2019-01-01

Characterization And Quality Assessment Of Smart Polymer Systems Fabricated By Using 3d Printing Technique

Carlos Alejandro Garcia Rosales
University of Texas at El Paso, cagarciarosales@miners.utep.edu

CHARACTERIZATION AND QUALITY ASSESSMENT OF SMART POLYMER SYSTEMS FABRICATED BY USING 3D PRINTING TECHNIQUE

CARLOS ALEJANDRO GARCIA ROSALES

Doctoral Program in Electrical and Computer Engineering

APPROVED:

Tzu-Liang Tseng, Ph.D., Chair

Yirong Lin, Ph.D., Co-Chair

Paras Mandal, Ph.D.

Deidra Hodges, Ph.D.

Charles Ambler, Ph.D.
Dean of the Graduate School

Dedication

I dedicate the doctoral research to my lovely wife, Julia, who has been on my side during my Ph.D. studies supporting and motivating me unconditionally. Thank you so much.

CHARACTERIZATION AND QUALITY ASSESSEMENT OF SMART POLYMER SYSTEMS FABRICATED BY USING 3D PRINTING TECHNIQUE

by

CARLOS ALEJANDRO GARCIA ROSALES, MSc

DISSERTATION

Presented to the Faculty of the Graduate School of

The University of Texas at El Paso

in Partial Fulfillment

of the Requirements

for the Degree of

DOCTOR OF PHILOSOPHY

Electrical and Computer Engineering Department

THE UNIVERSITY OF TEXAS AT EL PASO

May 2019

Acknowledgements

This work was supported by the National Science Foundation (DUE-TUES-1246050) and (NSF-PREM DMR-1205302). I wish to express sincere gratitude for their financial support. I would also like to would like to acknowledge the scholarship support by CONACYT. In addition, thank Akzo Nobel (USA) for provide us the material Ketjenblack, EC-600JD Electro-conductive carbon black. We thank Lubrizol (Ohio, USA) for provide us the material Tecoflex EG-72D.

Abstract

Shape memory polymers (SMPs) are classified as smart materials due to their inherent stimulus-induced response. SMP is capable of recovering its original shape from a high degree of deformation by applying an external stimulus such as thermal energy. Other stimuli are electricity, light, chemical, and magnetic field. Shape memory polymers (SMPs) and its fabrication process has recently attracted much attention as a result of their potential application as soft active materials. Demonstration of SMP systems fabricated via 3D printing technologies has been one of the most popular attempts. This dissertation presents an integration of two commercial SMP materials (DiAPLEX and Tecoflex) and a material extrusion (ME) printer to fabricate SMP parts and specimens. In addition, a simple approach to 3D printing of carbon black (CB) based shape memory polymer nanocomposites (SMP/CB) with toughness improving capabilities during programing stage using electrical stimulus is reported. Conductive SMP/CB nanocomposites, consisting of commercial SMP filled with conductive CB nanoparticles, were fabricated using solvent casting and single screw extrusion processes. In similar research, the fabrication of shape memory polymer/ graphene oxide composites (SMP/GO) using digital light processing (DLP) 3D printing was performed and is presented. In order to achieve SMP/GO systems, it was required to evaluate the proper SMP material mixing (monomer, cross-linker, photo-initiator). It has been demonstrated that GO has high photo-thermal properties, which eventually could be used for shape memory triggering using a laser beam with specific wavelength. In addition, since dimensional accuracy has been an inherent challenge in 3D printing, an artificial neural network (ANN) was developed on Phyton, which models the dimensional error of parts produced by DLP process. The ANN, which is trained by using historical DLP process data, could be used to predict the dimensional error based on input parameters. Finally, an approach that focuses on performing dimensional evaluation of printed SMP parts using a 3D scanner is proposed. For instance, two algorithms for dimensional evaluation of 3D printed parts and recovered parts are presented. A dimensional accuracy error

distribution was obtained by comparing the 3D scan file of the actual part with the CAD model. Another dimensional error distribution was acquired through evaluation of a SMP part through digital comparison of 3D scan files of a produced part and the recovered part.

The ME fabrication settings for the SMP specimens were defined by implementing a design of experiments (DOE) with temperature, velocity, and layer height as process variables. ME raster orientation factor was also evaluated separately. After fabrication, specimens were submitted to a thermo-mechanical cycle that encompasses tensile test, compact tension test, and a thermo-recovery process. On SMP/CB, material extrusion (ME) technique was used to 3D print dog bones type IV specimens for tensile test and electrical stimulus. On SMP/GO, it was required experimental trials to prove the compatibility of GO dispersed in the SMP photo-resin to be used in DLP process.

On pure SMPs fabrication, the material properties such as Young's modulus of the specimens was examined as a process output. Furthermore, stress-strain curve, strain recovery, instant shape-fixity ratio, long-term shape-fixity ratio, and recovery ratio of SMP specimens during a thermo-mechanical cycle were evaluated. Moreover, toughness property, maximum load, and load-displacement curves were investigated by using standard specimens to compact tension testing. Comparison studies of load-displacement, toughness and recovery efficiency of the specimens were carried out to determine the optimized fabrication parameters. On SMP/CB, temperature profiles at various electrical current levels, Young's modulus, and toughness results of the 3D printed specimens subjected and not subjected to electrical current were reported. On SMP/GO, mechanical properties of SMP parts, such as tensile-strength, and programing capacity of specimens using 3-point bending testing were characterized and reported.

It was found, according to main effect and iteration plots that fabrication parameters have an impact on SMP Young's modulus and exist minimum iteration among variables. In addition, Young's modulus variation of DiAPLEX and Tecoflex specimens was mostly caused by velocity and layer height parameters respectively. Moreover, results showed that SMP specimens were able to recover high levels of deformation. On SMP/CB composites, it was found that SMP/CB

electrical conductivity can be tuned by the CB filler fraction, and that an electrical current passing through SMP/CB nanocomposites causes temperature increments and changes on material strength condition. Moreover, it was observed that conductive SMP/CB specimens responded to electrical current stimulus by increasing their toughness four times higher than with no current applied during tensile test. On SMP/ GO composites, during experimental trials, it was found that specimens support high degree of deformation and full shape recovery, and that factors such as layer thickness and exposure significantly vary dimensional characteristics on final parts. On ANN dimensional prediction, it was found that inner layer architecture with 2(number of inputs) + 1 neurons achieved the maximum Pearson correlation prediction with 77.7 %. Finally, respecting the dimensional accuracy quality evaluation, a case study is presented through comparison of a commercial SMP substance and a traditional acrylonitrile butadiene styrene (ABS) material. Computational results obtained conclude that SMP and ABS parts have a similar level of dimensional accuracy while the SMP parts have an overall high degree of recovery.

This study contributes to process control as well as for rheological, toughness, and recovery properties of SMP parts produced by ME fabrication process. In addition, it is a reference for conductive properties of SMP/CB nanocomposites fabricated by 3D printing process, and programing properties of photo-responsive SMP systems fabricated via DLP 3D printing technique. Finally, this research paves a way to investigate quality assessment in dimensional accuracy for 3D printed parts.

Table of Contents

List of Tables

List of Figures

Chapter 1: Introduction

1.1 Background and Motivation

Material extrusion (ME) is a 3D printing technique that was initially considered a rapid prototyping alternative and has been demonstrated to be an innovative manufacturing technique for industrial, medical, automotive and aerospace sectors [1]. The fabrication capacity of ME technique makes possible to produce parts from 3D complex designs by depositing fused semi-liquid polymer material layer by layer in an additive manner until the completion of the part [2]. For a better insight in ME, Kuo et al., 2016 presents an overview of ME process, beginning with the extrusion of filament from pellets and continuing to fabrication of parts. Nowadays, commercial ME printers are designed to work with a limited number of polymer filaments. Acrylonitrile butadiene styrene (ABS) has been the most representative material in ME printers due to the easiness of print, smooth surface finish, and higher dimensional tolerance agreement over other materials. A strategy to promote the utilization of ME in design and manufacturing stages is to increase the list of material filament options. Higher material diversity implies adaptation of new polymer based composites filaments with commercial or customized 3D printers [3-12]. Another 3D printing technique with a high finishing resolution and fast curing speed is stereolithograpy (SL). This process is divide in two main classes of processes: scanning type (SLA) process, and projection type process. The former uses a UV laser beam to cure sections of photo-resin in a layer-by-layer fashion up to the completion of the part. The projection type uses a digital light projector (DLP) to cure resin by projecting the cross section of sliced layers of the CAD file up to the completion of the part [13-15].

Recently the 3D printing concept has evolved into 4D printing by incorporating smart materials in 3D printing technologies [16]. Smart materials are those that can be controlled by an external stimulus to generate a response. These stimuli can be a wide range of physical or chemical triggers such as but not limited to: induction heat, infrared radiation, chemical induction, light, electricity, external forces, and magnetic fields. These stimuli generate

responses such as: electricity, actuation force, molecular arrangement reconfiguration, thermal changes, or shape changes. Smart materials can be classified based on their stimuli to trigger response as: thermoresponsive, magnetoresponsive, chemoresponsive, photoresponsive, or mechanoresponsive [4-12, 17-19]. A type of smart materials that has attracted much attention is shape memory polymer (SMP). SMPs are block copolymers, formed of two types of segments: hard and soft segment. Cross-links among monomers in the hard segment provide the elasticity and mechanical strength required for the material to flow and be reshaped when the material is heated above the transition temperature (Tg). When deformation ends, and the part has cooled down to $T < Tg$, the soft segment establishes the new chain configuration by vitrification. The part is now in its new shape. This new shape will be kept indefinitely as long as $T < Tg$. Once $T > Tg$, the soft segment losses its strength and no longer support the new segment chain configuration. Then, entropic force acts as a driving force by releasing the stored strain energy and triggering the recovery [20, 21]. Therefore, SMPs are capable to memorize a primary shape, be subjected to a strain change, maintain a secondary shape, and be recovered to the primary shape after external stimuli is applied. There are a wide range of trigger stimuli to activate the SMPs such as thermal energy, light, electrical current/voltage, among others. Once the right stimulus is applied, the part initiates a shape transformation that persists over a period of time. This transformation response behaves differently according to the SMPs material properties, the level of stimulus and the fabrication technique.

SMP functionality has two stages: 1) fixing or programing and 2) recovery. The former process fixes the SMP parts into a secondary shape while the second consist in applying a stimulus to recover the part to its original shape. Therefore, the main functionality of SMP parts is the ability of restoring back to their original shape (primary shape) after they have been fixed in a temporary shape due to mechanical stress. This ability is known as shape memory effect (SME) [17, 20, 21]. Some SMPs functionalities and properties have been reported in the literature. In that matter, testing results include shape-fixity ratio, long-term shape fixity ratio,

recovery ratio, irrecoverable strain, tensile stress curves, Young's modulus, and storage and loss moduli [20, 22-25].

SMPs functionalities have been demonstrated mostly in applications that involve different levels of actuation and shape recovery [18]. Another application field is self-repaired systems, where successful damage restoration requires to be assisted by closing the surfaces with an external force assistance. In that regard, by activating the shape recovery properties, it is possible to avoid applying external forces to achieve autonomous fracture closure [26]. For instance, in SMPs a macroscopic crack can be closed by using the SME resulting in a microscopic crack that can be completely repaired by a self-healing mechanism [27].

Beside thermal-responsive SMPs, Electro-responsive SMPs are able to be programmed and recovered by the resistive heat generated in the parts by passing an electrical current through the parts. In such a case, the heat propagates in an internal-external fashion. An electrical stimulus, current, could be easy to control, sustain, and obtain a better heat distribution in the conductive SMP. In addition, photo-thermal SMPs are triggered by the photo-thermal effect of the material upon light exposure with a specific wavelength and through the surface plasmon resonance effect [28-30] that converts the light into thermal energy necessary to active the SME.

3D printing is a suitable alternative to replace conventional subtractive manufacturing methods, resulting in a minimum amount of wasted material, and to develop new design applications incorporating smart materials such as SMPs. Definitely, the aforementioned SMP material's functionalities in combination with 3D printing could lead into a new field of complex-functional parts. To achieve this, it is required to implement process control techniques, material characterization, and perform dimensional accuracy studies of 3D printed parts.

1.2 Problem Statements and Rationale

Clearly, the capabilities described above make SMP materials good candidates to be used in fabrication of programmable and recoverable devices. Although the successful efforts on

demonstrate SMPs functionalities, more mechanical characterization results are required that serve as guidelines during design stage to facilitate SMP application-oriented devices that achieve functional requirements, specifically during the programing stage. Moreover, functional devices made of SMPs are required to to be embedded in host structures at specific location or to hold complex shapes. These complex shapes are difficult to attain using conventional assembly methods and fabrication techniques since they are difficult to incorporate, or expensive to produce [16, 18]. A fabrication alternative that can fulfill those requirements is 3D printing. Therefore, process control studies are required in SMP-3D printing integration attempts especially with new functional materials in order to obtain acceptable quality of parts. Therefore, challenges to overcome are the control of 3D printing processes during SMP part fabrication, characterization of mechanical properties of SMP 3D printed parts, development of new functional material composites with a variety of SME triggering stimuli, and quality evaluation (specifically dimensional accuracy). An example of SMP part characterization could be quantify the mechanical properties, or evaluate functional restoration (toughness efficiency) on macroscopic damages. Combining SME and self-healing in a single material that is able to recover its original shape and be self-repaired in situ is a challenge that could minimize resources during service and maintenance operations in systems [16, 31]. Although findings on restoration of micro-cracks or scratches has been recently published, it is required more studies on functional restoration tests on macroscopic damages potentially found in material applications.

Thermal radiation is the most popular SME triggering mechanism that needs to continue being studied. Furthermore, programing and recovery activation of limited access regions in thermo-responsive systems is not easy to be tailored by the thermal radiation triggering mechanism. Thermal radiation could be easily dissipated in the surrounding environment, and an optimal heat distribution on the part is not guaranteed. Temperature distribution can vary on the sample and eventually the programming capacity and the recovery effect will be diminished. In addition, it is hard to tailor specific regions without to influence the surrounding environment increasing the risk of affecting adjacent system components. An alternative for the above-

mentioned drawbacks is electro-responsive and photo-responsive SMPs. Fabrication of electro-responsive and photo-responsive requires the doping of a SMP polymeric matrix with functional nanoparticles. In this regard premature breaking is a drawback in SMP nanocomposites compared to pure SMP since nanoparticle addition increases material brittleness. Otherwise this drawback could be overcome by increasing the temperature on the sample to modify its strength properties by passing a controlled current trough the part. Another challenge, is nanoparticle even distribution which can be solved by selecting the adequate material mixing and the proper fabrication method.

Another challenge on 3D printing of SMPs is the part dimensional accuracy evaluation that include all the critical features which can lead in complex optimization problem. An inspection of the overall features at a time creates a single optimization problem that can lead to a breakthrough in the 3D part dimension inspection. To accomplish that, better measurement devices are required. This is possible to be accomplished with a high resolution 3D scanner, by comparing a 3D scan file of an actial produced part with the CAD model. Furthermore, it is required to explore new modelling techniques that strong correlates the process parameters with the dimensional aspect of the SMP parts that allow to predict and optimize process outputs.

1.3 Objectives of the Study

The main goal of the study is fabrication and characterization of smart polymer systems fabricated by using 3D printing fabrication methods. In addition, an evaluation of dimensional accuracy of the fabricated parts, and modelling of the dimensional error. In order to achieve this, the specific objectives are:

Objective 1: To demonstrate the capability of ME technology in producing parts using commercial SMPs and to find the optimal 3D printer process parameters. Furthermore, this objective expands to evaluate the contribution of fabrication variables in tensile-strength properties, and to quantify the fixity and recovery levels of the samples.

Objective 2: To investigate the toughness property of SMP parts during fracture damage and to quantify the recovery efficiency upon macroscopic damage restoration on the parts. Moreover, to obtain an insight of the influence of ME parameters on maximum load, load-displacement curves, toughness, and recovery efficiency of the SMP parts.

Objective 3: To 3D print conductive SMP/CB nanocomposites using ME technique. Moreover, the objective expands to characterize the stress-strain response of the material under tensile loads and quantify the toughness of specimen subjected to an electrical current during the programming stage, which is critical to avoid premature breaking. Finally, this research intends to demonstrate super elastic behavior of SMP/CB nanocomposites during programming stage.

Objective 4: To 3D print photo-responsive SMP/CB nanocomposites using DLP streolithography (SL). This implies, to customize photo-curable resin material ratios and the fabrication of photo-thermal polymer composites from resin/ graphene-oxide (GO) mixture. GO wt% is a critical value that needs to be determined in order to achieve suitable fabrication.

Objective 5: To evaluate the printed accuracy of ME parts as well as the recovery of SMP parts by inspecting them with a high resolution 3D scanner technology. With the proposed algorithms, all the dimensions and regions of the parts are inspected and evaluated. It is possible to obtain a dimensional error distribution graphs with a color map indicating the regions inside and outside of the dimensional specifications.

Objective 6: To evaluate artificial neural network (ANN) methodology performance as a modelling tool on stereolithography (3D printing technique) for dimensional accuracy prediction of SMP parts. By using ANN, it is possible to predict dimensional accuracy error on SMP parts and obtain an insight of the dimensional error on final parts by evaluating the process parameter without fabrication of the parts.

1.4 Scope and Limitation

The scope of this dissertation lies on evaluate the fabrication and functional characteristics of thermal-responsive, electro-responsive, and photo-responsive polymer

composites on ME and DLP 3D printing manufacturing process. Moreover, the scope encompasses fabrication and demonstration of polymer nanocomposite filament through solvent casting method and single-screw extrusion process. Further, design of experiments (DOE) and artificial neural network (ANN) are the selected methodologies for investigation of the process fabrication settings. Then, stress-strain, compact test, and three point bending tests are the evaluation methods for property characterization on fabricated specimens. Stress-strain and compact tests lead to calculation of Young's modulus and toughness properties, and three point bending test lead to bending capability factor during specimen programing. Finally, this dissertation encompasses evaluation and modelling of dimensional accuracy on SMP parts.

Material cost and material availability have been a limitation on the present work. Therefore, the efforts have been focused on fabricate the samples for testing required on ASTM standard.

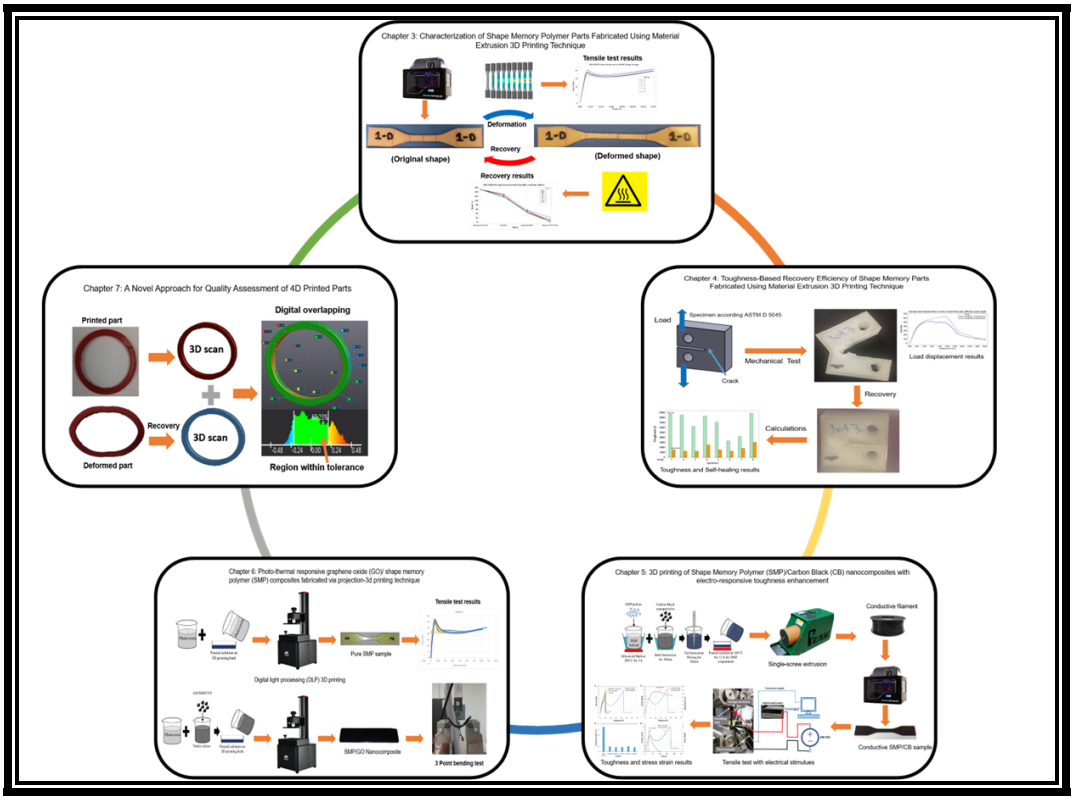

Fig. 1.1: Outline of the dissertation.

1.5 Outline of the Study

Figure 1.1 represents an outline of the dissertation. The figure shows an overview of the following research chapters and their contents in terms of material, fabrication process, testing, and expected results. In addition, the outline provides a quick reference for topics of interest. The outline includes chapter 3 and 4 where characterization of pure SMP specimens is performed, continuing with chapter 5 and 6 where SMP composites are developed and characterized. Finally, chapter 7 digs into the quality control of dimensional accuracy (dimensional error) of specimens using cutting edge technology, and dimensional error prediction using Artificial Neural Network (ANN) on SL process.

Chapter 2: Literature Review

Many SMPs and their properties have been reported in the literature. Specifically, these works focus on thermo-rheological characterization that include programming and recovery testing by submitting the specimens to a thermo-mechanical cycle. Testing results include shape-fixity ratio, long-term shape fixity ratio, recovery ratio, irrecoverable strain, tensile stress curves, Young's modulus, storage and loss moduli [20, 22-25]. Recently, fabrication of SMP parts using 3D printing has been attempted successfully, demonstrating SMP's functionalities and feasible material-machine integration [4-12, 19, 32-36]. This SMP-3D printing integration is defined as 4D printing [16, 18]. Li et al. [35] and Yang et al. [32] reported the functionality of SMPs by fabricating a gripper, it was programmed (in a secondary shape) and recovered, enabling the gripping action through SME. Another example is Zarek et al. [33] who proved the functionalities of SMP parts using a temperature sensor electronic device. The thermos-responsive SMP device returns to its original shape at high temperatures, turning a LED on by completing a circuit. Yu et al. [34] fabricated an inter-locking device to prove the functionality of SMPs. Specifically, ME 3D printing technology [2] has demonstrated a good compatibility with SMPs [32]. According with previous studies, an SMP-ME integration simplifies the exploration of a new field of complex-functional devices due to the ability of ME of producing complex shape parts without the need of sophisticated metal molds. A related field of study concluded that ME variables have an influence on the part properties since the process control implies multi-variable adjustments [37-44]. Based on previous literature, the most influential variables in quality of printed part are: nozzle temperature [32, 37], which pertains to the temperature reached by the filament inside the nozzle and during deposition; velocity [32] which pertains to the displacement of the nozzle (printing head) during the deposition; and layer height [40], which pertains to the displacement of the printing head along the Z axis after the completion of one layer and the initiation of the next.

Much of the recent work is oriented to investigate shape memory assistance in self-healing capabilities [26, 31, 45-49]. These studies highlight the benefits of combining SME and self-healing in a single material that is able to recover its original shape and be self-repaired in situ, minimizing resources during service and maintenance operations [16, 31]. Otherwise, these works based their results on micro-cracks or scratches restoration and omitted functional restoration tests on macroscopic damages potentially found in material applications. Moreover, the authors pointed out the contribution of SMPs in assist self-healing capabilities and report functional restoration results of the investigated material but they omitted restoration results on SME and self-healing properties independently.

Not only pure SMPs are investigated, polymer nanocomposites has been presented in many research studies where it is presented doping of polymeric matrix to enhance the composite properties and meet specific functionalities [50]. The present research, specifically chapters 5 and 6 focus on 3D print polymer nanocomposites with conductive [47, 51-66] and photo-thermal properties [28-30, 45, 67-71] respectively. Findings on these works will expand shape memory functionalities in SMP nanocomposite systems as electro-responsive and photo thermal responsive systems. In this regard, electro-responsive SMPs are able to be programmed and recovered by the resistive heat generated in the parts by passing an electrical current through the parts. In such a case, the heat propagates in an internal-external fashion. An electrical stimulus, current, could be easy to control, sustain, and obtain a better heat distribution in the conductive SMP unless conductive nanoparticles are distributed non-uniformly in SMP matrix. Conductivity is enhanced on polymers by adding conductive nanoparticles to it [5, 47, 52, 53, 72]. Attempts to develop conductive 3D printed conductive SMPs has been limited to fabricate and test conductive SMP nanocomposites on film fashion samples with techniques such as press molding or casting.

SMP functionalities on photo-thermal SMPs are triggered by photo-thermal effect of the material upon light exposure with a specific wavelength and through the surface plasmon resonance effect [28-30] that converts the light into thermal energy necessary to active the SME.

The most common alternative for light triggering is a laser beam stimulus that easily could be focus on very specific regions of the SMP composite polymer system without interaction with other regions. In addition, the laser beam does not required a medium to be transfer and hit the desired regions (remote control, wireless actuation) [69]. Moreover, the laser power output is feasible to be controlled by tuning the laser controls [68]. Photo-thermal property could be enhance in SMPs by doping the polymeric matrix with photo-thermal nanoparticles. Fabrication of photo-thermal polymer has been demonstrated on several studies [45, 67-71, 73]. Liang et al. [68] presented a full characterization of sulfonated graphene / thermoplastic polyurethane (TPU) composites. Samples were fabricate by solvent-casting method and the optical properties were submitted to characterization tests including absorbance and transmittance under infrared (IR) light. Moreover, tensile and recovery properties on samples were evaluated under IR. It was found that the level of carbon content and the distribution variation on the polymeric matrix lead to IR absorbance variation. Recovery test showed that graphene/TPU samples recovered after been exposed to IR during 10 s. In similar work, Yang et al. [67] demonstrated the fabrication of photo-responsive 3D printed objects by combining the benefits of ME and photo-responsive carbon black (CB)/SMP composites. Illumination triggers the SME on the samples by photo-thermal conversion. Different CB wt % content was added to the SMP matrix. It was found that variation on CB doping fraction and light intensity irradiated on the sample leads to different temperatures on the samples. Recovery results showed that bended samples are able to be fully recovered after 180 s of illumination. Kohlmeyer et al. [69] presented the remote control of multi-shape memory functionality on carbo nano-tubes CNT/Nafion composites. Samples (strips) were programed and then recovered by tailoring near IR light on specific sample sections, allowing intermediate shapes between temporary shape and full recovered shape. Leng et al. [70] presented the testing and SME evaluation of styrene-based SMP/CB composites. In addition to the characterization testing (scanning electron microscopy SEM, differential scanning calorimetry DSC, dynamic mechanical analysis DMA), it is presented recovery results on bended samples that responded to IR exposure. Recovery results on SMP/CB samples reach 100 % after

approximately 200 s. Yu and Yu [71] presented graphene oxide (GO)/SMP composite with photomechanical properties fabricated with casting method. The GO acts as light absorbent and photo-thermal nanoscale converter that initiates the SME. SME effect was demonstrated with mechanic oscillation response on the sample upon irradiation of visible light. Yoonesii et al. [73] exhibited the enhanced recovery properties of graphene polyimide nanocomposites in comparison of neat polyamide. In addition to this, mechanical dynamic storage moduli increased linearly with graphene content additions. Zhang and Zhao (2013) developed a poly-ethylene based SMP/gold nanoparticles (AuNPs) composite. The SMP/AuNPs exhibited both shape memory and self-healing properties triggered by light. Heating effect from the surface plasmon resonance on the AuNPs induced the SME, and by controlling the light power output was possible to control the self-healing on a damage though crystal melting and crystallization. Although the successful fabrication attempts for photo-thermal polymer, it would be beneficial to demonstrate photo-thermal effect on SMPs fabricated by using novel 3D printing techniques [45, 67, 73].

Although SMPs on 3D printing has been demonstrated at most on ME 3D printing process, SL is a technology with several advantages that need to be explored for SMPs. Recent research work [13-15] developed and used liquid based SMP photo-resin on a successful fabrication of SMP parts using DLP and SLA fabrication processes. Fabricated parts presented high resolution surface finishing and higher quality over ME. Moreover, it was not necessary to add any support material, the geometry complexity was increased, and the building time was reduced. Although the reporting advantages and functional capability demonstration, the authors pointed out a dimensional accuracy drawback on the final SL parts due to material shrinkage caused by photo-resin properties and fabrication settings. Not only SMPs produced by SL has led in dimensional accuracy errors, in general, it has been a challenge to overcome in 3D printing.

On ME, it has been proposed several methodologies aimed to improve (optimize) the dimensional accuracy in 3D printing parts [38, 40-44, 74]. The dimensional measurements performed in these studies were done using conventional devices (i.e., standard micrometer,

coordinate measuring machine, vision camera). The features considered were mostly basic such as circular or rectangular prism. These basic features were primarily selected for simplicity of taking measurements or because these instruments are limited to measure distances between parallel faces and not allow measurements from the entire features of the part. Studies were typically performed in X, Y, and Z axis (i.e., length, width, and thickness), generating a complex multi-objective optimization problem [39] with three responses, one per dimensional direction (i.e., reducing variation in length, width, or thickness). Although the previous effort on ME, the challenge remains of considering all dimensional features and regions of the part. Next, it is presented several efforts on optimal design of the fabrication parameters for SL printing process planning and efficiency by modelling the process and responses. The main objective of these works is to reduce the build time, improve the quality of the parts, and reduce cost. Specifically, the improvement of dimensional accuracy is a common objective on SL.

Parameter optimization on SL process has been attempted on several research works [75-83]. These works present different approaches to optimize different part characteristics based on the process input parameters. Schaub et al. [75] described the benefits of implement optimization techniques on SL process. A SL process could involve up to 50 variables and an optimization technique could find the optimal parameters based on the customer requirements, reducing process variability and material scrap (cost). Lan et al. [76] presented an empirical optimization formulation to maximize the non-stepped surfaces of a design and to find the optimal fabrication orientation that allow to improve the surface quality and reduce the build time. On similar study direction, Pang et al. [77] analyzed the distortion and dimensional accuracy error on SL systems by fabricating “letter H” specimens. This study concluded that dimensional error and distortion is caused by three aspects during SL process: distortion during SL, caused by material shrinkage; distortion during sample removal from platform; and material shrinking during post-cure with UV light. Different optimization methodologies have been also explored. Onuh and Hon [78] explored the use of Taguchi fractional factorial design to optimize surface roughness based on layer thickness (thickness of layer), hatch spacing (solidifying process of the cross section of a

layer), hatch spacing (distance between parallel cure sections on a layer), hatch overcure (cure depth), hatch fill cure depth (cure excess over cured layer). Optimal results leaded to build parts faster, cheaper, and with better dimensional accuracy. In addition, Lynn-Charney and Rosen [79] focused on develop a mathematical model by using response surface methodology (RSM) for SL process, improving finishing characteristics, and reducing building time. The input variables considered were Z-level, hatch overcure, fill overcure, and sweep period. Moreover, the resulting response surface equation allows to calculate six types of geometric tolerances such as positional, flatness, parallelism, perpendicularity, concentricity, and circularity. Karalekas and Aggelopoulos [80] presented a combination of theoretical analysis (lamination theory) and experimental runs to develop a model that correlate the process and material variables with the chemical shrinkage strains on SL parts. This experimental and analytical method could be implemented on other studies for polymerization shrinkage analysis. Zhou et al. [81] presented a combination of two analysis tools, response surface methodology and analysis of variance (ANOVA), for SL parameter evaluation and product optimization of dimensional accuracy. In this work is delivered an equation that includes major control factors (layer thickness, Z level wait, sweep period, over cure, blade gap, hatch spacing, dip velocity and dip acceleration). Response surface model was developed and the ANOVA was used for confidence interval and adequacy of the model. X, Y, and Z dimension were predicted with an accuracy of about 90%. Cho et al. [82] focused on increasing build accuracy by designing the appropiate process parameters. A genetic algorithm (GA) was selected to be implemented, based on the nonlinearity and dinamic cathactheristics of the SL process to obtain an accurate model. The near-optimal SLA condition was evaluated by experimental investigation. Finally, reeves and Cobb [83], presented a numerical modelling technique for defining optimum build part orientation on SLA process. A predicted model of roughnees deviation was constructed by varing the fabrication angle, layer thickness, and layer profile.

Chapter 3: Characterization of Shape Memory Polymer Parts Fabricated Using Material Extrusion 3D Printing Technique

3.1 Introduction

Shape memory polymer (SMP) is capable of recovering its original shape from a high degree of deformation by applying an external stimulus such as thermal energy. This chapter presents an integration of two commercial SMP materials (DiAPLEX and Tecoflex) and a material extrusion (ME) printer to fabricate SMP specimens. The material properties such as Young's modulus of the specimens was examined as a process output. Furthermore, stress-strain curve, strain recovery, instant shape-fixity ratio, long-term shape-fixity ratio, and recovery ratio of SMP specimens during a thermo-mechanical cycle were investigated. The ME fabrication settings for the SMP specimens were defined by implementing a design of experiments (DOE) with temperature, velocity, and layer height as process variables. It was found, according to main effect and iteration plots that fabrication parameters have an impact on Young's modulus and exist minimum iteration among variables. In addition, Young's modulus variation of DiAPLEX and Tecoflex specimens was mostly caused by velocity and layer height parameters respectively. Moreover, results showed that SMP specimens were able to recover high levels of deformation. Results on this chapter are a reference for process control as well as for rheological properties of SMP parts produced by ME fabrication process. The sub-section called "materials and fabrication" describes how a design of experiment (DOE) generates the trial settings to fabricate the specimens for a tensile-strength test. The sub-section called "mechanical properties" describes the tensile test. The sub-section called "programing–recovery characterization of SMP parts" presents the algorithm of the programming and recovering stages and the terms involved. Lastly the sections of results and conclusions are presented.

3.2 Material and Fabrication

The thermos-responsive SMP's, DiAPLEX MM-4520 and Tecoflex EG-72D, used in this study are cross-linked glassy copolymers with a Tg of 45 ℃ and 74 ℃, and a melting temperature of 200 ℃ and 210 ℃, respectively [20, 67]. This commercial SMPs were selected

due to their glass transition and melting temperature being adequate for the process parameter range. DiAPLEX, acquired from SMP technologies (Tokio, Japan), was provided in form of pellets and extruded in printable filament by utilizing a Filabot extruder of single screw. The filament was extruded at 182.5 ℃ with an average cross section diameter of 1.61 mm. Tecoflex EG-72D, obtained from Lubrizol (Ohio, USA), was provided in a filament fashion with 1.75 mm diameter. A ME 3D printer (Makerbot, Replicator 2X) was selected due to its demonstrated success in printing SMP filament [67]. A design of experiment (DOE) was implemented for each material to study the influence of fabrication settings on specimen material property. Based on previous literature, the most influential variables in the quality of a printed part are: nozzle temperature [37, 67], which pertains to the temperature reached by the filament inside the nozzle and during deposition; velocity [67], which pertains to the displacement of the nozzle (printing head) during the deposition; and layer height [40], which pertains to the displacement of the printing head in the Z axis after the completion of one layer and the initiation of the next. Two levels were determined for each factor. In the case of DiAPLEX, the levels were stablished according to Yang (2016), while Tecoflex required prior trial and error fabrication attempts for level selection. Table 3.1 presents the factors and levels of study into consideration for both materials, DiAPLEX and Tecoflex. Table 3.2, and Table 3.3 show the runs derived from a DOE for both SMPs. For all samples infill was kept at 100 percent.

Table 3.1: Factors and levels of the DOE.

Material	DiAPLEX		Tecoflex	
Level	-	+	-	+
Temperature (ºC)	230	235	215	225
Velocity (mm/s)	80	100	65	75
Layer Height (mm)	0.25	0.3	0.27	0.3

Table 3.2: DOE runs for DiAPLEX.

Run	Temperature (ºC)	Velocity (mm/s)	Layer Height (mm)
1	235	100	0.3
2	235	80	0.3
3	230	80	0.3
4	230	80	0.25
5	235	80	0.25
6	230	100	0.3
7	230	100	0.25
8	235	100	0.25

The DOE's main purpose is to evaluate the properties of the parts fabricated against the settings of each run. Five replicas of a Dog Bone type IV according to ASTM standard D638 (Fig. 3.1a) were fabricated for each run [20, 84]. Specimens fabricated are classified in groups 1 to 8 corresponding to the DOE run settings utilized. To avoid potential bias during fabrication it was used a randomized DOE. Stress-strain curves were generated and an evaluation of Young's modulus response was performed. Also, for the recovery evaluation eight specimens of each DiAPLEX and Tecoflex specimens were fabricated. Actual samples of ME specimens are shown in Fig. 3.1b, c.

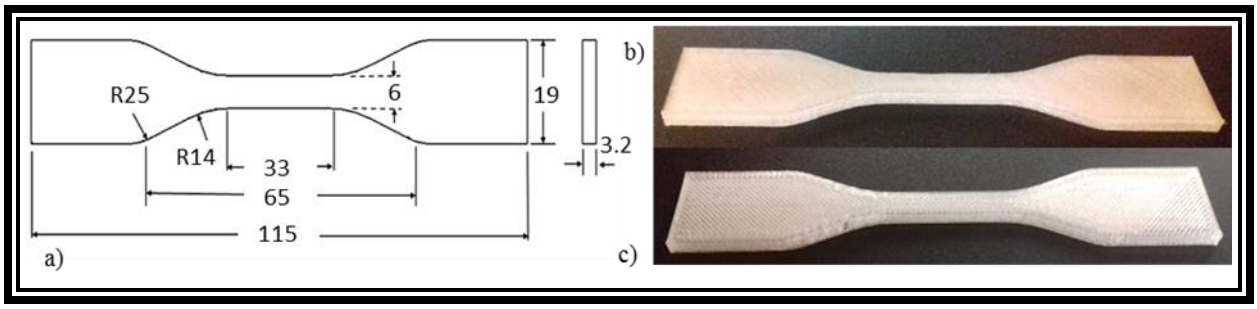

Fig. 3.1: Dog bone specimens. a) Schematics Type IV (mm). b) DiAPLEX specimen. c) Tecoflex specimen.

Table 3.3: DOE runs for Tecoflex.

Run	Temperature (ºC)	Velocity (mm/s)	Layer Height (mm)
1	225	65	0.3
2	225	75	0.27
3	215	65	0.27
4	215	75	0.27
5	225	65	0.23
6	215	65	0.3
7	215	75	0.3
8	225	75	0.3

3.2.1 Material Properties

The tensile property of the SMP materials was characterized using the dog bone type IV specimens. These tests were conducted using an INSTRON 5969 with an extension rate of 5 mm/min, a maximum extension of 50 mm, and a holding grip of 25 mm on each end of the 115 mm long dog bone. An extensometer was attached at the center of the sample in order to obtain an accurate reading of extension to calculate the modulus of elasticity. As soon as the sample was released from the clamps, the length of each sample was measured. Tensile strength measurements were carried out at room temperature which is below the Tg of the SMPs materials.

3.3 Proposed Methodology

The SME thermo-mechanical process consists of two main stages: the programming stage and the recovery stage (Fig. 3.2) [22].

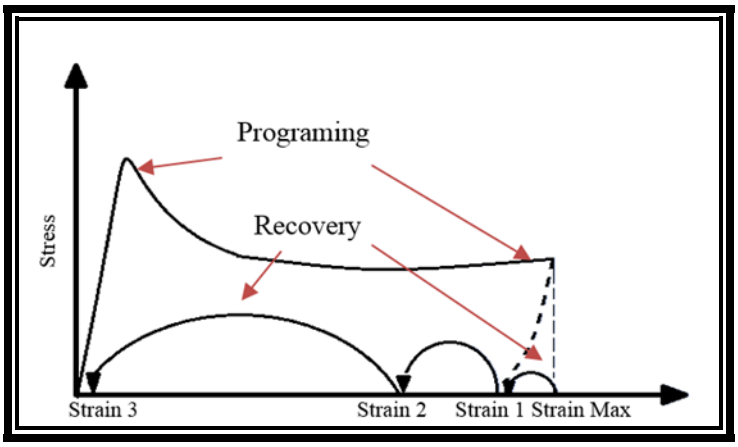

Fig. 3.2: Programing-recovery stages.

3.3.1 Programing–Recovery Characterization of SMP Parts

The programming stage focuses on modifying the original form of the part by causing a deformation into a new temporary shape by mechanical stress application. The new shape will be fixed until the start of the recovering stage. The recovering stage is characterized by strain level after unloading (strain 1), strain after creeping effect (strain 2), and strain after applying thermal stimulus (strain 3). In order to perform the programing-recovering characterization of the SMP parts, the algorithms described below show the steps to follow.

3.3.1.1 Programming Algorithm

i. Tension at a constant speed rate is applied on the specimen until the maximum specified strain % is reached. In the present study, this step was performed using the dog bone type IV specimens and the INSTRON 5969 machine with maximum strain % (Strain Max) values for specimen.

ii. Once the specimens reach their corresponding maximum strain (%) the specimen is unloaded, keeping a new temporary shape.

3.3.1.2 Recovery Algorithm

iii. Measure the residual strain (%) after unloading and calculate the instant shape-fixity ratio (Rfi). Rfi is calculated using the next equation (Fig. 3.1):

Rfi= Strain 1/ Strain Max……...(3.1)

iv. Evaluate the creeping effect. Measure the specimen periodically until no significant changes are observed. Calculate the long-term shape fixity ratio (Rf1) using the next equation (Fig. 3.2):

Rf1= Strain 2/ Strain Max……..(3.2)

v. Apply the recovering stimulus. In the present work, a thermal stimulus was used. The heating reference is the glass transition temperature (Tg) of the SMP material. Tecoflex specimens were subject to 75 ℃ for 2 minutes. DiAPLEX specimens were subject to 45 ℃ for 1 minute and to 50 ℃ for another 1 minute.

vi. Measure the residual strain (strain 3) and calculate shape recovery ratio (Rr) using the next equation (Fig. 3.3):

Rr = (Strain2 – Strain 3)/ Strain 2 (Fig. 3.3)……..…(3.3)

3.4 Results and Discussions

3.4.1 Process Factor Impact on Young's Modulus

Fig. 3.3 shows the main effects plot for DiAPLEX and Tecoflex with Young's modulus as a response. Young's modulus is classified as a response since it is a determinant value that affects ultimate tensile strength and elasticity capacity of the samples (Young's modulus was calculated based on the area derived from specimen's design specification). In Fig. 3.3a (DiAPLEX), it can be observed that the velocity has the largest impact on Young's modulus, followed by temperature, and lastly the layer height. Low velocity led to a higher Young's modulus since more material was deposited along the path, fabricating samples with better layer bonding. It is important to note that by changing the velocity value, the extrusion rate is automatically modified to compensate for the velocity. High temperature increased the Young's modulus, since it reduces the viscosity of the material and it flows more easily out of the nozzle depositing more material. In these regards, Fig. 3.5a shows that specimens fabricated with a lower level in velocity and an upper level in temperature (group 2) have a weight average of 5.26 g. In contrast, samples fabricated with an upper level in velocity and a lower level in temperature

(group 6) have a weight average of 4.90 g (Fig. 3.5a). Normal distribution of specimen weight is shifted to the left by using setting 6. In addition, the increase of the Young's modulus by increasing the layer height is consequence of better layer-to-layer bonding in the specimen due to more material being extruded. Thus, it results in less room for air gaps to occur with fewer layers. The total number of layers used were 16, 17, and 18 for layer heights of .3, .27, and .25, respectively. In this regard, Fig. 3.5b shows how the normal distribution of specimen weight is shifted to the right by using upper level of layer height. Fig. 3.3a presents consistency with Fig. 3.5b (Tecoflex) in the Young's modulus effect relative to temperature and layer height. However, an opposite effect is observed in velocity; when velocity increases, Young's modulus increases in the range from 159 to 163 MPa. It is important to point out that in the Tecoflex samples, velocity has the smallest effect on the Young's modulus with a 4 MPa in variation range compare to the 11 MPa effect caused by layer height within data that has a standard deviation of 5.66 MPa. Therefore this low variation is caused by the interaction between layer height at low level and velocity at low level specifically (Fig. 3.4b), deriving that the deposited material do not fill the gap among parallel paths and generates poor layer bonding. It is seen in Fig. 3.4 that both SMPs' DOE present minimum variable interaction, except for the interaction between temperature and layer height in Fig. 3.4b.

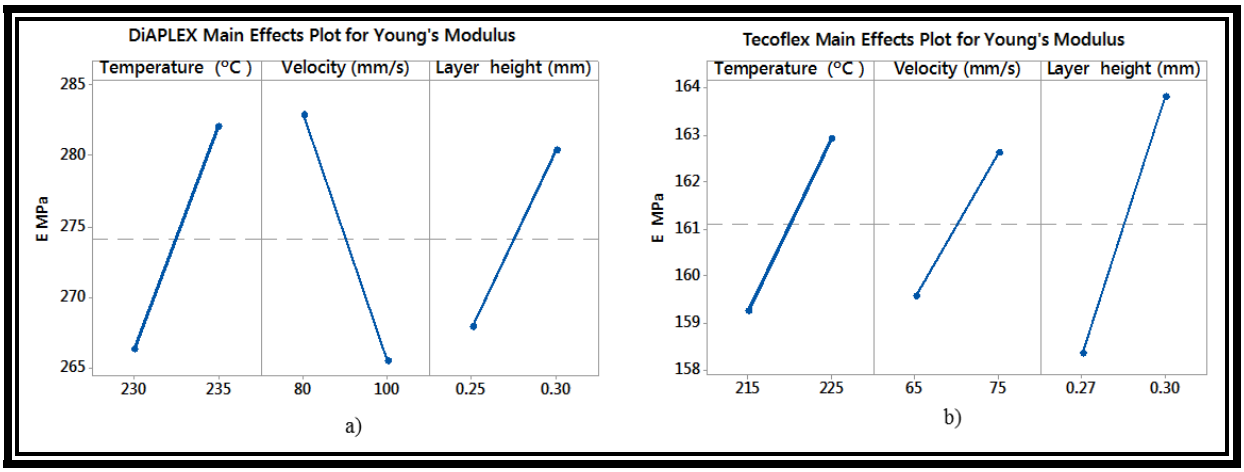

Fig. 3.3: DOE Main effect plot. a) DiPLEX. b) Tecoflex.

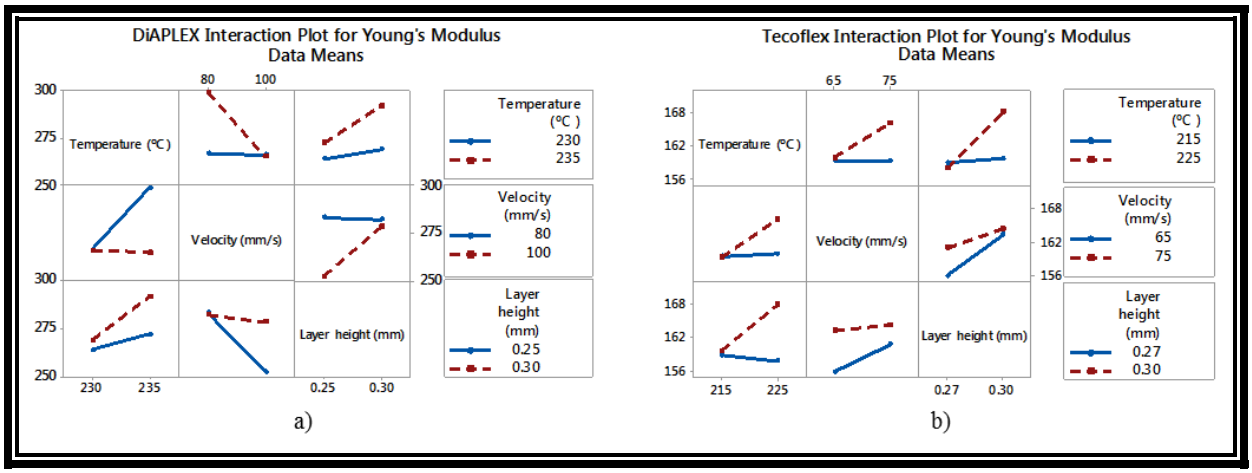

Fig. 3.4: Interaction plot. a) DiAPLEX. b) Tecoflex.

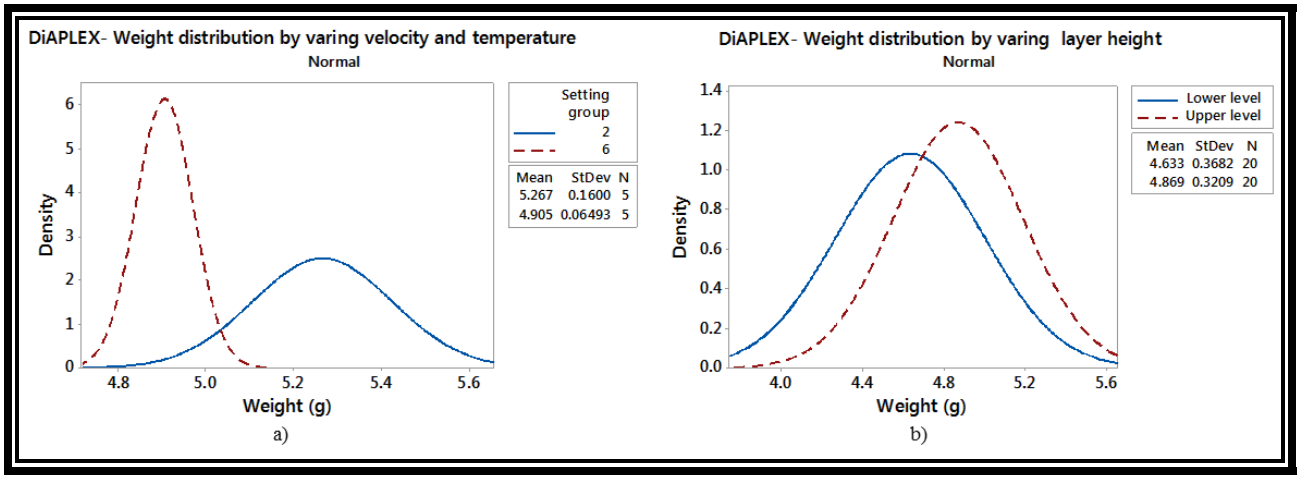

Fig. 3.5: Normal distribution. a) Comparing group 2 against 6. b) Comparing low against upper level of layer height.

3.4.2 Stress-Strain Curve Analysis

Fig. 3.6 present the stress-strain average curves for DOE specimen groups. For DiAPLEX (Fig. 3.6a), it is observed that fabrication settings caused a variation in the elastic region. A variation in the upper yield stress point is also noticed. During the plastic region it is observed a variation in the lower yield stress point. All the facture points happened during the plastic region at various strain % levels. The breaking point ranged from 10.35 % strain to 24.98% strain. Group 3 presented the higher elongation with a 24.98 % strain followed by group 4 and group 8. We attribute the variation of stress-strain curves to the different settings that lead

to various amount of deposited material, and layer interface bonding. Material amount and temperature conditions vary the polymeric arrangement occurring at the layer interface. All the specimens have being tested at room temperature conditions. For Tecoflex (Fig. 3.6b), it was observed that all groups were more consistent in different setting values compared to DiAPLEX. A variation is observed in the upper yield stress point. The elastic region looked consistent as well as the plastic region. No breaking points are observed leading to a maximum strain of 151.51 % for all groups. The maximum strain tested was 151.51% due to testing setup limitation. These curves reflect the super plasticity properties of TECOFLEX even at temperatures below the material's Tg.

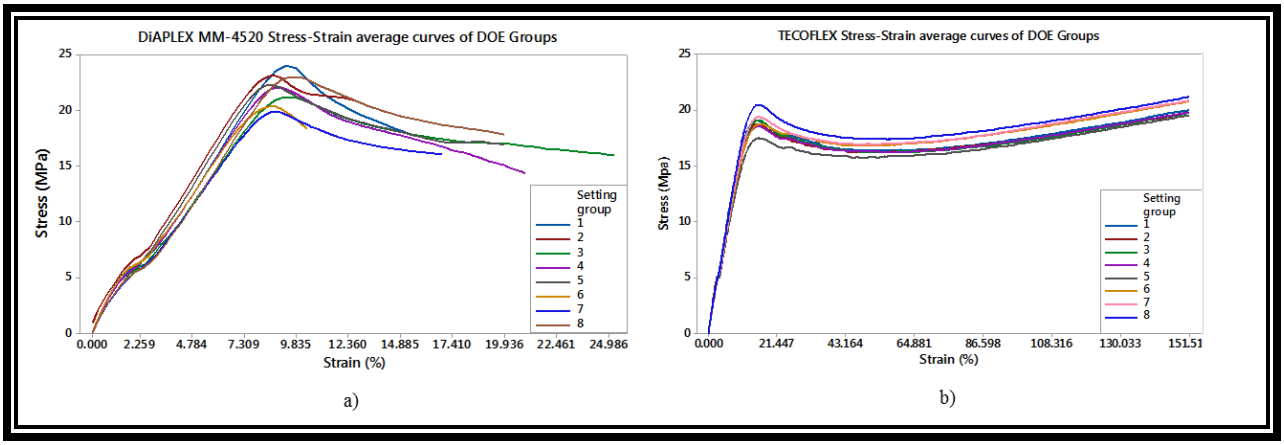

Fig. 3.6: Stress-Stain average curves of DOE specimen groups. a) DiAPLEX. b) Tecoflex.

3.4.3 Young's Modulus

It is seen clearly in Fig. 3.7a the impact of settings parameter in Young's modulus of ME parts made of DiAPLEX. Young's modulus varies from 250 to 310 MPa, around a 60 MPa between minimum and maximum value. The maximum point is the value of the specimen group fabricated with settings #2 (high level temperature, low level velocity, high level layer height) and the minimum point is the value of specimen group fabricated using settings #7 (low level temperature, high level velocity, low level layer height). This indicated that the fabrication setting causes the variation in Young's modulus of specimens. Fig. 3.7b shows that Tecoflex

specimen groups have Young's moduli range from 150 MPa to 170 MPa, 20 MPa from lower to upper value, around a third from DiAPLEX's variation range. Groups 1 and 8 have a Young's modulus fairly similar close to 168 MPa; group 3 and 7 are also similar with values around 161 MPa; group 4 and 6 are similar having 157 and 158 MPa, respectively. Moreover, Fig. 3.8 presents the boxplots of Young's modulus for both materials under investigation. The boxplot of settings group 8 and 2, that corresponds to DiAPLEX and Tecoflex respectively, have a central median value and a narrow shape distribution. Therefore, settings 8 and 2 lead to low Young's modulus variability. As a result, the optimal settings prove to be as follow: temperature 235 ºC, velocity 100 mm/s, and layer height .25 mm. For TECOFLEX, the optimal settings are as follow: temperature 225 ºC, velocity 75 mm/s, and layer height .27 mm.

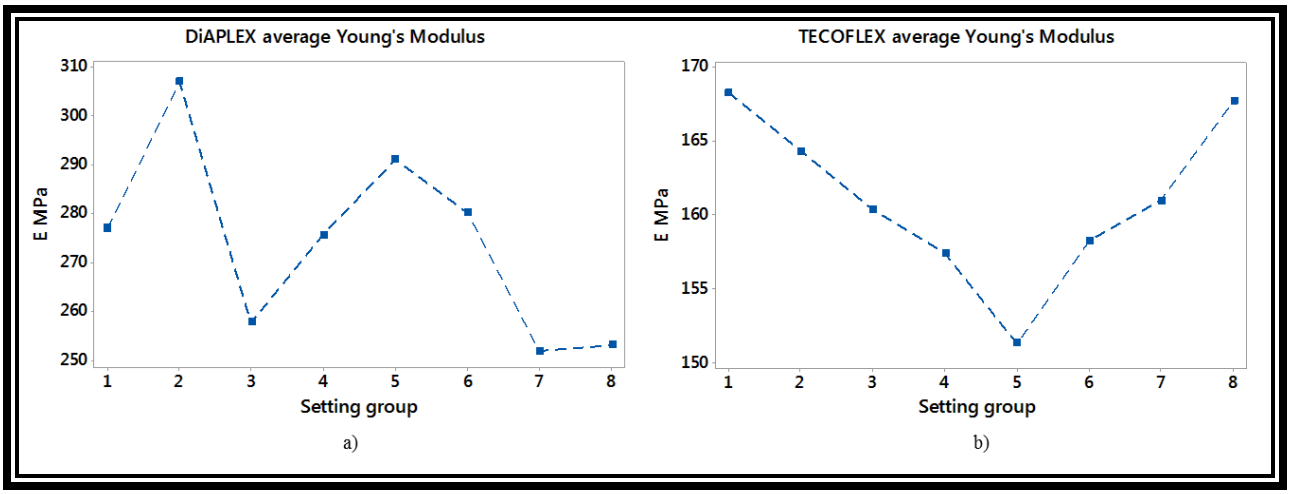

Fig. 3.7: Young's modulus by setting group. a) DiAPLEX. b) Tecoflex.

3.4.4 Strain Recovery Results

For the strain recovery assessment, in order to prevent sample fracture during the tensile test, was necessary to fabricate new DiAPLEX samples and stretch them to a different maximum strain % (Table 3.4). Samples were fabricated under similar conditions, once the parameters were stablished the fabrication process started. When each sample was finalized, the bed temperature was turned off leading the sample to cool down to ambient temperature to be removed. This is

because previous DOE results have shown that fractures occurred at different elongation as it is observed in Fig. 3.5a. We used settings from group 8, since it had the lowest Young's modulus variability, to fabricate eight samples. Fig. 3.9a presents the maximum strain level of each specimen during the recovery process. It was observed that after unloading the samples, strain decreased slightly. This was expected, since a high level of strain energy was stored in each sample. After the samples were left at room temperature for 144 hours to evaluate long term relaxation by creeping effect, residual stress decreased sharply in all the samples, even more than 20% in large strain samples. The strain lowered consistently according to the slope of the line generated between the unloading and creeping points (Fig. 3.9a). Next, the thermal stimulus was applied. Since there was no prior knowledge, the first attempt was heating the samples at 45 °C (Tg) for 1 minute. Recovery was observed in all the samples. Sample 1, 2 and 3 reached full recovery. Other samples were just partially recovered.

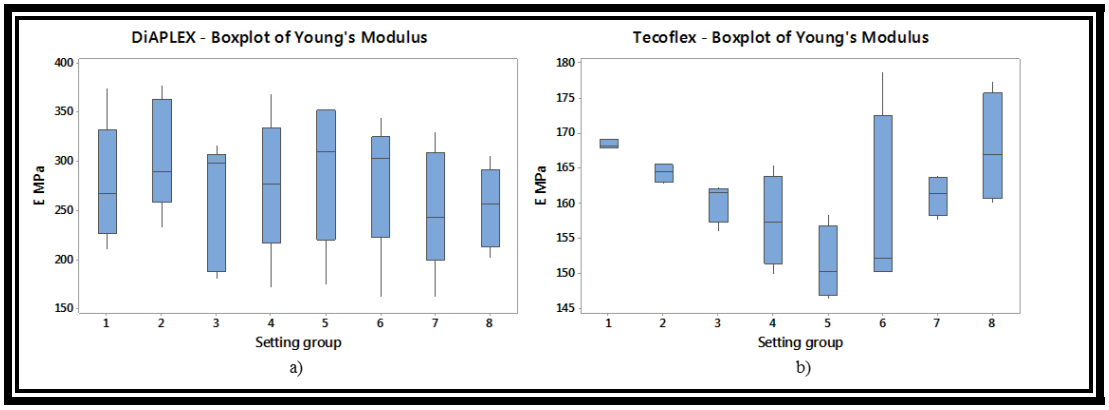

Fig. 3.8: Boxplot of Young's modulus by setting group. a) DiAPLEX. b) Tecoflex.

Partially recovered samples were submitted again to a thermal stimulus, but this time at 55 °C for 1 minute. Samples were close to full recovery, releasing all the strain energy obtained during the programming stage (Fig. 3.9a). For Tecoflex, eight samples were fabricated using settings from group 2 due to its low Young's modulus variability. After unloading, the samples were left at room temperature for 144 hours to evaluate long term relaxation by creeping effect. Fig. 3.9b shows the strain % level after each effect in the Tecoflex samples. During unloading

and creeping the strain lowered consistently, the transition slopes from maximum strain to unloading and to creeping are fairly similar. During those stages (unloading and creeping) strain % drop off from 151.5 % to between 40 and 50 %. Finally, after heating at 75 ºC for 2 minutes, the samples were recovered to a range between 1.62 % and 22.72 % of strain.

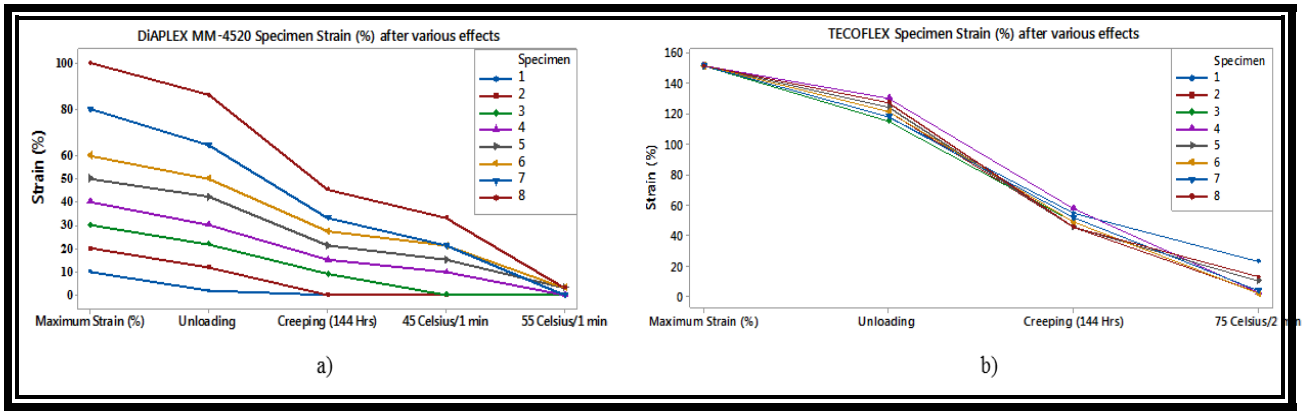

Fig. 3.9: Strain recovery after various effects. a) DiAPLEX. b) Tecoflex.

Table 3.4: Programing levels for DiAPLEX samples.

Sample	Maximum strain %
1	10
2	20
3	30
4	40
5	50
6	60
7	80
8	100

3.4.5 Fixity and Recovery Ratios

As mentioned before, instant shape fixity ratio provides an insight of the instant recovery after the samples are released from programing stress. For the instant shape fixity ratios, a “0”

indicates a poor fixity and a “1.0” indicates a perfect fixity. In Fig. 10a, it is possible to observe that samples from DiAPLEX with a maximum strain of 30 % or more, have a Rfi between 0.7 and 0.9, indicating that the samples were going back to the original shape between 10% and 30% of the total elongation. It is observed that sample 1 from DiAPLEX was elongated to a maximum strain of 10% and almost returned to the original shape with a Rfi close to 0.2. And sample 2 from DiAPLEX was elongated to a maximum strain of 20%, and had a Rfi close to 0.6. It was inferred that by increasing the maximum strain, the Rfi of DiAPLEX tended to increase and be more constant among samples because the elongations reached the plastic region of the material. As well, Fig. 10a shows that the Tecoflex samples elongated to a maximum strain of 151.5 %, had a Rfi among 0.78 and 0.86. This Rfi is consistent, attributable that all the samples were exposed to the same maximum strain. It is seen in Fig. 10b that samples from both materials suffer a high level of relaxation due to the creeping effect. Sample 1 and 2 from DiAPLEX were fully recovered. The remaining samples of DiAPLEX had a Rf1 ranging from 0.30 to 0.45. The Rf1 from TECOFLEX ranged from 0.30 to 0.36. The low Rf1 levels indicate a low level of shape fixity of the samples, caused by the elastic properties of the materials and the programming temperature below Tg. Rr was evaluated independently from Rfi and Rf1. The closer the value to “0” means that no recovery happened, and a value of “1” indicates full recovery. In Fig. 11 it is shown that samples 1 and 2 from DiAPLEX had Rr of 0 since they were fully recovered during creeping. The remaining samples from DiAPLEX had an Rr ranging 0.86 to 1. The Tecoflex samples had an Rr ranging from 0.58 to 0.97. According to the results we can infer that the SMPs have an acceptable short term and a poor long term fixity ratio, we assumed this is due the programing conditions with a T <Tg. Otherwise, the recovery ratio was in most of the samples of both material high, between 0.8 and 0.97. Some of the samples reached the full recovery and some of them partial recovery. Probably by increasing the recovery time under heating conditions the parts would reach full recovery.

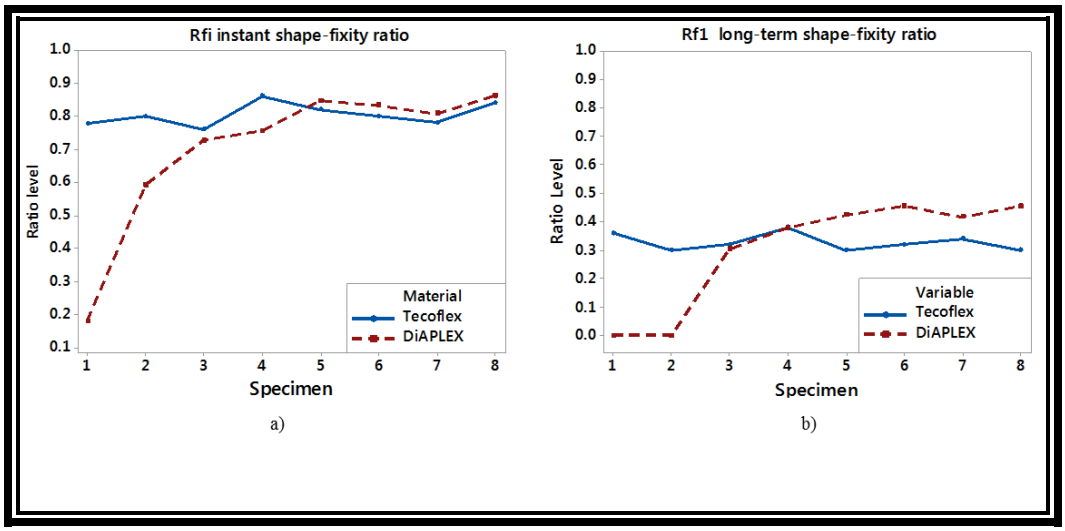

Fig. 3.10: Fixity ratios. a) Rfi ratios. b) Rf1 ratios.

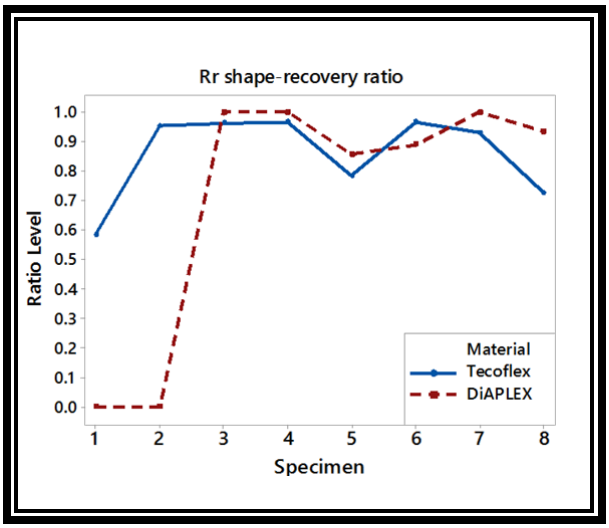

Fig. 3.11: Recovery ratios.

3.5 Conclusion

This chapter 3 provided a step forward in the integration of SMPs parts with ME 3D printing technology. Specimen fabrication using two commercial SMPs was achieved demonstrating the capacity of ME to work with various SMPs. This study also provides a reference for SMP part characterization regarding mechanical properties, recovery ratios, and SMP application design. It was demonstrated the capability of integrating SMP materials, DiAPLEX and Tecoflex, with ME using a DOE to obtain fabrication settings and identify main

effects. It is shown on Fig. 3.8 that both DiAPLEX and Tecoflex, have a low variability in Young's Modulus. This low variability is in correlation to the printing parameters that were chosen for these groups. For DiAPLEX, the optimal parameters were a printing velocity of 100 mm/s, a temperature of 235 ºC, and a layer height of 0.25 mm (setting group 8). The most influential parameter was printing velocity. For Tecoflex, a printing velocity of 75 mm/s was chosen, a temperature of 225 ºC, and a layer height of 0.27 mm (setting group 2). Here, the layer height was the most influential. Stress-strain characterization was performed on the basis of a programing algorithm. It was observed that there was a variation impact in the stress-strain curves and Young's modulus among specimens using different settings. Velocity and layer height are main factors for Young's modulus variation for DiAPLEX and Tecoflex respectively. Moreover, using a recovery algorithm, it was observed a poor long term fixity property but this was attributable that the samples were programmed at room temperature ($T < Tg$). In addition, recovery ratios were obtained demonstrating that ME is suitable in producing SMP parts that can achieve a high degree of recovery between 80 and 97 % depending on the maximum strain programmed. [1]Research findings of this chapter were reported on literature.

[1] C. A. Garcia Rosales, H. Kim, M. F. Garcia Duarte, L. Chavez, M. Castañeda, T.-L. B. Tseng, and Y. Lin, "Characterization of shape memory polymer parts fabricated using material extrusion 3D printing technique," Rapid Prototyping Journal, 2018.

Chapter 4: Toughness-Based Recovery Efficiency of Shape Memory Parts Fabricated Using Material Extrusion 3D Printing Technique

4.1 Introduction

This research aims to characterize the toughness property of thermo-responsive SMP specimens fabricated by material extrusion (ME) process and to investigate the impact of ME parameters on specimen maximum load and load-displacement curves. Moreover, to investigate the recovery efficiency based on the initial and post toughness generated by compact tension test. A Design of Experiments (DOE) with three parameters (temperature, velocity, layer height) defined the ME settings to fabricate the specimens. ME raster orientation factor was also evaluated separately. In addition, one more specimen group assisted by a clamp during the recovery process was compared with a specimen control group. After fabrication, specimens were submitted to a thermo-mechanical cycle that encompasses a compact tension test and a thermo-recovery process. Comparison studies of load-displacement, toughness and recovery efficiency of the specimens were carried out to determine the optimized fabrication parameters. It was found that ME parameters and raster orientation impacted the test results. Samples with the clamp support during recovery returned a higher toughness than samples without support. Lastly, results showed that the shape memory effect (SME) can contribute with up to 43 % recovery efficiency in a first recovery and up to 23 % in a second recovery of damaged specimens. Next sections are composed as follow. Section 4.2 corresponds to “material and fabrication” with a sub-section that describe the material properties. Section 4.3 fabrication process. Section 4.4 corresponds to result and discussion. Lastly section 4.5 includes conclusion and future work.

4.2 Material and Fabrication

The SMP used is a polyurethane based SMP, Tecoflex EG-72D. The material was obtained from Lubrizol (Ohio, USA) in form of filament with a diameter of 1.75 mm and a glass transition temperature (Tg) of 74 °C. Tecoflex is a cross-linked glassy copolymer and is thermo-responsive [20]. The ME printer (Makerbot, Replicator 2X) utilized for the part fabrication is

selected due to its demonstrated success in printing SMP filament [67]. A Design of Experiment (DOE) was carried out for the ME process. Considered factors were: nozzle temperature, which pertains to the temperature reached by the filament inside the nozzle and during deposition; velocity, which pertains to the displacement of the nozzle (printing head) during the deposition; and layer height, which pertains to the displacement of the printing head along the Z axis after the completion of one layer and the initiation of the next. Other variables involved in the process remained fixed. Two levels were determined for each factor after a prior trial and error fabrication attempts for level selection. Table 4.1 presents the fabrication factors and levels into consideration for the DOE. Table 4.2 shows the eight runs derived from the DOE. One sample per run was fabricated using compact tension specimens according to ASTM standard D5045 (Standard) as seen in Fig.4.1. Specimens were identified according the run number.

Table 4.1: Factors and levels of the DOE.

Material	Tecoflex	
Level	-	+
Temperature (ºC)	215	225
Velocity (mm/s)	65	75
Layer Height (mm)	0.27	0.3

Printing orientation could be in linear and a tilted fashion [37]. In this regard, additionally to the studied DOE factors, the printing raster orientation factor was studied independently using printing fashion [+45/-45] and [0/90] as seen in Fig. 4.1d-e [37, 40]. In this regard, 9 specimens at [+45/-45] (default setting) and 3 specimens [0/90] were fabricated. In both cases, once a layer is completed the raster orientation rotates 90° to create an orthogonal structure by continuing the alternation up to the part completion. Furthermore, external assistance on specimens during recovery was evaluated. In this respect, 2 more groups (test and control) were fabricated to evaluate the toughness on specimens assisted with clamp during the recovery process.

Table 4.2: DOE runs.

Run	Temperature (°C)	Velocity (mm/s)	Layer height (mm)
1	225	65	0.3
2	225	75	0.27
3	215	65	0.27
4	215	75	0.27
5	225	65	0.27
6	215	65	0.3
7	215	75	0.3
8	225	75	0.3

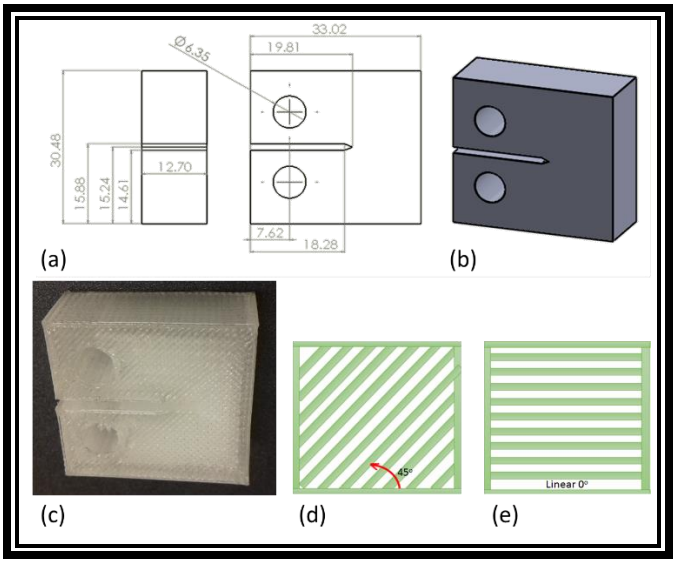

Fig. 4.1: Compact tension specimen. a) ASTM D 5045. b) Specimen model. c) Tecoflex specimen. d) Raster orientation at [+45/-45]. e) Raster orientation at [0/90].

4.2.1 Material Properties

The load-displacement curve of the material was characterized using compact tension specimens. The tests were conducted using an INSTRON 5969 with extension rate of 10 mm/min at room temperature according to regulations, with a maximum displacement of 30 mm

(Standard). Customized fixtures were made to fit into the INSTRON to test the compact tension specimens. Pre-cracking was done with a hacksaw creating a deepness of 4.5 mm, as well as scratching the top and bottom surface of the sample along the path cracking should follow to ensure a plain strain analysis.

4.3 Proposed Methodology

4.3.1 Evaluation Procedure of SME Assisting Recovery

To evaluate recovery efficiency of the 3D printed SMP part, a SME thermo-mechanical cycle was performed. The SME thermo-mechanical process consisted of two main stages: the programming stage and the recovery stage [22]. The programming stage pertains to modify the original form of the part, by causing a deformation or a damage, into a temporary new shape. The new shape will be fixed until the start of the recovery stage. Then, the specimen will be recovered back to its original shape after the application of a thermal stimulus. For the programming in this study, the specimens were submitted to the compact tension test causing a damage in the central region of the part. The displacement was set to 30 mm to leave a non-damage region for supporting the recovery mechanism to the original shape. Afterwards, the specimens were stimulated by heating it to its glass transition temperature to be recovered. Once the damaged specimens were fully recovered to its original shape, the samples were cooled down. Below is described the employed procedure to evaluate the recovery efficiency in SMP specimens.

4.3.1.1 Programming Procedure

i. Set the part in the testing machine for compact tension test. Then, apply tension at a constant speed rate on the compact tension specimen causing fracture mode I (opening mode) [85]. Register the toughness.

ii. Stop the test once the specimens reach their maximum displacement. An undamaged section of the specimen need to be kept for recovery with thermal treatment.

iii. Remove the specimen from the testing machine, keeping a new temporary shape with a fracture mode I.

4.3.1.2 Recovery Procedure

iv. Apply the recovery stimulus. In the present work it was used a thermal energy. To heat the sample about the Tg of the SMP material. Tecoflex specimens were heated to 74 ºC for 2 minutes.

v. This step is exclusive for specimen with clamp assistance after the sample is recovered. Once the specimen is cooled down, fixe the clamps to the specimen and heat up the specimen to 74 ºC for 1 more minute.

vi. Repeat steps from i to iii for the recovered samples.

vii. Calculate the recovery efficiency using the next equation:

Recovery efficiency(%)= (Toughnessrecovered / Toughnessinitial) x 100)…….(4.1)

The use of initial and post toughness in Eq. (4.1) is suggested by the authors to respond to the necessity of quantifying the recovery level of the initial conditions on the sample. Eq. (4.1) provides a metric to assess the polymer bonding occurring at the realign fracture surfaces of the compact tension samples after recovery. Toughness was calculated from the load-displacement data generated in step (i) by obtaining the area under the corresponding curve using MATLAB software.

4.4 Results and Discussions

4.4.1 Process Factor Impact on Load-Displacement Curves

DOE results obtained from the tested specimens are analyzed in this section. Maximum load is selected as a response since it provides information to understand failure onset. ANOVA (general linear model) test results (P-value) are presented in Table 4.3 which includes individual factors and interaction through order of 2 factors in descending order of significance. One-Way ANOVA for factor level is presented in Table 4.4. In addition, Fig. 4.2 shows the main effects plot results with maximum load as a response. It is observed that among the factors considered

the temperature has the biggest impact (Fig. 4.2) and higher significance (Table 4.4) on maximum load, followed by layer height, and lastly velocity. Temperature lower level resulted in a mean response of 255.57 N and the upper level 458.32 N, which is a range of 202.75 N. The velocity levels (Table 4.4) influence in a much lower proportion (poor significance) on the maximum load compared to temperature. With the velocity lower level, a mean of 346.03 N was obtained and with the upper level a mean of 367.80 N, a range of 21.77 N. This range is just 10.73 % of the temperature effect. Layer height lower level had a mean of 418.28 N and an upper level 295.58 N, a difference of 122.7 N between the two settings. That is 48.01 % from the range of influence caused by the temperature. It is inferred that the higher range of influence in the maximum load values caused by the temperature compared to velocity and layer height is presumably consequence of the major amount of material deposited. Temperature upper level increased the maximum load, since it reduces the viscosity of the material and it flows more easily out of the nozzle depositing more material during the process. To support that, specimens 1,2,5,8 fabricated with upper temperature level (Table 4.2) resulted a weight average of 10.606 g, in contrast specimens 3, 4, 6 and 7 fabricated with lower temperature registered an average weight of 10.385 g. The higher amount of material deposited causes a better layer-to-layer bonding. Observing the interaction plot (Fig. 4.3), it is found that exists a minimum interaction among temperature and velocity and temperature and layer height. However, it is not the case with velocity and layer height. The response variation corresponding to the velocity level differs its tendency influenced by the levels of the layer height causing an intersection in the interaction plot (Fig.4.3) at the area corresponding to both variables. Specifically, at a high level of layer height and velocity the material deposited do not fill the gap among parallel paths and generates poor layer bonding. Although level significance of velocity is poor (Table 4.4), layer height and velocity interaction significance increases (Table 4.3) causing poor layer bonding and lower maximum load values. As we could observe the factor level during the ME process clearly influenced the variation in the maximum load of the specimens.

Table 4.3: ANOVA (general linear model).

Source	P-Value
Temperature (ºC)	0.347
Layer height (mm)*Velocity (mm/s)	0.456
Layer height (mm)	0.500
Temperature (ºC)*Layer height (mm)	0.580
Temperature (ºC)*Velocity (mm/s)	0.854
Velocity (mm/s)	0.888

Table 4.4: One-Way ANOVA for factor level.

Source	P-Value
Temperature (ºC)	0.090
Layer height (mm)	0.346
Velocity (mm/s)	0.872

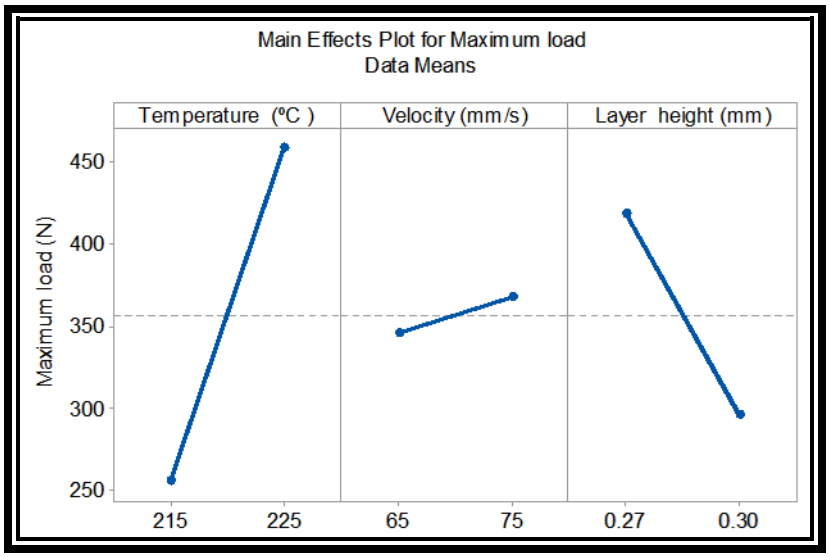

Fig. 4.2: DOE Main effect plot.

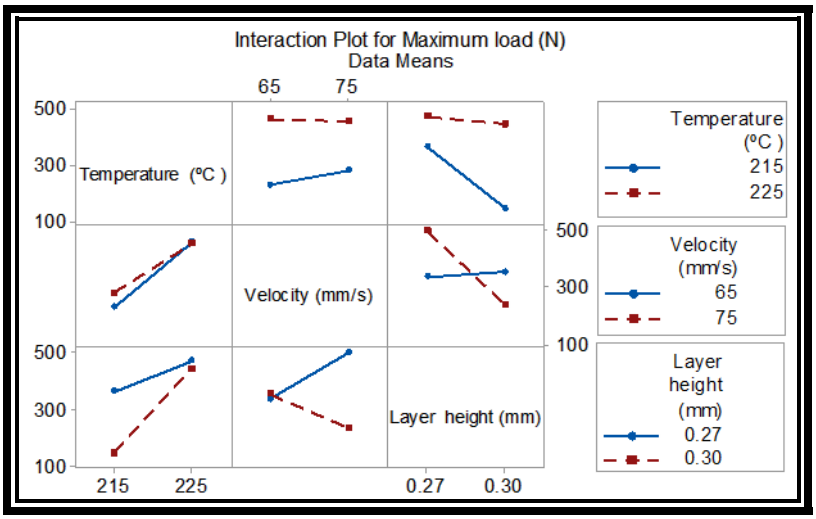

Fig. 4.3: Interaction plot.

4.4.2 Load-Displacement Curves Analysis

Fig. 4.4 presents the load-displacement curves for DOE specimens identified as its corresponding run setting number. The linear region at the initial section of the curves reflects variation. In addition, variation occurring among specimens at the maximum load point was also noticed. The maximum load is a good insight of ME parameter influence on material property: for example, specimen 2 required approximately six times the load required by specimen 6 to initiate a crack propagation. Rupture points were not able to generate since the test was stopped when displacement reached 30 mm. Moreover, the curves appear to be grouped in three regions according to the maximum load. The first group is composed from specimens with setup 1&2 with 579.9 N and 600.53 N, respectively. This group is characterized for high level of temperature which reduces the material viscosity causing the material to flow out from the nozzle easily, and to generate a better polymeric arrangement improving the layer bonding interfaces. The second region encompasses specimens with setup 3, 4, 5 and 8 with values in a range between 300 to 400 N. This group specifically is characterized by being fabricated using low level layer thickness in combination with both levels of temperature. The use of low level layer thickness (low air gap) compensates the layer bonding losses due to low level temperature. The lower the air gap lead to more layers of material being deposited during fabrication resulting

in a better layer bonding (under Table 1 conditions). The third region includes specimens fabricated using setups 6 and 7 with 130.34 and 175.06 N respectively. Therefore, based on previous results, it was deducted that the variable levels influenced on load-displacement curve behavior. This third group is characterize of being fabricated with higher level of layer height (high air gap) which causes poor bonding layer bonding since the material amount (under the setting condition from Table 1) do not fill properly the air gap between layers. Therefore, material amount and temperature conditions vary the polymeric arrangement occurring at the layer interface leading to different load-displacement curve behavior.

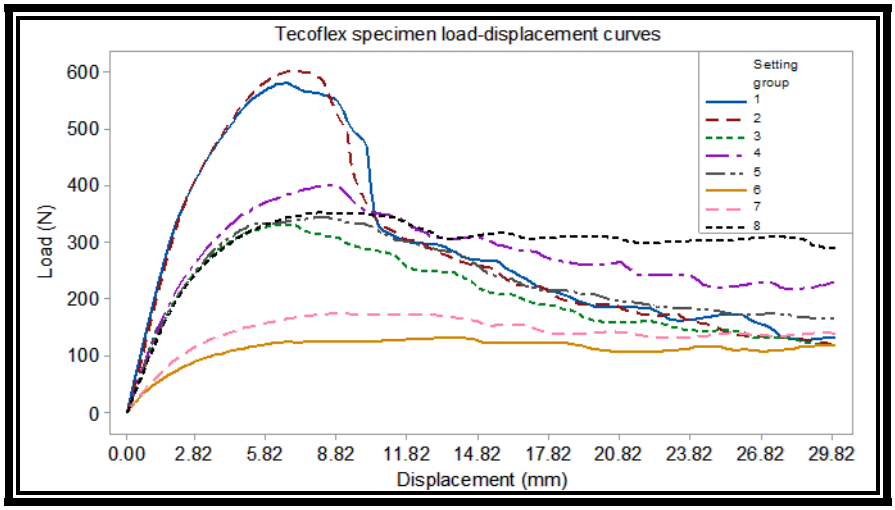

Fig. 4.4: Specimen load-displacement curve from DOE.

After heating the samples from the DOE at 74º C for 2 minutes, they were able to recover their original shape and to close the ruptured surface. Figure 4.5 shows a damaged specimen before and after recovery. Then, the samples were cooled down and subjected to the compact-tension test under similar conditions of virgin samples. Figure 4.6 shows the load-displacement curves of the recovered specimens. It is observed that variation among specimens fabricated using different settings persist in the recovery parts. By observing the graphs, the fabrication settings have an impact in toughness on recovered specimens. While specimen 6 continues having the lower toughness, in contrast to the virgin samples, specimens 8and 4 have the higher

toughness. This is attributed to the fabrication settings of specimens 8 and 4 which creates a layer arrangement that allows higher residual stress concentration stored in the undamaged region after the compact-tension test. This stress is released during the recovery causing a stronger realign of the fracture surfaces. In general, residual stress concentration generated during the compact test varied according the polymeric arrangement for each specimen during fabrication. This cause a different strain energy level relaxation during recovery leading to different realign of the fracture surfaces. Based on Figs. 4.4 and 4.6, no correlation among first and post recovery load displacements curves is observed.

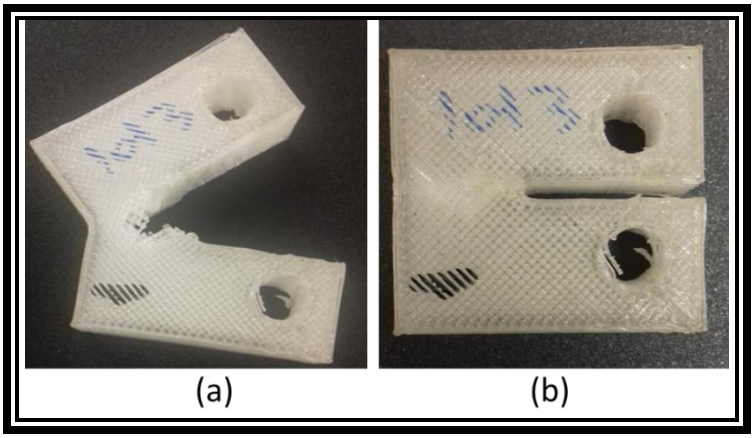

Fig. 4.5: Tecoflex specimen: a) after compact tension test, and b) after recovery process.

Another factor of investigation was the printing raster orientation. Specifically, for this investigation, there were used settings from DOE run 2 for the fabrication of 9 specimens with raster orientation [+45, -45] and 3 linear specimens [0/90]. Figure 4.7 shows the average load-displacement curves of both groups revealing that load-displacement curve is slightly affected by the printing orientation, leading the samples with [+45/-45] deposition orientation had a higher toughness than [0/90] specifically after the second half of the displacement. This effect can be attributed to the nature of the crack propagation, while the carrying loads of the layer configuration [+45/ -45] is well distributed in each layer, the load in the [0/90] configuration tend

the to be supported in a higher degree by the layers which deposited material forms 90 degrees with respect the crack propagation.

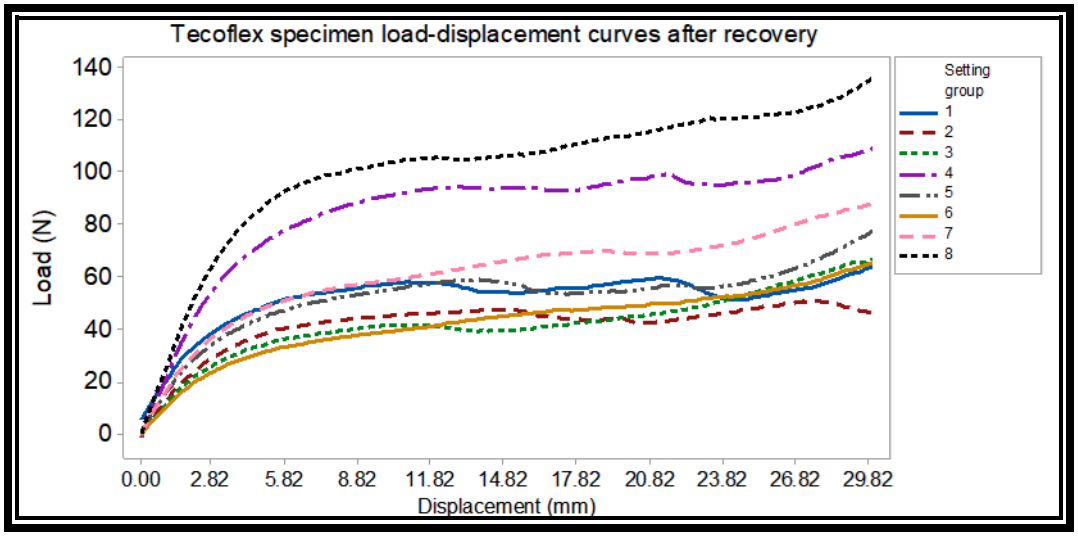

Fig. 4.6: Load displacement curves of recovered specimens.

Moreover, the influence of an auxiliary external force in the recovery process was investigated. 6 samples with settings from DOE run 2 were fabricated and submitted to the compact tension test. After a recovery at 74 ºC for 2 minutes, 3 of the samples were fixed with a clamp and heated at 74 ºC for 1 minute more and the other 3 samples were only heated to 1 more minute. Figure 4.8 shows the results reveling that the group with clamp show a slightly better performance that the group without clamp. This can be seen especially in the maximum load to initiate a crack propagation. It was inferred that the clamp allows to create better conditions for polymer chain re-arrangement between surfaces of the fracture. In addition, for reference purposes the load-displacement average curve of the 6 virgin specimens was included in Fig. 4.8.

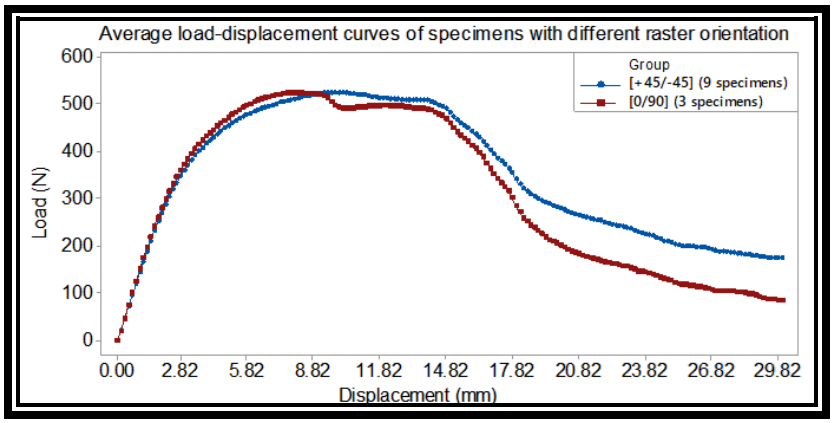

Fig. 4.7: Load-displacement curve with raster orientation of [+45/-45] and [0/90].

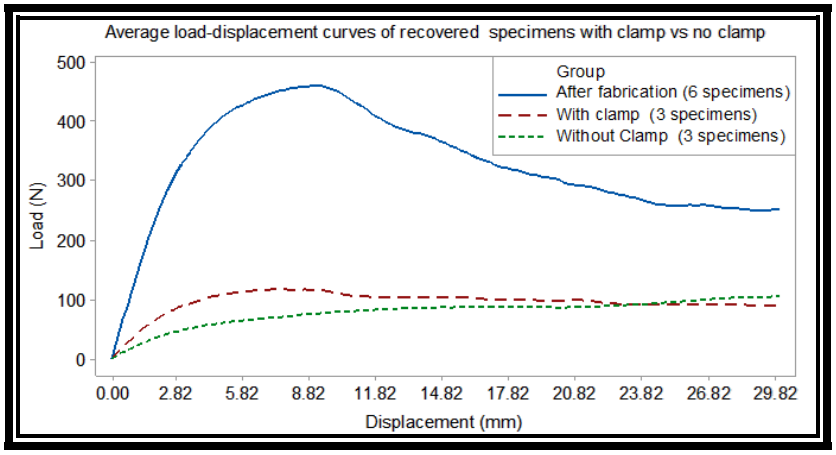

Fig. 4.8: Load displacement curve comparison between recovered specimens assisted with clamp and without clamp.

4.4.3 Toughness and Recovery Efficiency

Recovery efficiency of the thermo-responsive SMP assisted by the SME was obtained from performing the calculation using Eq. (4.1). Fig. 4.9 shows the toughness results for each DOE specimen from the first compact-tension test and its corresponding toughness results from the recovered samples. Although the toughness after recovery appears to be marginally more stable, it can be observed toughness variation among specimens during the first test and second test. Fig. 4.10a presents the recovery efficiency results, specimen 7 yielded the highest efficiency with 43.27 % followed by specimens 6 and 8. Specimen 2 obtained the lowest recovery efficiency although it supported the maximum load during the first test.

Specimens 6, 7 and 8 were selected to investigate a second healing cycle since they resulted with a significant higher efficiency that the rest of the specimens. Fig. 4.10b shows the healing efficiencies of the second cycle, where efficiency from specimen 6 drops from 38.10 to 23.31 %, specimen 7 from 43.28 to 22.86 %, and specimen 8 from 34.19 to 16.90 %. All the compact tension specimens were able to be fully recover their original shape by heating them during the 2 cycles even the remaining undamaged region had a thickness no more than 3 mm.

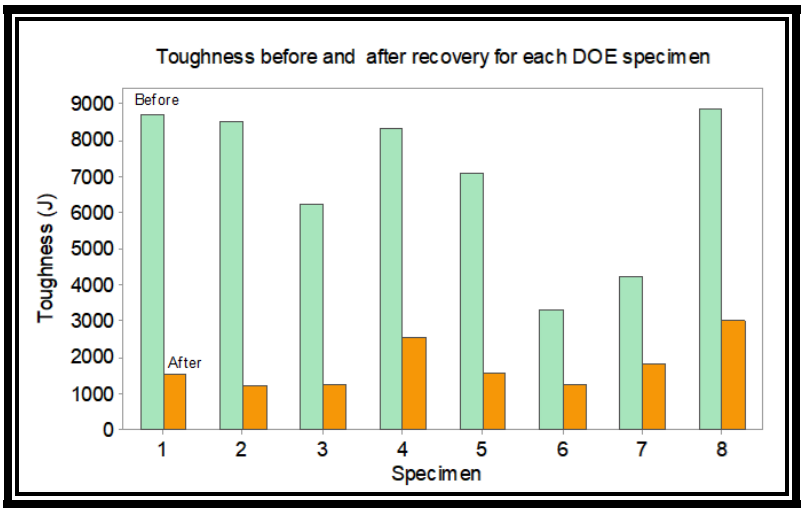

Fig. 4.9: Toughness before and after recovery.

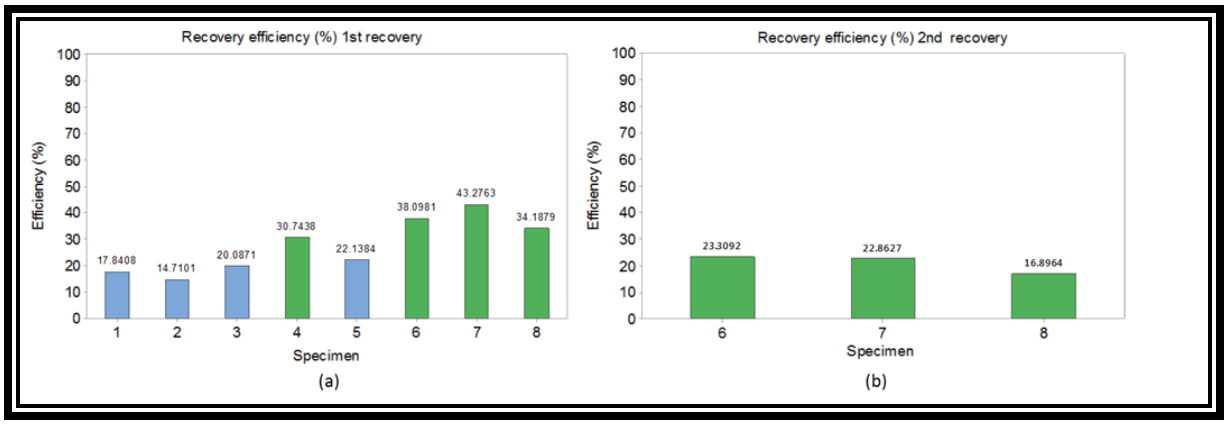

Fig. 4.10: a) Recovery efficiency by setup (1st recovery). b) Recovery efficiency after a second recovery cycle.

4.5 Conclusion

This chapter 4 demonstrated the capability to fabricate SMP specimens with ME using a design of experiment (DOE). Load displacement curve and recovery efficiency was investigated to various specimens fabricated with different parameters settings. Studied factors were nozzle temperature, nozzle velocity, and layer height. Temperature contributed the most to the maximum load reached during compact-tension test. In addition, raster orientation factor was investigated separately resulting in a difference between load displacement curves of specimens with a raster orientation of [+45, -45] and [0,90] degrees. In other test, a slightly higher performance of toughness was obtained in specimens by assisting the recovery process with a clamp compare with specimens without assistance. Toughness values allowed to calculate recovery efficiencies in a way that, to the best of the knowledge of the authors, had not been previously considered. Furthermore, it was demonstrated that the shape memory effect of Tecoflex SMP can recover a fracture mode I damage up to an efficiency of 43 % in a first recovery cycle and up to 23 % in a second cycle in specimens produced by ME technology. The results in this study could be considered and enhanced in shape memory thermally assisted self-healing works. In future studies, this SMP can be complemented by adding self-healing polymers to improve and reach higher recovery efficiencies. [2]Research findings of this chapter were reported on literature.

[2] C. A. Garcia Rosales, H. Kim, M. F. Garcia Duarte, L. Chavez, T.-L. B. Tseng, and Y. Lin, "Toughness-based recovery efficiency of shape memory parts fabricated using material extrusion 3D printing technique," Rapid Prototyping Journal, 2018.

Chapter 5: 3D printing of Shape Memory Polymer (SMP)/Carbon Black (CB) nanocomposites with electro-responsive toughness enhancement

5.1 Introduction

In this chapter, a simple approach to 3D printing of carbon black based shape memory polymer nanocomposites (SMP/CB) with toughness improving capabilities during programing stage using electrical stimulus is reported. Conductive SMP/CB nanocomposites, consisting of commercial SMP filled with conductive CB nanoparticles, were fabricated using solvent casting and single screw extrusion processes. Subsequently, material extrusion (ME) technique was used to 3D print dog bone type IV specimens for tensile test and electrical stimulus. It was found that SMP/CB electrical conductivity can be tuned by the filler fraction. In addition, electrical current passing through SMP/CB nanocomposites causes temperature increments and changes on material strength condition. Temperature profiles at various electrical current levels are reported. Moreover, Young's modulus and toughness of the 3D printed specimens subjected and not subjected to electrical current are presented. It was observed that conductive SMP/CB specimens responded to electrical current stimulus by increasing their toughness four times higher than with no current applied during tensile test. This chapter is a reference for rheological and conductive properties of SMP/CB nanocomposites fabricated by ME 3D printing process. Next sections are composed as follow. Section 5.2 corresponds to "material and fabrication" with a sub-section that describe the material properties. Section 5.3 is called "proposed methodology". Section 5.4 corresponds to result and discussion. Lastly, section 5.5 includes conclusion and future work.

5.2 Material and Fabrication

The thermo-responsive SMP pellets (DiAPLEX MM-4520®, SMP technologies, Japan), is a cross-linked glassy copolymer with a glass transition temperature (T_g) of 45 ºC , and a melting temperature of 200 ºC [67, 86]. This commercial SMP was selected because their glass transition and melting temperatures are adequate for the ME process parameter range. Carbon black nanoparticles (CB) (Ketjenblack® EC600JD supplied by Akzo Nobel, USA) were chosen

as conductive nanofiller due to their high conductive properties over other materials, and its performance shown in previous polymer nanocomposite studies [27, 47, 52, 53]. Uniform and continuous electrical conductivity SMP/CB nanocomposites with various CB content (1, 3, 5, and 7 wt.%) were obtained by blending the SMP with CB. SMP pellets and CB are mixed with N-dimethylformamide solvent (DMF, OmniSolv®, USA) via solvent-casting method as shown in Fig. 5.1. The solution is prepared by dissolving the SMP pellets in DMF (1:8 weight ratio). The solution is then placed in a silicon oil bath at 200 ºC for 3h. After the pellets are fully dissolved, the CB is added to the solution. Prior, the CB are dispersed in DMF (1:30 weight ratio) by bath-sonication at 40 kHz for 30 min. Then, CB/DMF is mixed with SMP/DMF solution by tip-sonication at 40 kHz for 30 min. Homogeneous solution is poured onto a glass substrate and heated to a temperature of 100 ºC for 12 h to evaporate the DMF. The procedure results in a thin sheet of SMP/CB nanocomposite, and these casted nanocomposites are cut into pieces for conductivity calculation. Conductivity was calculated on SMP /CB casted films (20 × 40 mm with 0.42 mm average thickness) with various CB content (1, 3, 5, and 7 wt.%) from resistance measurements (IET/QUADTECH 1910/1920 1 MHz LCR METER) and Eq. (5.1).

$$\rho = RA/l \quad \text{.....(5.1)}$$

Where R is the electrical resistance of a uniform specimen of material, l is the length between the tip of the clapms of the LCR meter used for resistance measurements, and A is the cross-sectional area of the specimen. A master batch SMP/CB composite (SMP-7 wt.% CB) is combined with SMP (1:0.33 weight ratio) to be mechanical mixed and extruded as a filament (SMP with 5 wt.% CB) using a single screw extruder (Filabot filament extruder, Filabot®). The material was passed through the extruder 2 times at 200 ºC and 2 times at 160 ºC using a 1.7 mm diameter nozzle to obtain conductive filament suitable to be use in the ME process. Final filament had uniform material distribution (good mixing), acceptable cross section diameter, no bubbles or voids, and low rate filament breaking during ME process feeding. The resultant uniform filament with an average cross section diameter of 1.64 mm is then used in a ME 3D printer (MAKERGEAR M2) to print test specimens (Dog Bone type IV) according to ASTM

standard D638 [20, 84]. Prior trial and error ME fabrication attempts leaded to process parameters selection. Table 5.1 presents the parameters settings used for specimen fabrication. When sample is finalized, the bed temperature is turned off leading the sample to cool down to ambient temperature in order to be removed.

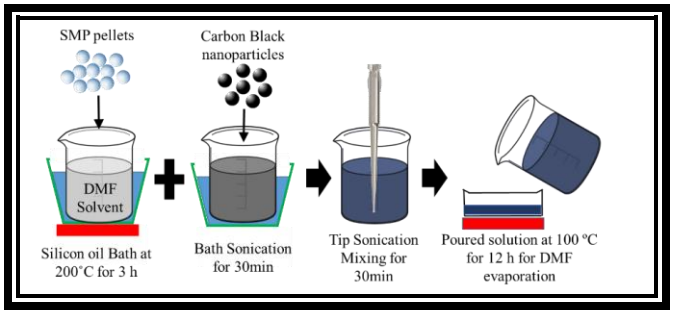

Fig. 5.1: SMP/CB nanocomposites through solvent casting.

5.2.1 Material Tensile Property

The tensile property of the SMP/CB material was characterized using dog bone type IV specimens. Six replicas of a Dog Bone type IV (five used as controls and one under electrical stimulus) according to ASTM standard D638 (Fig. 5.2a) were fabricated using ME. Actual 3D printed specimen is shown in Fig. 5.2b. The tensile test was conducted on an INSTRON 5969 load frame using an extension rate of 5 mm/min, up to a maximum extension of 50 mm, and a holding grip of 25 mm on each end of the 115 mm long dog bone. Tensile strength measurements were carried out at room temperature which is below the Tg of the SMP material. Stress-elongation curves were generated.

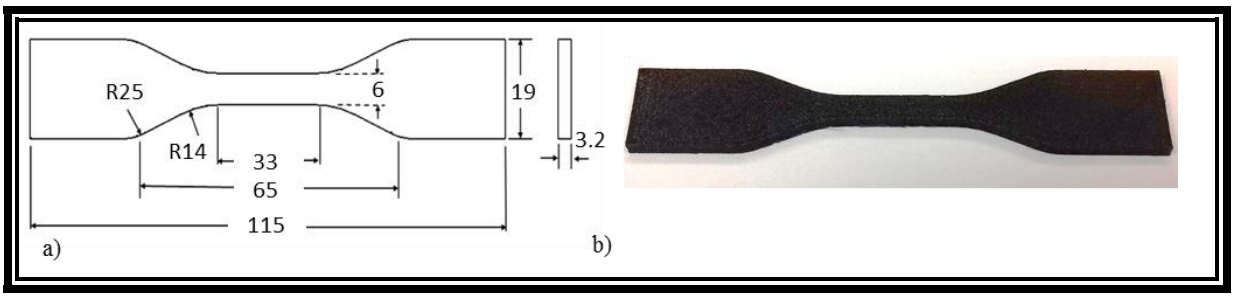

Fig. 5.2: Dog bone specimen. a) Schematics Type IV (mm). b) SMP/CB specimen.

5.3 Proposed Methodology

5.3.1 Programing Process

The programming stage as shown in Fig. 5.3 [22] indicates modifying the original form of the part causing a deformation by mechanical stress application. The programing procedure on control samples was carried through tensile test as described above. In the specimen subjected to electrical test, an additional step was added. This consist of applying electrical current trough the specimen during the elastic deformation region of the tensile test, see Fig. 5.3. A schematic illustration of experimental setup for electrical stimulus application is presented in Fig. 5.4. A thermocouple (type K) was attached for temperature monitoring, and terminals were connected to DC power supplies with 300 V output capacity which are switch on and off at specific times during tensile test. Once the specimens reached the fracture point the specimen was unloaded.

Table 5.1: ME process parameters.

Parameter	Value
Temperature (ºC)	230
Velocity (mm/s)	80
Layer Height (mm)	0.25
Platform temperature (ºC)	60
Infill (%)	100
Filament diameter (mm)	1.7

5.4 Results and Discussions

5.4.1 Nanocomposite Conductivity

Fig. 5.5 shows the conductivity output on samples with various contents of CB. The conductivity value is an average of sampling 5 specimens of each composite. It can be observed that conductivity increases as CB % increases. A peak electrical conductivity of 9.17 S/m was

observed in the SMP/CB sample with 7wt.% CB concentration. This is a presumable consequence of a higher density of CB distributed in the polymer matrix.

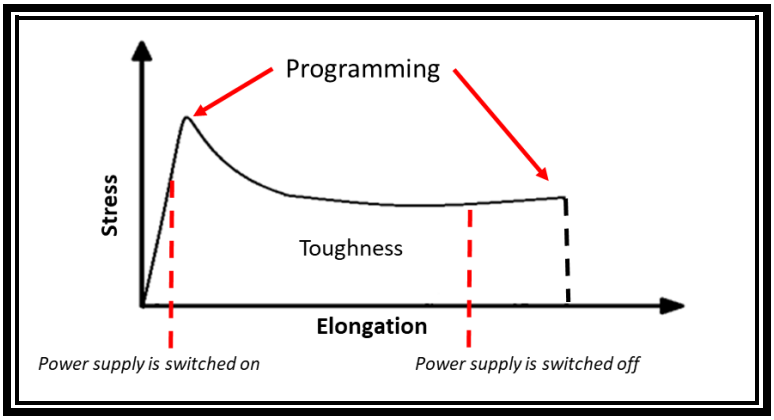

Fig. 5.3: Programing stage of SMP/CB specimen.

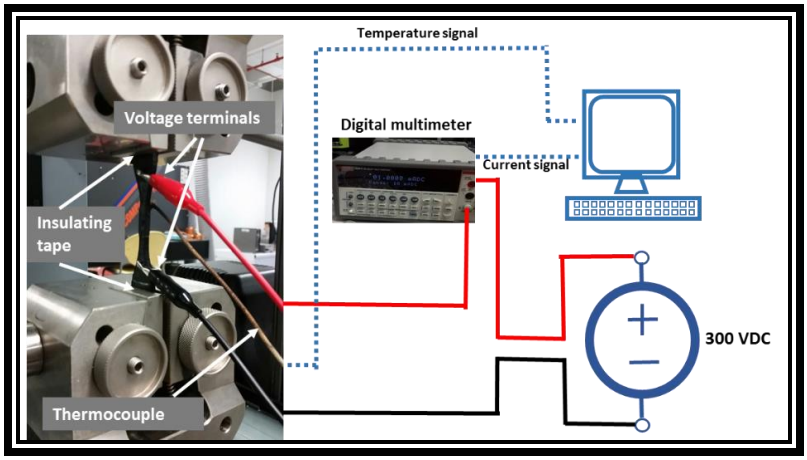

Fig. 5.4: Setup for electrical stimulus.

Moreover, temperature behavior response to DC current was evaluated by testing different currents levels through SMP/CB with 5 wt.% CB, Fig. 5.6. Samples subjected to higher current stimuli presented higher rate of temperature increments, once the temperature stabilized the samples were able to keep it for a longer time. The samples were able to hold its structure during the electrical current test.

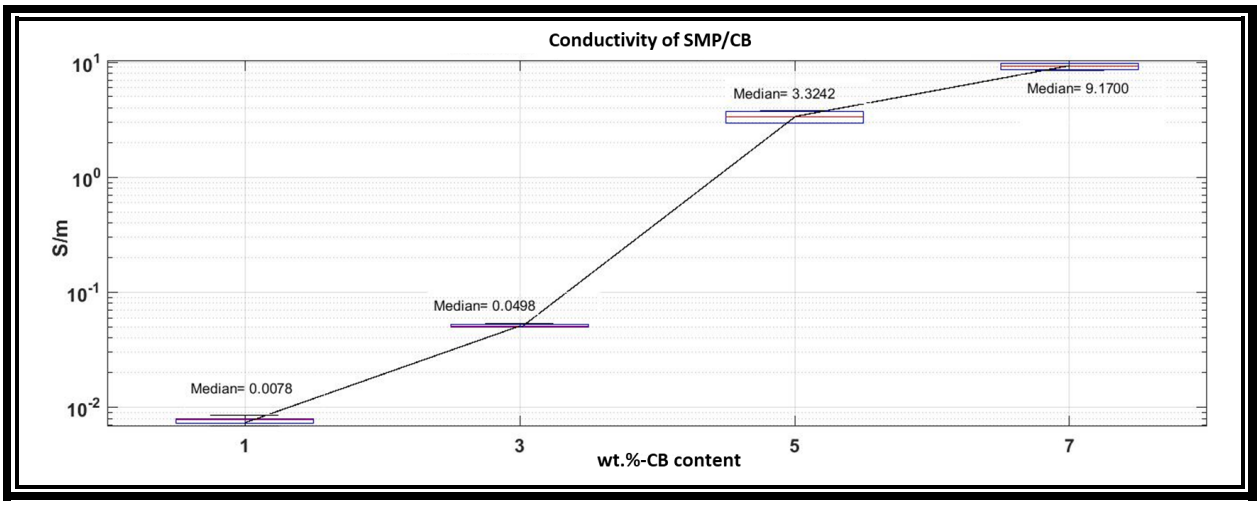

Fig. 5.5: Conductivity on SMP /CB (1, 3, 5, and 7 wt.%-CB) solvent casted films.

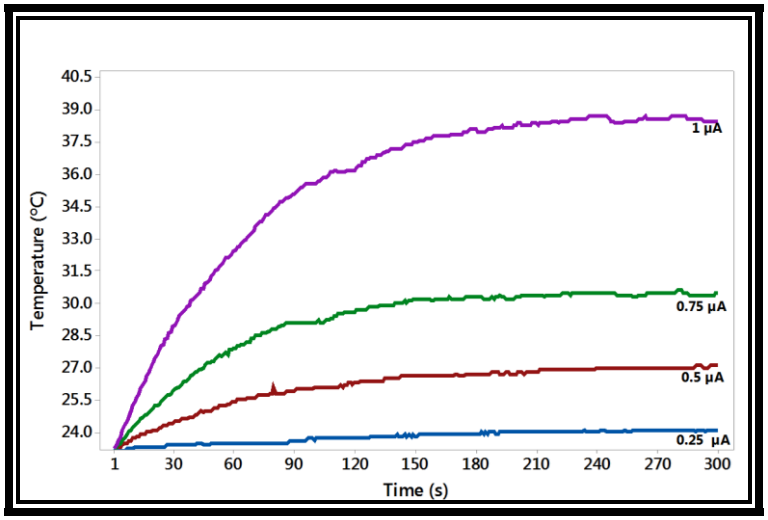

Fig. 5.6: Temperature profile on SMP/CB (with 5wt.% CB content) films (20X10X0.42 mm) at various current levels (0.25, 0.5, 0.75, 1.0 µA).

5.4.2 Filament Conditions

Preliminary filament extrusion attempts in the ME process were performed to obtain a better process insight. Filaments with CB content of 1 %, 3% lost their conductivity properties even when exposed to 1000 VDC with resistances higher that 120 MΩ, which made them not suitable for this study. This poor conductivity filament is attributed to nanocomposite blending conditions at low temperature (160 ºC) and low-pressure since extruder has only one extrusion screw and a single heating chamber. Otherwise, SMP/CB with 5 and 7% filament presented

conductivity properties of 0.1822×10-3 and 3.83×0-3 S/m respectively. It appears that the filament extrusion process affects conductivity properties of these composites. Preliminary ME process attempts showed that SMP/CB filament with 5 wt.% CB contents was too soft for continuous material extrusion causing material obstruction in the extrusion head during deposition. Conversely, SMP/CB filament with 7 wt.% CB contents was too brittle causing high breaking rate during the ME extrusion process. To overcome this poor stiffness filament conditions, it was decided to fabricate an additional master batch SMP/CB composite (7%-CB) and mechanically mix it with SMP (1:0.33 weight ratio) in the single screw extruder to produce SMP/CB filament with 5 wt.% CB content using a single screw extruder under conditions presented in section 5.2.

5.4.3 Stress-Elongation and Toughness Results

The mentioned extrusion process allowed us to obtain filament with ME printable conditions. This filament was fed into the ME process to obtain dog bone specimens for tensile testing. Fig. 5.7 present tensile test results of the 3D printed specimens that include the stress-elongation curves (with current and no current stimulus applied), tensile toughness, temperature profile, and current profile.

SMP control specimens presented an average Young's modulus of 160.26 MPa (standard variation of 12.99 MPa), and a 9.45% (standard variation of 0.45%) elongation at break (Fig. 5.7a). Similar stress-elongation behavior on samples is due to same fabrication setting that lead to similar amount of deposited material and layer interface bonding (polymeric arrangement). All the specimens were tested at room temperature conditions. For specimen subjected to an applied current (Fig. 5.7a), it was observed that Young's modulus is similar to the control since the test conditions up to 18 s from start point were similar. After current application (at 18 s), specimen temperature increased gradually up to 33.4 ºC, thus changing the material strength. The gradual increasing on specimen temperature was caused by the resistive heat generated on the surface of embedded CB, heating up the surrounding polymeric chains through conductive heat transfer

causing a change from stiff solid to soft solid state in the polymeric chains. Therefore, stress-elongation curve of sample under electrical condition behave different compared to controls (Fig. 5.7a). A decrease in the Young's modulus of the sample was observed after the power was switched on. The plastic region behaved steadily as elongation increased. A maximum strain of 44 % was obtained until rupture occurred. This elongation was the maximum strain obtained from all the specimens tested under the same tensile conditions and reflects the super plasticity properties of SMP/CB nanocomposites when submitted to an electrical stimulus during programing even at temperatures below the material's Tg.

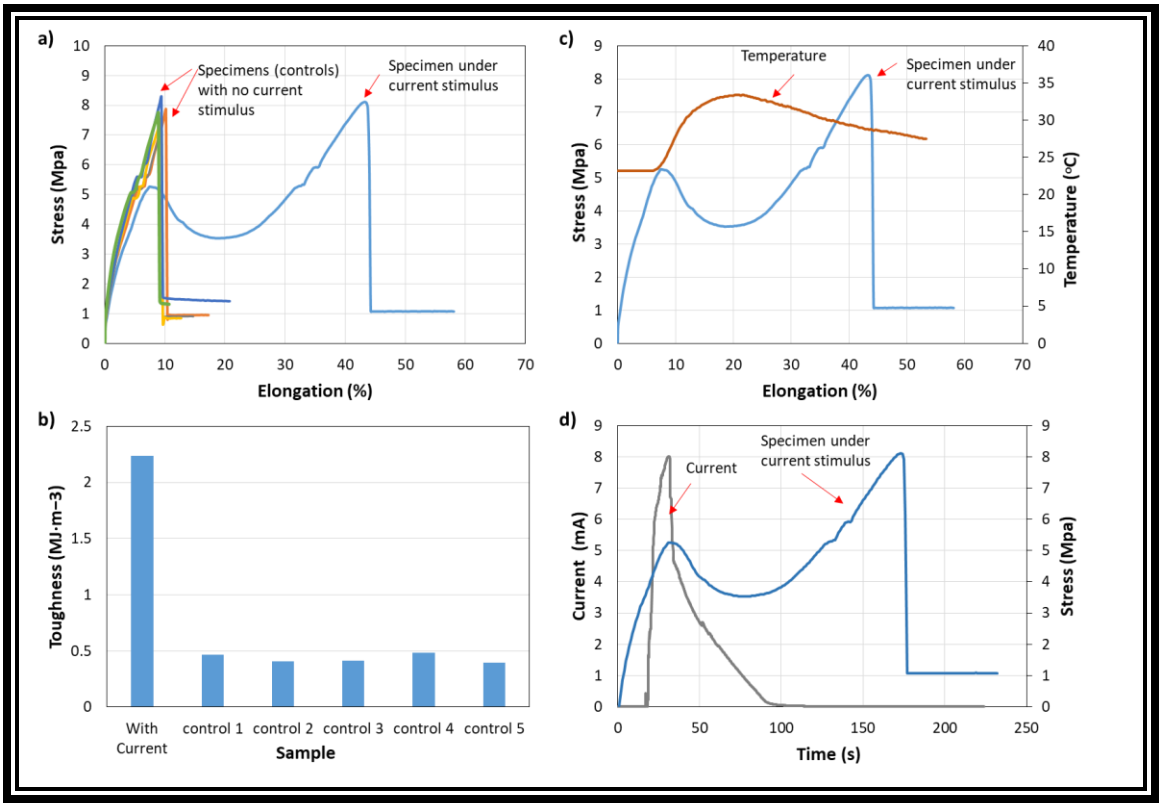

Fig. 5.7: Tensile test results. a) Stress-elongation curves. b) Temperature profile and stress behavior. c) Toughness of samples. d) Current profile and stress behavior.

In Fig. 5.7b, it is observed that toughness can be improved at least 4 times on SMP/CB 3D printed specimens during tensile test by applying a controlled current. The reason of a lower toughness on SMP/CB control specimens is attributable that specimens were tested at room

temperature which is below the glass transition temperature (Tg) of the SMP matrix. The SMP matrix contributes to maintain the shape of the sample when the temperature (T) is lower than its glass transition temperature (Tg) but losses its strength above Tg. Tensile toughness on specimens when T > Tg during the plastic zone increases since the polymeric matrix has lost its stiffness and elasticity increases. Fig. 5.7c shows the stress curve and temperature profile of sample when electrical current was applied. Both curves match, when temperature reach a maximum value during plastic region the stress reaches a minimum according to the polymeric chains conditions. Finally, Fig. 5.7d presents stress and current behavior of sample under electrical test. The current increases rapidly reaching 8 mA in few seconds after the power supply was turned on, heat increased exponentially, then it was decided to turn off the power supply (on second 32) once the stress started to decrease to avoid the material overpassing Tg and start melting. Even after the current was cut off, a temperature increase was observed as heat power generated continued dissipating along the material sections reaching the thermocouple and instant later.

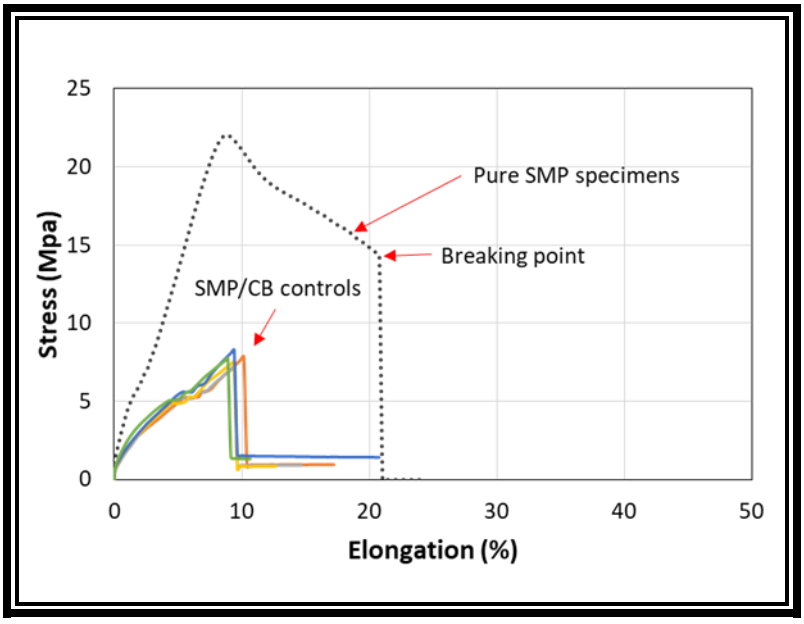

Fig. 5.8: Stress-elongation comparison between pure SMP specimen and SMP/CB control specimens.

Although conductivity properties on SMP/CB specimens were demonstrated, addition of CB to the polymeric matrix is detrimental to the tensile ductility. In this regard, it is shown in Fig. 5.8 a comparison between an average-stress strain curve obtained from five replicas of a pure SMP Dog Bone type IV (according to ASTM standard D638) and the strain stress curves of the SMP/CB control specimens with 5 wt.% of CB. It is observed that the elongation of SMP/CB decrease around 50 % compared to pure SMP elongation. Moreover, Young's modulus decreased with CB additions on controls. The ductility reduction on SMP/CB controls is caused by the dispersion of CB in the polymeric matrix affecting the interfacial interaction between polymeric chains.

5.4.4 SEM Analysis

SEM was performed to analyze surface topography of SMP/CB 3D printed specimens. SEM images of bottom and top surfaces, and cross section regions of specimens were obtained and are shown in Fig. 5.9. On the bottom surface, shown in Fig. 5.9a-b, it can be observed the deposited material interface and CB agglomerations caused by CB exposed on the surface of the deposited material. Fig. 5.9b shows that one of the bigger agglomeration detected is around 50 um long. In addition, on the remaining area of the bottom surface can be observed well distributed agglomerations no longer than 5 um. In cross section areas, shown in Fig. 5.9c, voids are detected among material layers ranging from approximately 60 to 120 um long. Voids were expected since they are associated to the layer by layer fashion fabrication. However, beside voids, the significant larger captured area, Fig. 5.9c, shows a uniform material distribution without cracks or porosities detected indicating proper material adhesions. In the top surface, as shown in Fig. 5.9d, CB agglomerations detected do not extend longer than approximately 30 um. Similar to the bottom surface and cross-section region, the top surface shows a uniform material distribution and good material adhesions without crack neither porosities.

Accordingly, with the conductive capabilities of SMP/CB filament described in section 5.3 and the SEM images of 3D printed specimens on this section, it can be inferred that SMP/CB composites are homogenously distributed.

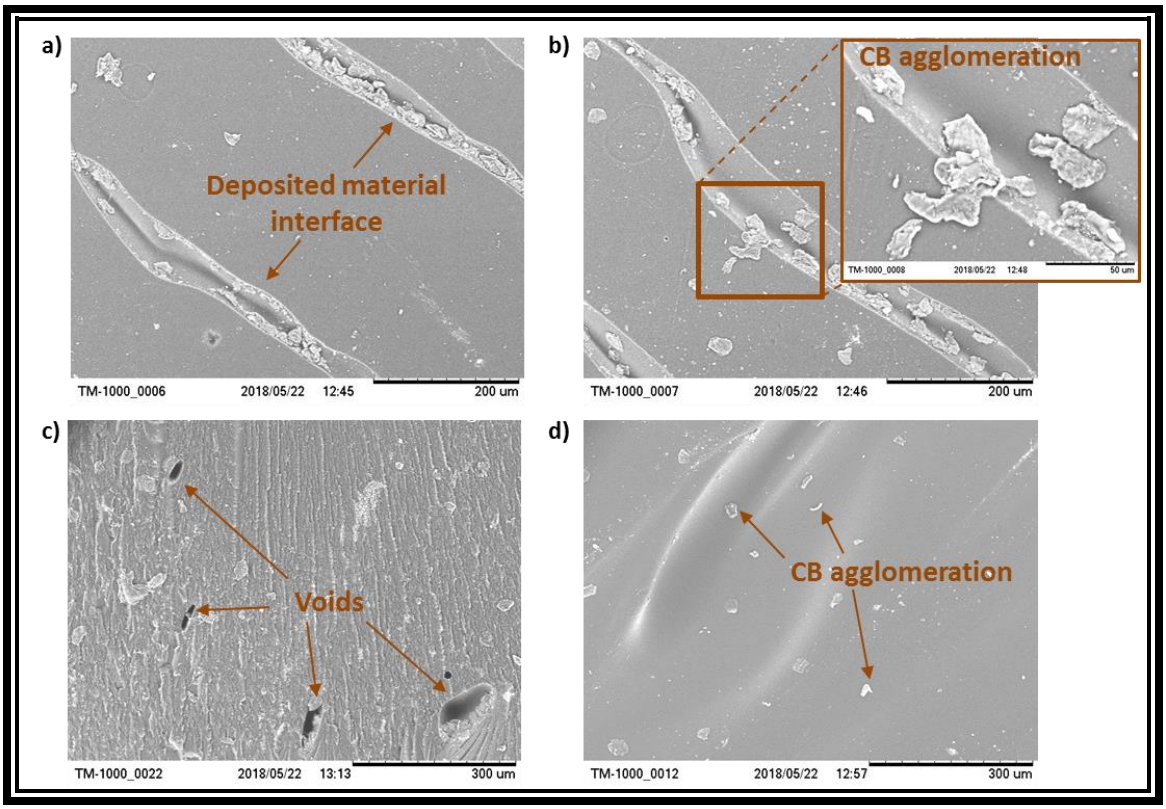

Fig. 5.9: SEM images of SMP/CB 3D printed specimens. a) Bottom surface. b) CB agglomerations on bottom surface. c) Cross-section. d) Top surface.

5.5 Conclusion

This chapter 5 provided a step forward in the integration of SMP/CB nanocomposites with ME-3D printing technique. Conductive SMP/CB nanocomposites fabrication was achieved by solvent casting, filament extrusion, and ME sequential processes. SMP/CB nanocomposites increased their conductivity by increasing of CB wt.% in the SMP matrix. Electrical conductivity was evaluated in the SMP/CB nanocomposites at various concentrations. Further, a direct correlation among temperature increments respect to DC current increments on SMP/CB films (5wt.% CB content) subjected to an electrical stimulus was observed. Moreover, printable

electro-conductive filament for ME was fabricated using a single low-cost extruder. The capability of ME to produce conductive electro-responsive SMP/CB nanocomposites was demonstrated with the fabrication of SMP/CB Dog bone specimens type IV at constant fabrication settings. Finally, SMP/CB nanocomposites stress-elongation testing and toughness evaluation, and SEM analysis were performed. Differences on stress-elongation curves among control specimens and specimens under electrical stimulus were described. Toughness enhancement on specimen under electrical stimulus was 4 times higher compared to controls. In the same basis, elongation was improved from 9.45 to 44%. SEM analysis on SMP/CB indicated a proper material adhesions and material distribution. Finally, this study also provides a reference for future works regarding mechanical properties and guidelines to fabricate SMP/CB conductive systems. In future work, it is required to incorporate design of experiments and optimization technique to find optimal fabrication settings and electrical test conditions to maximize properties of SMP/CB nanocomposites. [3]Research findings of this chapter were reported on literature.

[3] C. A. G. Rosales, M. A. Garcia, H. Kim, L. A. Chavez, D. Hodges, P. Mandal, Y. Lin, and T.-L. B. Tseng, "3D printing of Shape Memory Polymer (SMP)/Carbon Black (CB) nanocomposites with electro-responsive toughness enhancement," Materials Research Express, 2018..

Chapter 6: Photo-thermal Responsive Shape Memory Polymer (SMP)/ Graphene Oxide (GO) Composites Fabricated via Projection-3D Printing Technique

6.1 Introduction

Shape memory polymers (SMPs) and its fabrication process has recently attracted much attention because of their potential application as soft active materials. Demonstration of SMP systems fabricated via 3D printing technologies has been one of the most popular attempts. In this chapter, it is conducted the fabrication of shape memory polymer/graphene oxide (SMP/GO) composites using digital light processing (DLP) 3D printing. According to literature review, GO has high photo-thermal properties, which could be used for SME triggering using a laser beam with specific wavelength. In order to obtain photo-responsive SMP/GO systems fabricated through DLP, it was required to find the proper SMP photo-resin mixing (monomer, cross-linker, photo-initiator) that resulted in high shape memory properties. In this regard, it was possible to obtain a proper mixing ratio to reach thermal recovery ratios of 100% on tested specimens. In addition, mechanical properties of SMP specimens, such as tensile-strength, were characterized and reported in this chapter. It was found that stress-strain curves are consistent among specimens. Experimental trials were conducted to achieve proper GO dispersion in the SMP photo-resin. Moreover, it was investigated the programing capacity of SMP/GO parts using 3-point bending testing. Similar to stress-strain curves, load displacement curves behavior are consistent on 3-point bending test. During experimental trials, it was found that factors such as layer thickness and exposure time significantly vary dimensional characteristics on final parts. Furthermore, since dimensional accuracy is an inherent challenge in 3D printing, an artificial neural network (ANN) was developed using Phyton (Appendix A) based on back propagation theory [87] for modelling dimensional error on specimens fabricated by using DLP process. The ANN input layer consist of DLP process parameters that affects dimensional error on specimens, and a process response (dimensional error) as process output. ANN training and testing phases used historical data and results were compared for several variants of the ANN architecture.

ANN results obtained a maximum Pearson correlation of 77.7 % during testing. This chapter is a reference for fabrication, rheological properties, and dimensional error modelling of SMP/GO composite systems fabricated via DLP 3D printing technique. Next sections are composed as follow. Section 6.2 corresponds to "material and fabrication" with a sub-section that describe the material properties. Section 6.3 pertains to methodology. Section 6.4 corresponds to results and discussion. Lastly, section 6.5 includes conclusion and future work.

6.2 Material and Fabrication

SMP photo-resin was resulting from a mixing of tert-butyl acrylate (tBA) as monomer solvent, di(ethylene glycol) diacrylate (DEGDA) as crosslinker, and Phenylbis (2,4,6-trimethyl-benzoyl) phosphine oxide (BAPO) as photo-initiator, all obtained from Fishier Scientific (USA). The SMP photo-resin has a T_g of 69.5 ºC [14]. This SMP resin was selected because it is suitable for DLP process [14]. Graphene Oxide (GO) nanoflakes (Graphene Oxide, flakes, 15-20 sheets by Aldrich, USA) were chosen as photo-thermal nanofiller due to their high photo-thermal properties over other materials, and its performance shown in previous polymer nanocomposite studies [29, 71, 73]. SMP resin (tBA/ DEGDA/ BAPO) was fabricated in 3 versions to evaluate suitable material combination by varying the DEGDA content (10, 20, 30 wt.%), keeping the BAPO content constant (2 wt.%), and mixing (Vortex Mixer) for 30 min as shown in Table 6.1.

Uniform and continuous SMP/GO nanocomposites with various GO content (1, 2, 3 wt.%) were obtained by blending with SMP resin (fabricated with DEGDA with 20 wt% content). SMP resin and GO were mixed (Vortex Mixer) for 30 min. Homogeneous pure SMP and SMP/GO were poured onto a DLP bath for 3D part fabrication as show in Fig. 6.1. The DLP printer (Wanhao duplicator 7) was selected because of its accessible cost and simple operational procedure. SMP specimens were printed according to ASTM standard D638 (Dog Bone type IV) [84] and SMP/GO specimens according to ASTM D790 (three point bending test specimen) [88] as seen in Fig. 6.2. In Fig. 6.3 is shown the actual fabricated specimens.

Table 6.1: Material content on SMP resin.

Material	Type 1	Type 2	Type 3
Tert-butyl acrylate (tBA) / wt.%	88	78	68
Di(ethylene glycol) diacrylate (DEGDA) / wt.%	10	20	30
Phenylbis (2,4,6-trimethyl-benzoyl) phosphine oxide (BAPO) wt.%	2	2	2

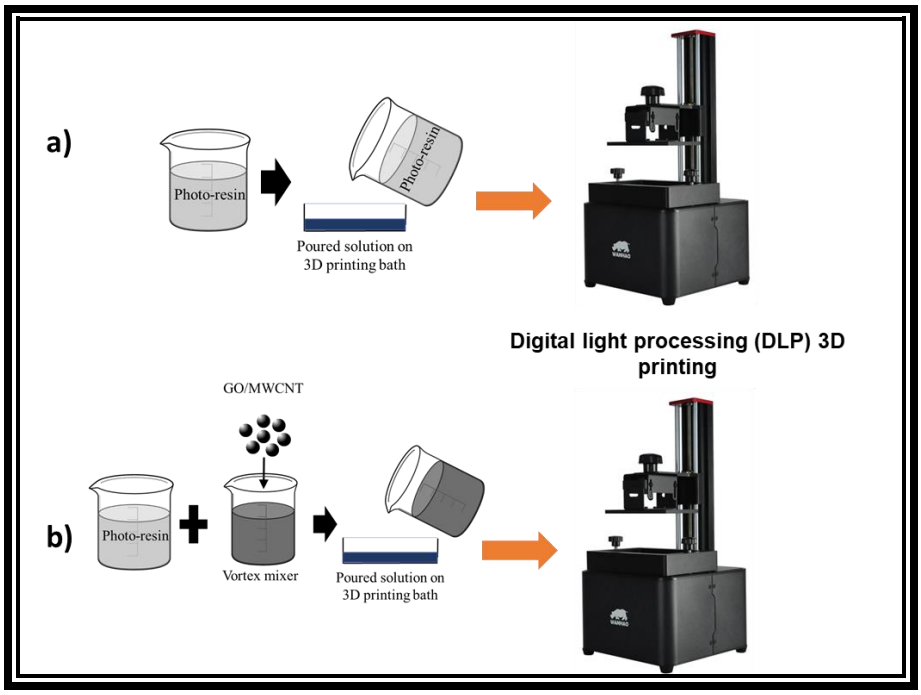

Fig. 6.1: Specimen fabrication process. a) Pure SMP specimens. b) GO/SMP specimens.

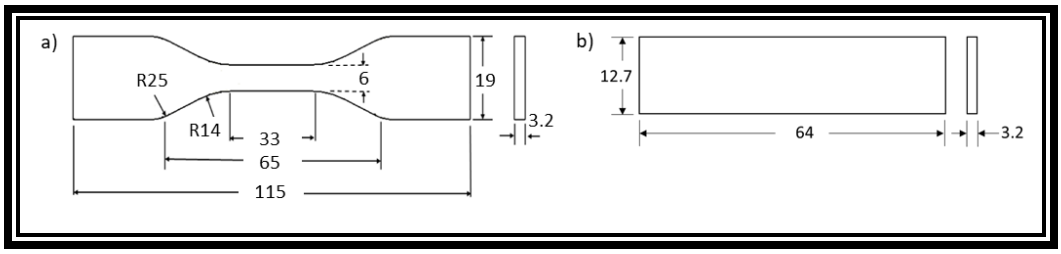

Fig. 6.2: Specimen specification. a) SMP according to ASTM standard D638 (Dog Bone type IV). b) SMP/GO specimens according to ASTM D790 .

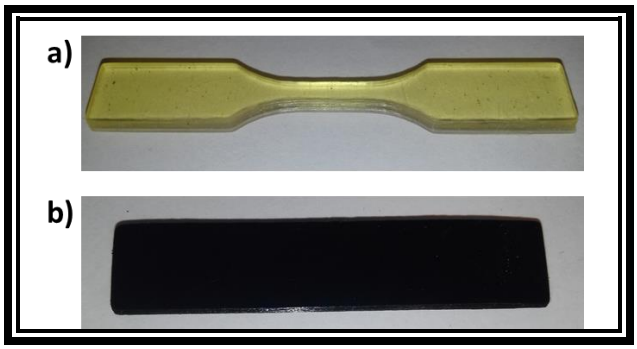

Fig. 6.3: Fabricated specimen. a) SMP specimen. b) SMP/GO specimen.

Prior trial and error fabrication attempts on DLP leaded to process parameters selection. Table 6.2 presents the parameters settings used for specimen fabrication. The specimens were removed from the platform upon completion.

Table 6.2: DLP parameter settings.

Parameter	Value
Slice thickness (mm)	0.020
Exposure Time (ms)	30000
Bottom Exposure (ms)	40000
# of Bottom Layers	2

6.2.1 Material Tensile Property

The tensile property of the SMP material was characterized using dog bone type IV specimens. Five replicas of a Dog Bone type IV were fabricated using DLP process. The tensile test was conducted on an INSTRON 5969 load frame using an extension rate of 5 mm/min, up to a maximum extension of 50 mm, and a holding grip of 25 mm on each end of the 115 mm long dog bone. Tensile strength measurements were carried out at room temperature, which is below the T_g of the SMP material. Stress-elongation curves are presented in next sections.

6.2.1 SMP Recovery Properties

SMP dog bone type IV specimens. Five replicas of a Dog Bone type IV were fabricated using DLP process using pure SMP resins from Table 6.1. SMP properties were evaluated by heating up the specimens in water at 65 ºC for 5 minutes to obtain a sample with uniform distributed temperature. Next, specimens were bended 90 degrees and held until specimens reached the ambient temperature. Finally, the samples were heated up in water to evaluate the recovery capabilities. This programing and recovery evaluation process in presented in Fig. 6.4.

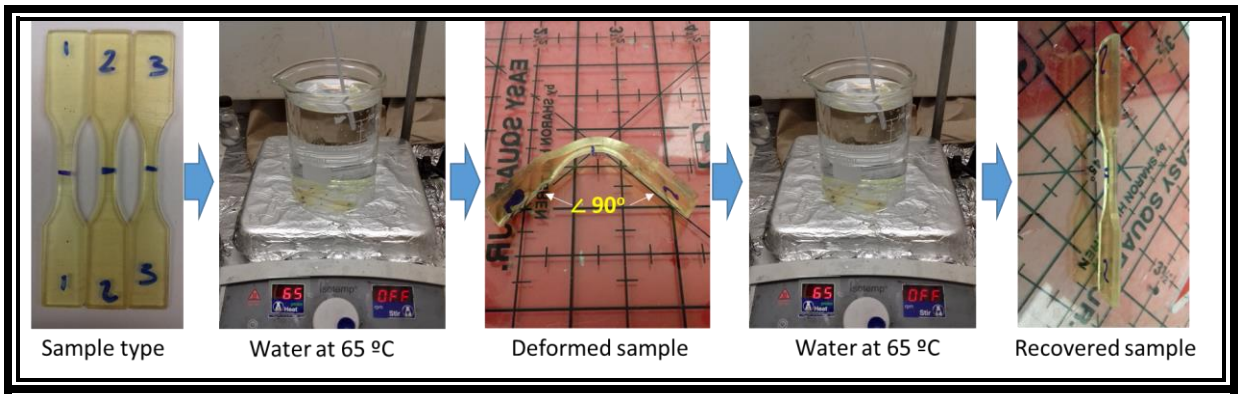

Fig. 6.4: SMP programing and recovery evaluation process.

6.2.1 Three Point Bending Test

The bending property of the GO/SMP material was characterized using ASTM D790 specimens. Five replicas based on ASTM D790 were fabricated using DLP process. The three point bending test was conducted on an INSTRON 5969 load frame using a compression rate of 1 mm/s, up to a maximum extension of 15 mm. Prior, SMP/GO specimens were heated up in water at 65 ºC for 5 minutes and immediately be submitted for testing. Bending measurements were carried out at room temperature, which is below the T_g of the GO/SMP material. Compression data was generated. Fig. 6.5 presents the specimen preparation and three point bending test.

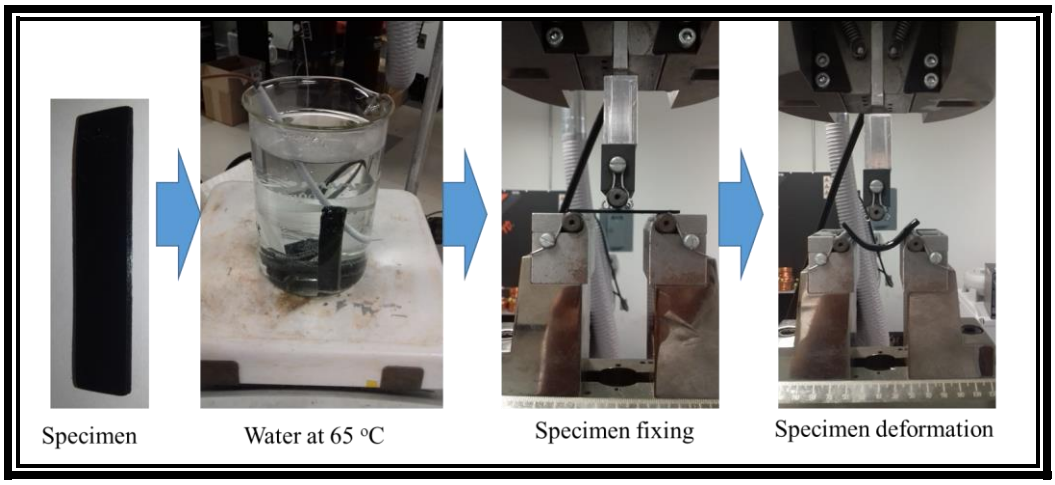

Fig. 6.5: Three point bending evaluation process.

6.3 Proposed Methodology

6.3.1 Artificial Neural Network

Clearly, on Fig. 6.6, it is observed the dimensional variation problem on produced samples using different process parameters. Therefore, ANN modelling designs were implemented using stereolithograply (SL) historical data [89] with 140 data points (111 data samples for training, 29 samples for testing) and evaluated based on cost convergence and Pearson correlation (R) coefficient for dimensional error response. Two neural network designs, ANN (3 inputs, 3 hidden layers/4 neurons each, 1 output) shown in Fig. 6.7, and ANN (3 inputs, 2n+1 neurons, 1 output) as in Fig. 6.8 were defined. The ANN designs used 3 process inputs, layer thickness (displacement of platform on Z axis), curing depth (light penetration during curing), and hatch spacing (distance between projected curing light beams). It was used one process output: dimensional error. For ANN training, it was selected three different amount of epochs (1000, 3000, 5000), and two learning rate (alpha) values (0.01 and 0.001). In addition, it was used Mean Squared Error (MSE) for cost evaluation. The ANN code (presented in Appendix A) was made on Phyton language based on back propagation theory [87] .

Fig. 6.6: Dimensional variation on produced samples using different process parameters.

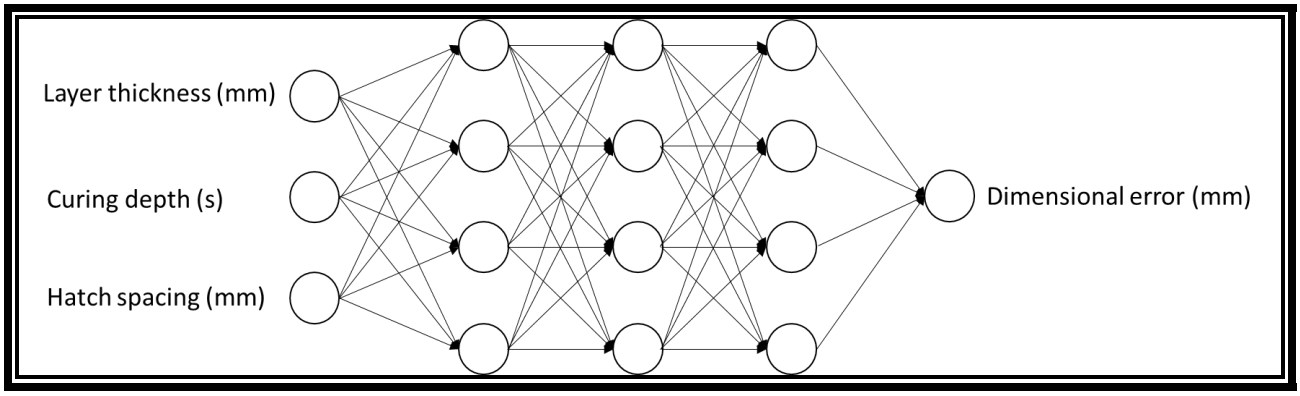

Fig. 6.7: ANN with 3 inputs, 3 hidden layers/ 4 neurons each, 1 output.

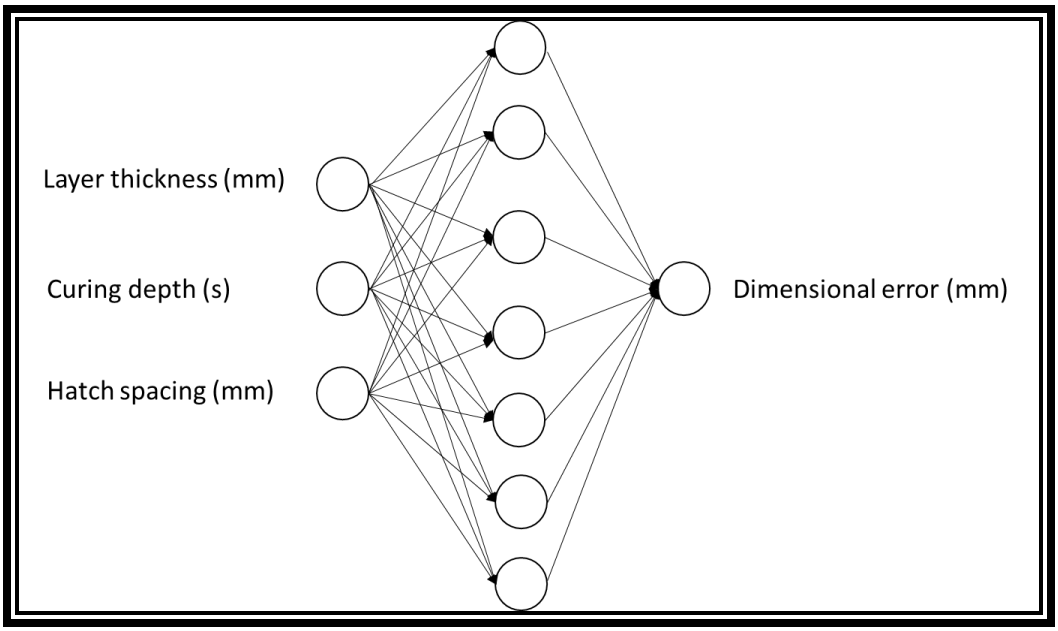

Fig. 6.8: ANN with 3 inputs, 2n+1 neurons, 1 output.

6.4 Results and Discussions

6.4.1 Pure SMP Recovery

Table 6.3 shows the results on programing-recovery testing by bending the specimens 90 degrees as shown in Fig. 6.4, on the three types of mixing contents. Type 2 specimens obtained the desired results by supporting the programming and recovery process successfully. It can be observed on Table 6.4 that failure amount was cero for type 2, while the failure amount for types 3 and 4 was higher. Failure during programing was represented by broken samples, while during recovery stage a failure represents partial recovery. It is infered that failure variation on samples is consequence of different content of crosslinker. Crosslinker provides the "memory capabilities" to the material and the ability to sustain high deformations (super elasticity) by bonding the monomer chains. The cero defects on type 2 SMP proves that the resin is suitable to be programed and recovered at 65 ºC.

Based on the previous results, it was decide to use type 2 SMP resin for further SMP/GO fabrication attempts.

Table 6.3: Pure SMP programing/recovering results.

Programing/recovery test results	Failure amount		Successful amount	
	Bending	Recovering	Bending	Recovering
Type 1	3	1	2	1
Type 2	0	0	5	5
Type 3	2	5	3	0

6.4.2 Stress-Strain Results of Pure SMP Specimens

Fig. 6.9 presents the tensile test results (stress-strain curves) of the 3D printed SMP specimens. The curves are very consistent, especially during the elastic region with a consistent Young's modulus, and maximum stress with values varying from 28 to 33 MPa. Slightly but

stable variation is observed on the plastic region. The elasticity presented by the samples is relevant, strain has an average of 0.3 (mm/mm) which correspond to 3D printing specimens on Fig. 3.7.

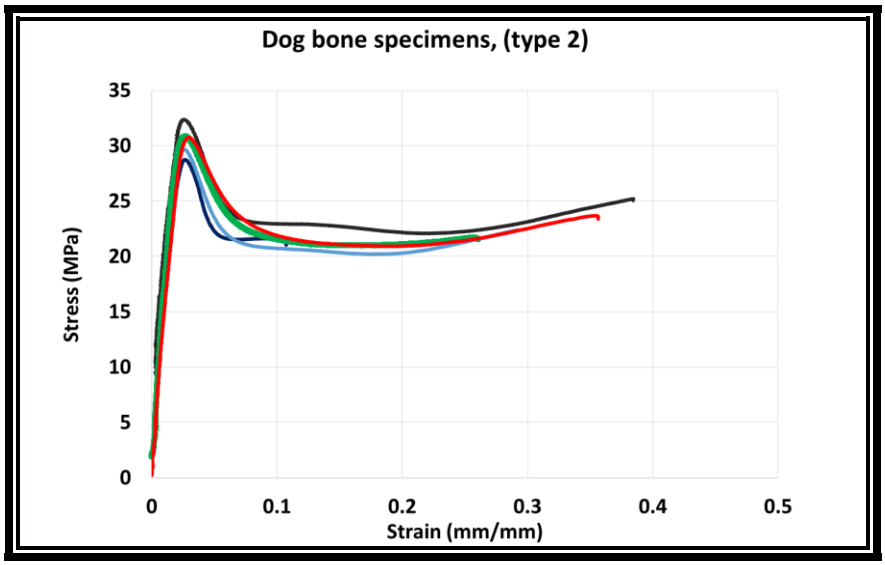

Fig. 6.9: Stress-Strain results of SMP specimens.

6.4.3 Three Point Bending Test

SMP/GO composite was fabricated with 1, 2 and 3 wt. % GO content. After fabrication attempts, 1 wt. % GO content was visually too low in the SMP matrix. SMP/GO specimens with 2 wt. % GO content were successful fabricated with good GO distribution on the matrix. SMP/GO with 3 wt. % GO was not possible to be fabricated on DLP since the high content of GO blocked the curing light. SMP/GO specimens with 2 wt. % content were submitted to three point bending test. The five SMP/GO specimens withheld the deformation without breaking. In Fig. 6.10, it is possible to observe a deformed specimen after three point bending test. In Fig. 6.11, it is presented the load-displacement results. Load displacement curves are stable and consistent among specimens. Specimens reached a maximum deformation of 15 mm and the maximum load founded was around 40 N.

Fig. 6.10: Deformed specimens after three point bending test.

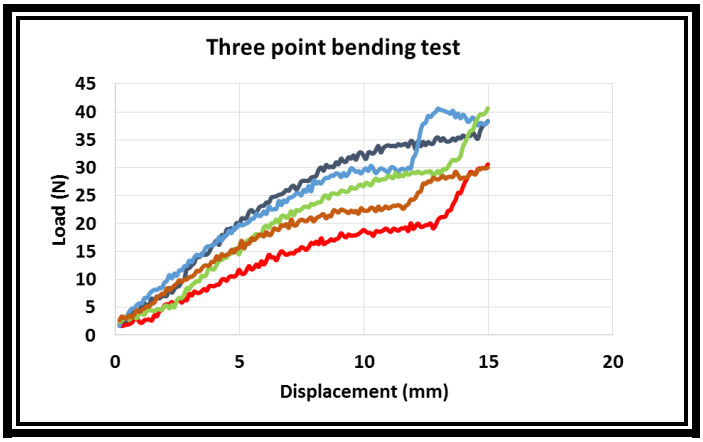

Fig. 6.11: Load-displacement results from three point bending test.

6.4.4 ANN Results

Table 6.5 presents the results of several learning attempts using different amount of epochs (1000, 3000, and 5000) and two learning rate (alpha) values (0.01 and 0.001). It was used 111 data samples for training, and 29 samples for testing. In addition, it was used Mean Squared Error (MSE) to evaluate the model cost. ANN using 2n+1 neuron architecture leaded to obtain the lower cost (0.00049334) and the higher R (0.77635969) value at 5000 epochs and learning rate of .001. See Fig. 6.12 for comparisons on cost and Fig. 6.13 for R-value comparisons among the training variants. It is clearly observed that ANN (2n+1) neuron architecture at 5000 epochs and .001 learning rate obtained the best results. On Fig. 6.14, it is noticed that cost converge to a minimum after 5000 epochs (iterations). This is an indication that after 5000 epochs the model is stable. Moreover, Fig. 6.15 present the correlation dispersion of the target values and predicted values. In addition, Fig. 6.16 and 6.17 present a comparison of target and predicted values of

dimensional error under the fabrication parameters (layer thickness, curing depth, hatch spacing). Future work pertains to validate the results using actual data from SL process.

Table 6.5: MSE and R for dimensional accuracy prediction.

Epoch amount	NN 3X4 hidden neurons		NN 2n+1 hidden neurons	
	Cost	R	Cost	R
1000 Epochs α = 0.01	0.00285819	0.0849229	0.00415647	0.20069911
1000 Epochs α = 0.001	0.07191131	0.51774424	0.0040788	0.27655586
3000 Epochs α = 0.01	0.00068847	0.72605624	0.00065592	0.64353793
3000 Epochs α = 0.001	0.00668608	0.27476683	0.01464068	0.69470278
5000 Epochs α = 0.01	0.0007834	0.57078522	0.00169254	0.45629692
5000 Epochs α = 0.001	0.01598386	0.34577681	**0.00049334**	**0.77635969**

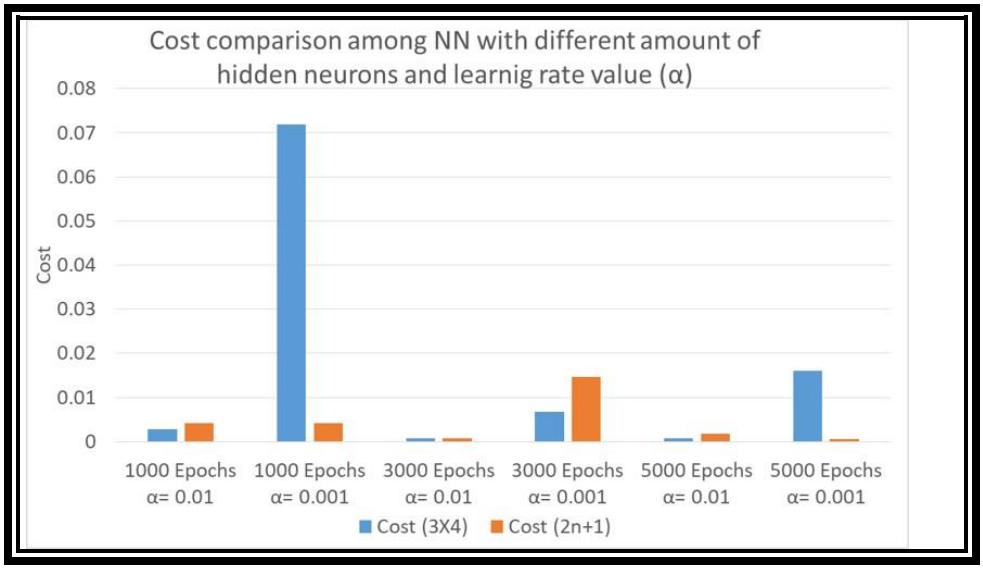

Fig. 6.12: Cost results for various epoch amount and learning rates.

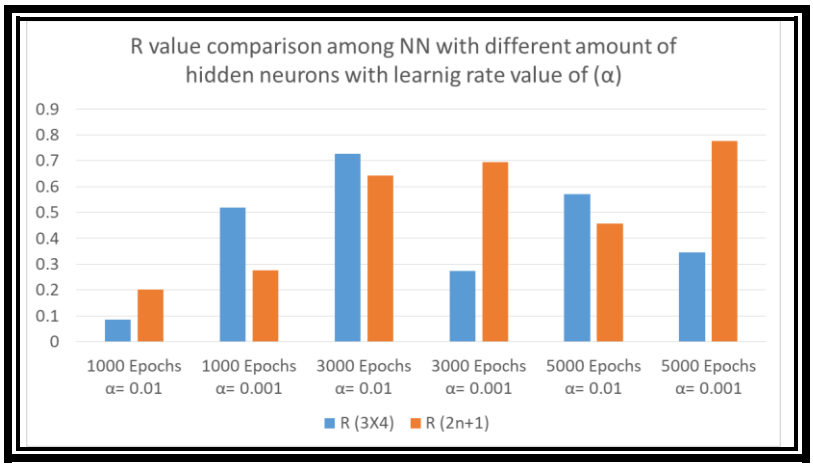

Fig. 6.13: R (correlation value) results for various epoch amount and learning rates.

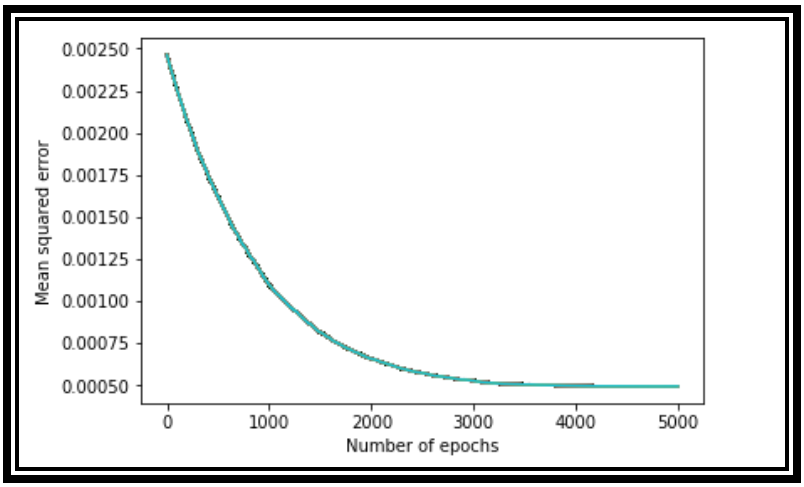

Fig. 6.14: Cost behavior during training of ANN with 2n+1.

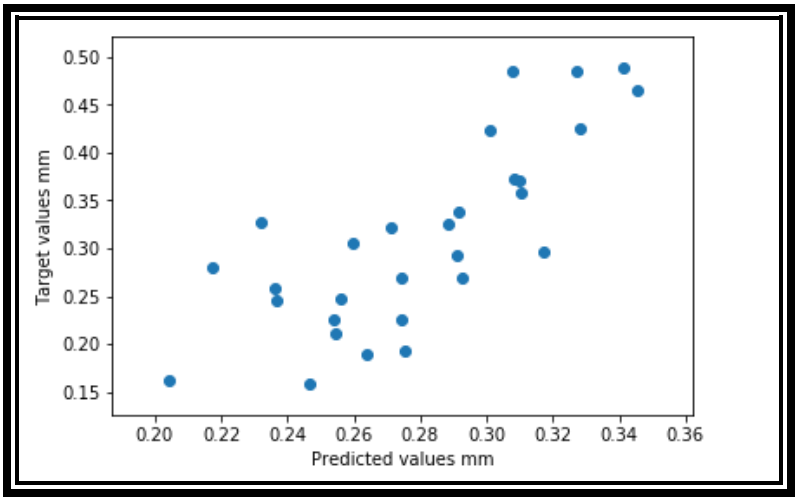

Fig. 6.15: Predicted vs target values during ANN model testing.

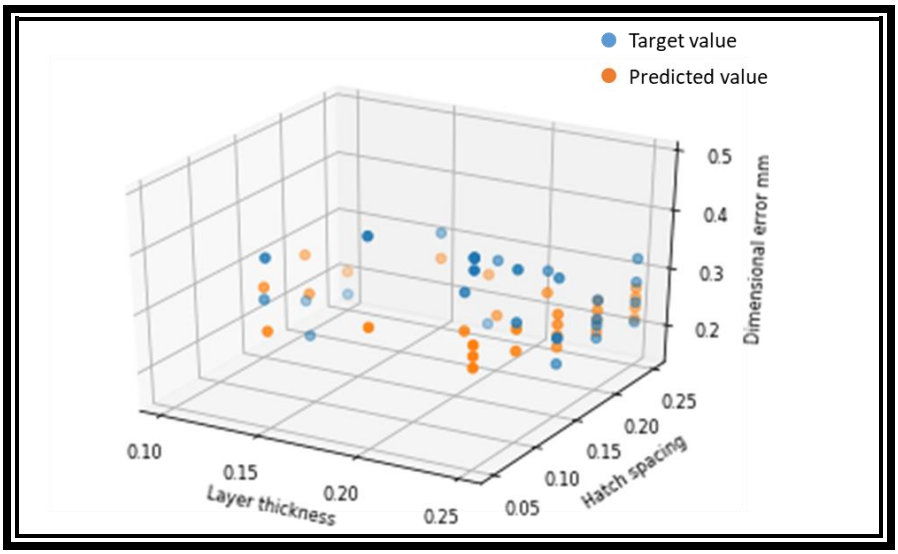

Fig. 6.16: Target and predicted values of dimensional error under layer thickness and hatch spacing parameters.

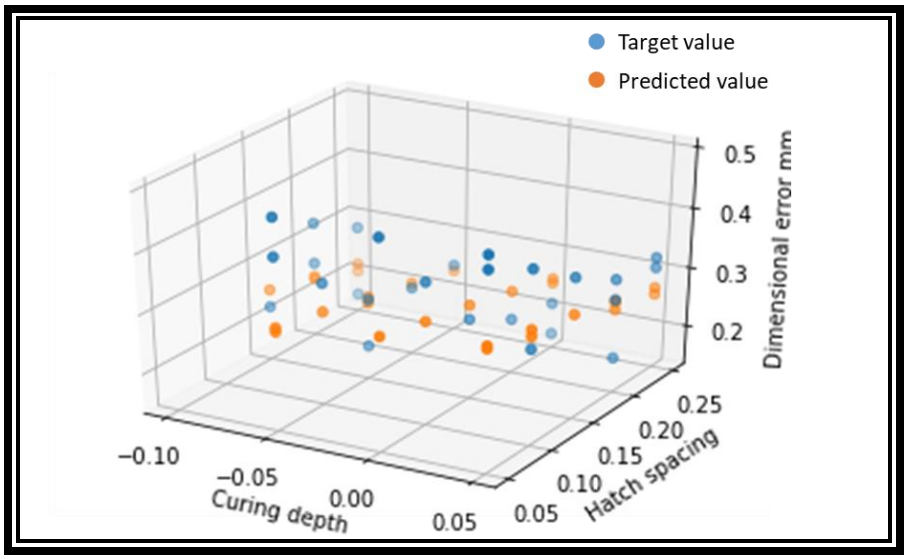

Fig. 6.17: Target and predicted values of dimensional error under curing depth and hatch spacing parameters.

6.5 Conclusion

This chapter 6 demonstrated the capability of produce SMP part on DLP technology. A photo-polymer resin was developed using a monomer, crosslinker, and photo initiator. Later, SMP type 2 was selected based on it good programing and recovery properties shown during 90 degrees specimen bending. Then, SMP dog bone specimens were submitted to tensile test.

Stress-strain results showed low variation among curves. Then, SMP resin type 2 was successfully combined with GO in order to produce SMP/GO. The programing capacities of SMP/GO where tested on a three point bending test that resulted in cero failures and bending consistency among samples. Moreover, the secondary shape was hold, indicating good fixity capabilities. Dimensional variation was detected on SMP/GO due to fabrication settings. Therefore, an ANN modelling technique was suggested in order to predict dimensional error output, a critical characteristic in DLP process. Historical data with 140 data points was used for training and testing of the ANN under different epochs and learning rates. The highest correlation value R was 0.776 under 5000 epochs and 0.001 learning rates. The findings on this chapter are a reference for SMP and GO/SMP fabrication using DLP technology. Moreover, SMP/GO could be used in photo-responsive shape memory systems. Finally, the ANN could be used in future DLP systems to predict the dimensional error based on fabrication settings.

Chapter 7: A Novel Approach for Quality Assessment of 4D Printed Parts

7.1 Introduction

Material extrusion (ME) is a 3D printing technology used for part fabrication by depositing fused polymer layer-by-layer in an additive manner until the part is completed. Recent innovation for polymer filament has led to incorporate materials with special functionalities to ME such as shape memory polymer (SMPs), creating the 4D printing field. An SMP part is capable of recovering its original shape after been deformed, either partially or totally, by applying external thermal stimulus. However, dimensional accuracy of the ME part is a relevant aspect that needs to be further evaluated. The proposed approach focuses on performing dimensional evaluation of printed SMP parts using a 3D scanner. Two algorithms for dimensional evaluation of a ME part and a recovered part are presented. A dimensional accuracy error distribution is obtained by comparing the 3D scan file of a produced part with the actual CAD model. Another dimensional error distribution is acquired through evaluation of a SMP part through digital comparison of 3D scan files of a produced part and a recovered part. A case study is presented through comparison of a commercial SMP substance and a traditional Acrylonitrile Butadiene Styrene (ABS) material. Computational results obtained conclude that SMP and ABS parts have a similar level of dimensional accuracy while the SMP parts have an overall high degree of recovery. This research paves a way to investigate quality assessment in dimensional accuracy for 4D printed parts. Next sections are composed as follow. Section 7.2 corresponds to “material and fabrication” with a sub-section that describe the material properties. Section 7.3 is called “proposed methodology”. Section 7.4 presents a case study and computational results. Lastly, section 7.5 includes conclusion and future work.

7.2 Material and Fabrication

The polymer filaments used in this study are thermo-responsive DiAPLEX MM-4520 SMP [67] and ABS. 3D models of the parts were created using SolidWorks software, and parts fabricated by using an ME printer (Makerbot Replicator 2X). A standard tessellation language

(STL) file was generated from the models and imported to ME software. Makerbot Desktop interface allows to adjust the key process parameters of ME while keeping others fixed. According to previous works, significant process parameters in ME are: nozzle velocity, nozzle temperature, layer height, and platform temperature [22, 33, 67]. Default production settings of ME were used for ABS parts, while for SMP parts, the best settings trials from a previous DOE from chapter 3 were used. Table 7.1 presents the process parameters for ABS parts and SMP parts. The parts were fabricated by depositing extruded material from the nozzle layer by layer following a pre-determined path generated by the ME software. After fabrication, the parts were leaved in place until the temperature reached room temperature and the parts were solidified. In next sections, is presented a description of the ME printer and the 3D scanner followed by the dimensional accuracy evaluation algorithms.

Table 7.1: Process parameter for ABS and SMP parts.

Material	Temperature (ºC)	Travel velocity (mm/s)	Layer Height (mm)	Platform Temperature (ºC)
ABS	230	150	0.20	110
SMP	235	100	0.25	60

The utilized FMD printer was MakerBot Replicator 2X. The maximum build volume for this 3D printer is 24.6 cm x 16.3 cm x 15.5 cm. The ME printer has a head with integrated steep motors that feed the polymer filament into the nozzle. The nozzle heats the filament and deposits it onto a heated surface to build the object layer by layer. Position accuracy of the head in the XY plane is 11 microns and in the Z direction is 2.5 microns, making this ME printer very accurate. The software interface, Makerbot Desktop, operates using a STL file.

Dimensional accuracy inspection was done with a portable 3D scanner (GO!SCAN 20™). It is a self-positioning system that provides visual guidance during scanning. It also provides a fast measurement rate and minimum post-processing work. Also, it can scan small

parts containing a detailed texture with a resolution of up to 0.100 mm. Part of the software that complement the scanner is VXscan for the data acquisition, and VXmodel that is post-treatment software to finalized 3D scan data.

7.3 Proposed Methodology

7.3.1 Dimensional Accuracy Evaluation Algorithms

Fig. 7.1 presents flowchart steps to obtain the dimensional error distribution graphs of ME parts. Fig. 7.1a presents steps for evaluation of a produced part. This procedure applies for dimensional accuracy evaluation of part right after fabrication by making a digital comparison of its dimensional features against a CAD model. Fig. 7.1b provides steps to evaluate a recovered SMP part. This procedure applies for dimensional accuracy evaluation of a recovered part by making a digital comparison of its dimensional features before deformation and after recovery. The next subsections describe the evaluation algorithms.

7.3.1.1 Algorithm for Evaluation of Produced Part

Step 1. Design a CAD model of the part.

Step 2. Generate the STL file: by saving the CAD model as a STL file.

Step 3. Import the file into the 3D printer software.

Step 4. Fabricate the part by using fused deposition modeling (ME) 3D printer.

Step 5. Scan the produced part with the 3D scanner.

Step 6. Post process the scan file by using the 3D scanner software's tools to eliminate the image noise generated. This improve the quality of the scanned file.

Step 7. Generate scan mesh of the scanned files. This steps refers to creating a watertight model of the scan files using the 3D scanner software.

Step 8. Import the CAD model. The 3D scanner software allows to import CAD models (STL file) into the scanner software.

Step 9. Overlap the CAD model and the scan mesh by using the positioning tools of the software.

Step 10. Generate the dimensional error distribution graph. Once the CAD model and the scan mesh have been successfully overlaped it is possible to generate the dimensional error distribution using the proper software tool.

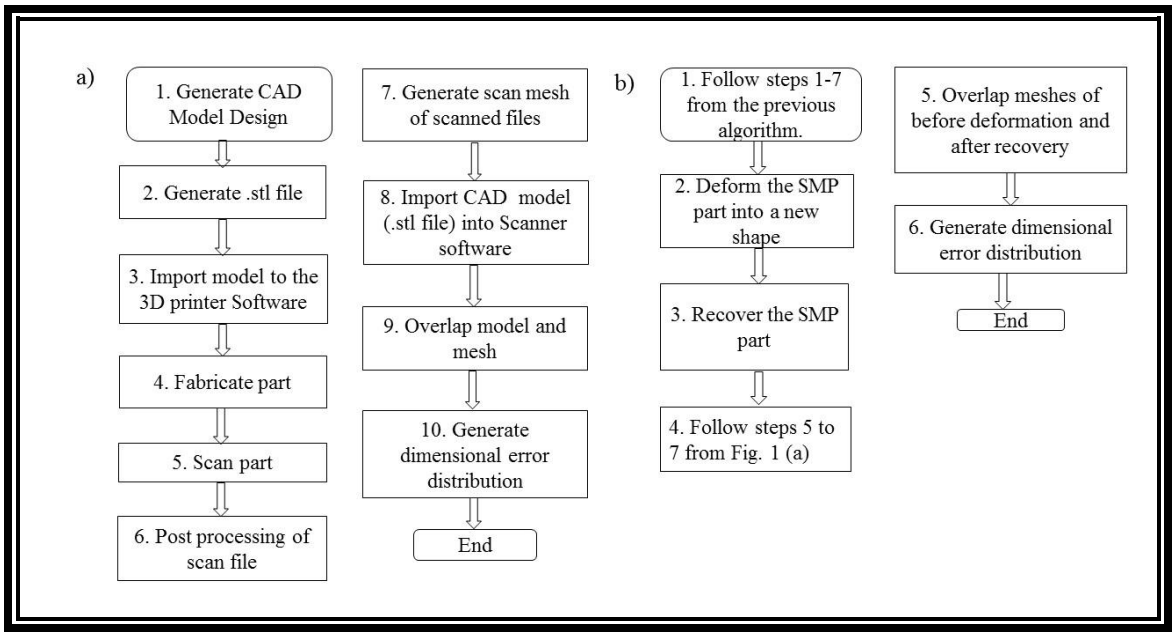

Fig. 7.1: Dimensional accuracy evaluation steps. a) For fabricated parts. b) For recovered parts.

7.3.1.2 Algorithm for Evaluation of Recovered Parts

Step 1. Follow steps 1 to 7 from previous algorithm (Fig. 7.1a).

Step 2. Deform the SMP part by mechanical stress. In this work a compression test was used.

Step 3. Recover the SMP part by using the correct stimulus. In the case study the SMP was heated to 45 ºC for 1 minute.

Step 4. Follow steps 5 to 7 from previous algorithm (Fig. 7.1a) using the recovered part.

Step 5. Overlap scan files to compare meshes of part before deformation and after recovery. By using positioning tools of the software it is possible to overlap both meshes.

Step 6. Generate the dimensional error distribution graph. Once the scan meshes have been successfully overlapped it is possible to generate the deviation error distribution using the proper software tool.

7.4 Case Study and Computational Results

Two parts were selected for a case study evaluation since they are the basis to form other complex designs. Circular shape and L-shape parts were modelled using a CAD software. Fig. 7.2a, c present the model dimensions and Fig. 7.2b, d the actual CAD model. These models were used to fabricate the physical parts using ABS and SMP materials by ME. An evaluation of the dimensional accuracy of the physical parts was performed.

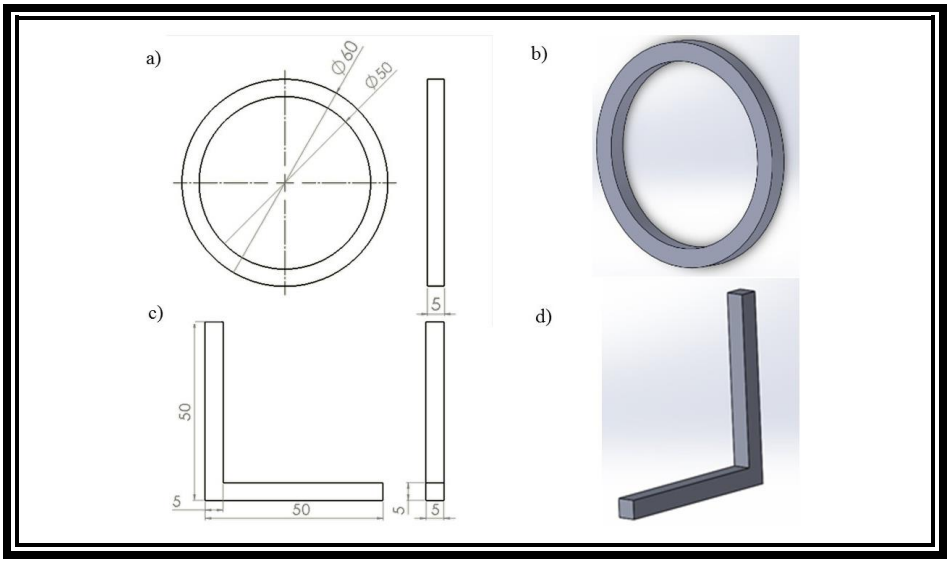

Fig. 7.2: Model dimensions (mm) and CAD models. a-b) Circular shape. C-d) L-shape

7.4.1 Evaluation Results on Produced Parts

The Algorithm from Fig. 7.1a was used to obtain the 3D scans of the physical parts. By using the software tools of the 3D scanner, it was possible to overlap the CAD models and the 3D scans. Fig. 7.3 shows the digital overlapping with a coded color indicating the level of dimensional accuracy error on each region. We used a tolerance of +/-0.2 mm for this study. Green regions are into margin of tolerance. Fig. 7.4a, b shows the actual dimensional error

distribution of SMP parts, indicating that 63.07 % of the sampled points are into tolerance for the circular shape, and 55.66 % for the L- shape. Fig. 7.4c, d shows the dimensional error distribution of ABS parts, indicating that 61.15 % of the sampled region are into tolerance for the circular shape, and 75.70 % for the L-shape..

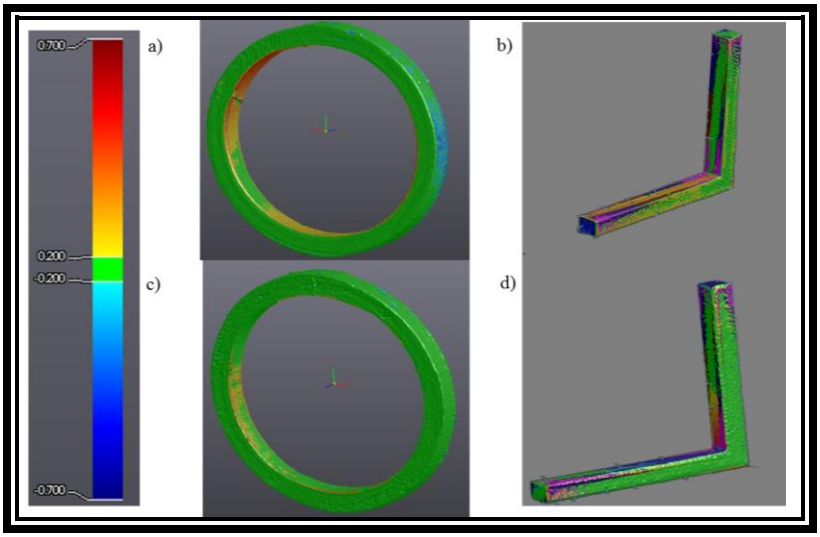

Fig. 7.3: Color-coded comparison between model and 3D scan. a) SMP circular shape. b) SMP L-shape. c) ABS circular shape. d) ABS L-shape.

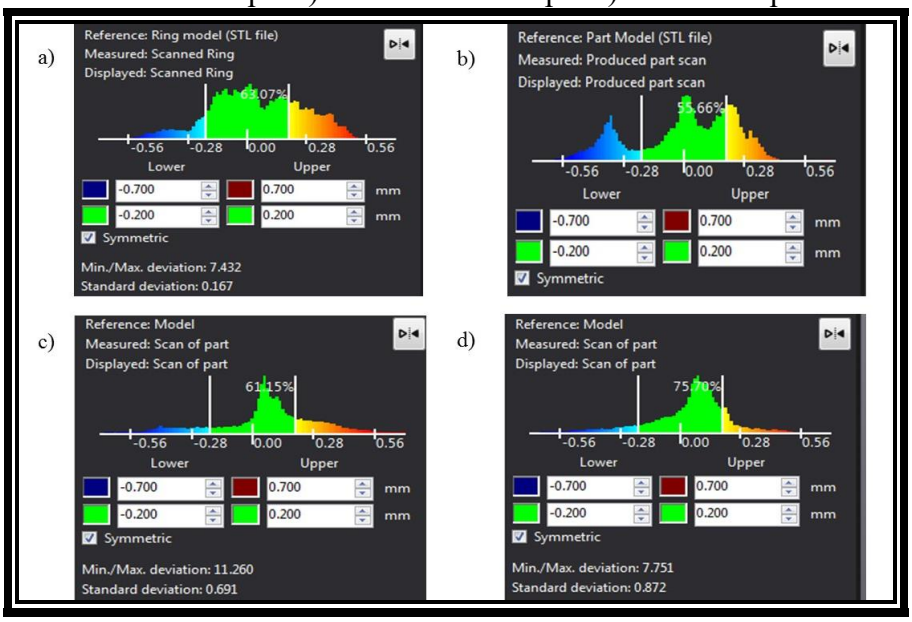

Fig. 7.4: Dimensional error distribution. a) SMP circular shape part. b) SMP L-shape part. c) ABS circular shape part. d) ABS L-shape part.

7.4.2 Evaluation Results on Recovered Parts

Using the 3D scanner, it was also possible to stablish a quality control inspection and quantify the overall recovery percentage for SMP parts; taking into consideration all the features of the recovered part. This was performed using algorithm from Fig. 7.1b. Fig. 7.5 illustrates the dimensional accuracy evaluation process of the circular shape SMP part after recovery. Fig. 7.6 presents the evaluation process of the L-shape SMP part. 3D scan files of the produced parts are shown in Fig. 7.5a and 7.6a. In Fig. 7.5b and 7.6b is possible to observe the level of deformation that suffered the parts. Fig. 7.5c and 7.6c present the 3D scan files of the recovered parts. Finally, a digital comparison between the 3D scan files of the physical parts before deformation and after recovery was performed. Fig. 7.7 presents the dimensional error distribution with a tolerance of +/- 0.2 mm for both parts, acquiring a 69.23% error distribution inside the tolerance for the circular shape and 62.59 % for the L-shape. Table 7.2 summarizes the findings of dimensional accuracy error values into a tolerance of +/-0.2 mm for all the presented cases.

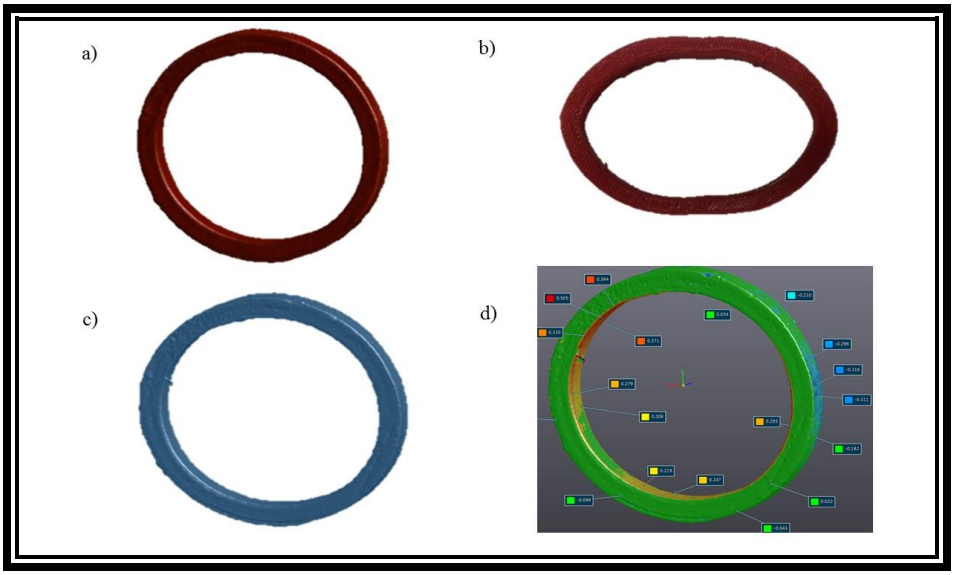

Fig. 7.5: Dimensional accuracy evaluation of the recovered part a) Produced part 3D scan. b) Deformed part. c) Recovered part 3D scan. d) Color-coded comparison of 3D scans.

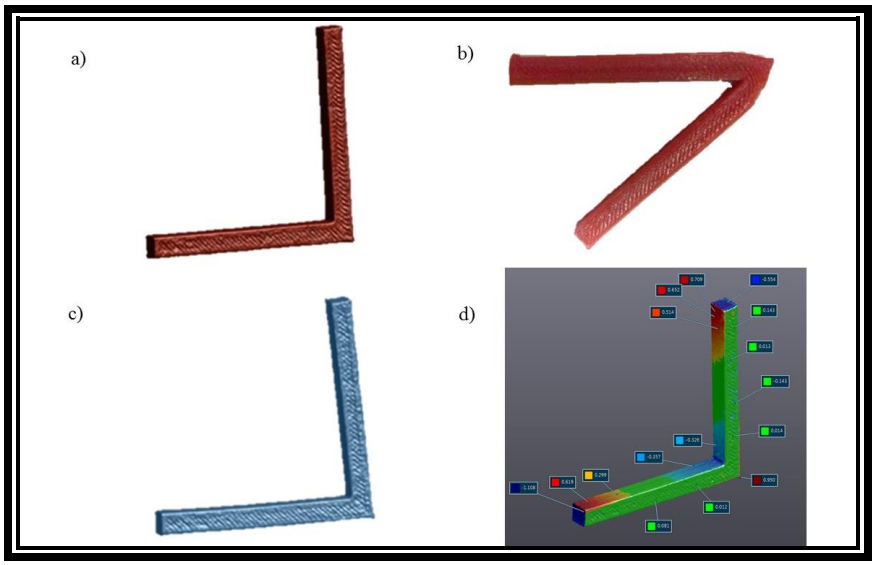

Fig. 7.6: Dimensional accuracy evaluation of the recovered part. a) Produced part 3D scan. b) Deformed part. c) Recovered part 3D scan. d) Color-coded comparison of 3D scans.

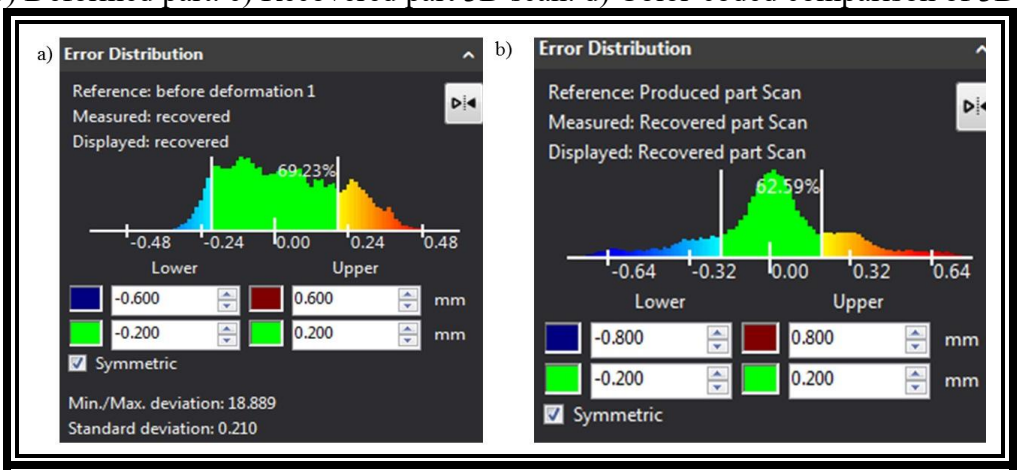

Fig. 7.7: Dimensional accuracy error distribution of recovered parts. a) Circular part. b) L-shape part.

Table 7.2: Dimensional accuracy error into a tolerance of +/-0.2 mm.

Material	Fabricated part		Recovered part	
	Circular shape	L-shape	Circular shape	L-shape
SMP	63.07 %	55.66 %	69.23%	62.59 %
ABS	61.15 %	75.70 %	-----	-----

7.5 Conclusion

This study proposed a novel dimensional accuracy evaluation approach for 4D printed SMP parts. The algorithm generates a dimensional error distribution of the fabricated part from a digital overlapping of a CAD model and a 3D scan file. As well, we presented an algorithm that is useful for recovered SMP parts, which evaluate the dimensional accuracy of recovered SMP parts by comparing 3D scans before deformation and after recovery. Algorithm steps were presented in detail by using a case study and showing the capabilities of the 3D scanner technology. The case study results showed similar dimensional accuracy error values into tolerance for circle shape ME parts made of SMP and ABS. However, the L- shape SMP part showed a significant lower dimensional accuracy error value into tolerance compared with the L-shape ABS part. Furthermore, dimensional error into tolerance was a useful parameter to analyze the level of recovery in SMP parts. Results demonstrated a slightly higher recovery in the circle shape part than in the L-shape part, with a 7% more dimensional error into tolerance. Because of these evaluations, the percentage of error inside the tolerance can be utilized as a single optimization value for future works. Also, it was demonstrated that dimensional accuracy evaluations in 4D printing can be enhanced by integrating 3D scanning tools that increase feature inspection of complex 4D printed parts. Future work include an evaluation of parts with different shapes and a calculation of a recovery index of SMP parts after submitting them to several thermo-mechanical cycles. [4]Research findings of this chapter were reported on literature.

[4]Rosales, C. A. G., (2017). A novel approach for quality assessment of 4D printed parts. International Journal of Industrial Engineering. Manuscript submitted for publication.

Chapter 8: Conclusions and Recommendations for Future Work

Chapter 8 concludes the major contributions of this thesis in fabrication, characterization, and quality assessment of advanced functional polymer systems fabricated by using 3D printing techniques. This chapter also provides recommendations for future work.

8.1 Summary and Conclusion

This dissertation contributed to demonstrate the integration of functional material and 3D printing fabrication technology. Moreover, investigation of process configuration of 3D printers and quality assessments of produced parts using novel algorithms and data analytics were performed. The conclusion of this dissertation is outlined below.

- Chapter 3 provided a step forward in the integration of SMPs parts with ME 3D printing technology. Specimen fabrication using two commercial SMPs was achieved demonstrating the capacity of ME to work with various SMPs. This study also provides a reference for SMP part characterization regarding mechanical properties, recovery ratios and SMP application design. It was demonstrated the capability of integrating SMP materials, DiAPLEX and Tecoflex, with ME using a DOE to obtain fabrication settings and identify main effects. For DiAPLEX, the optimal parameters were a printing velocity of 100 mm/s, a temperature of 235°C and a layer height of 0.25 mm (setting group 8). Where the most influential parameter was printing velocity. For Tecoflex, a printing velocity of 75 mm/s, a temperature of 225°C and a layer height of 0.27 mm were chosen (setting group 2). Where the layer height was the most influential. Stress-strain characterization was performed on the basis of a programing algorithm. It was observed that there was a variation impact in the stress-strain curves and Young's modulus among specimens using different settings. Velocity and layer height are main factors for Young's modulus variation for DiAPLEX and Tecoflex,respectively. Moreover, using a recovery algorithm, a poor long-term fixity property was observed, but this was attributable that the samples were programed at room temperature ($T < Tg$). In addition, recovery ratios were obtained

demonstrating that ME is suitable in producing SMP parts that can achieve a high degree of recovery between 80 and 97 percent depending on the maximum strain programed.

- Chapter 4 demonstrated the capability to fabricate SMP specimens with ME using a DOE. Load displacement curve and recovery efficiency were investigated for various specimens fabricated with different parameter settings. Studied factors were nozzle temperature, nozzle velocity and layer height. Temperature contributed the most to the maximum load reached during the compact tension test. In addition, the raster orientation factor was investigated separately, resulting in a difference between load displacement curves of specimens with a aster orientation of [145,145] and [0,90] degrees. In other test, a slightly higher performance of toughness was obtained in specimens by assisting the recovery process with a clamp compared with specimens without assistance. Toughness values allowed to calculate recovery efficiencies in a way that, to the best of the knowledge of the author, had not been previously considered. Furthermore, it was demonstrated that the SME of Tecoflex SMP can recover a fracture mode I damage up to an efficiency of 4 3percent in a first recovery cycle and up to 23 percent in a second cycle in specimens produced by ME technology. The results in this study could be considered and enhanced in shape memory thermally assisted self-healing works.
- Chapter 5 provided a step forward in the integration of SMP/CB nanocomposites with ME-3Dprinting technique. Conductive SMP/CB nanocomposites fabrication was achieved by solvent casting, filament extrusion, and ME sequential processes. SMP/CB nanocomposites increased their conductivity by increasing of CB wt% in the SMP matrix. Electrical conductivity was evaluated in the SMP/CB nanocomposites at various concentrations. Further, a direct correlation among temperature increments respect to DC current increments on SMP/CB films (5 wt% CB content) subjected to an electrical stimulus was observed. Moreover, printable electro-conductive filament for ME was fabricated using a single low-cost extruder. The capability of ME to produce conductive electro-responsive SMP/CB nanocomposites was demonstrated with the fabrication of SMP/CB Dog bone

specimens type IV at constant fabrication settings. Finally,stress-elongation testing on SMP/CB nanocomposites and toughness evaluation, and SEM analysis were performed. Differences on stress elongation curves among control specimens and specimens under electrical stimulus were described. Toughness enhancement on specimen under electrical stimulus was 4 times higher compared to controls. In the same basis, elongation was improved from 9.45 to 44%. SEM analysis on SMP/CB indicated a proper material adhesions and material distribution. Finally, this study also provides a reference for future works regarding mechanical properties and guidelines to fabricate SMP/CB conductive systems.

- Chapter 6 demonstrated the capability of produce SMP part on SL technology. A photo-polymer resin was developed using a monomer, crosslinker, and photo initiator. Later, SMP type 2 was selected based on its good programing and recovery properties shown during 90 degrees specimen bending. Then, SMP dog bone specimens were submitted to tensile test. Stress-strain results showed low variation among curves. Then, SMP resin type 2 was successfully combined with GO in order to produce SMP/GO. The programing capacities of SMP/GO where tested on a three point bending test that resulted in cero failures and bending consistency among samples. Moreover, the secondary shape was held, indicating good fixity capabilities. Moreover, dimensional variation was detected on SMP/GO due to fabrication settings, during trial and error attempts. Therefore, an ANN modelling technique was suggested in order to predict dimensional error output, a critical characteristic in SL process. Historical data with 140 data points was used for training and testing the ANN under different epochs and learning rates. The highest correlation value R was 0.776 under 5000 epochs and 0.001 learning rates. The findings on this chapter are a reference for SMP and GO/SMP fabrication using SL technology.
- Chapter 7 proposed a novel dimensional accuracy evaluation approach for 4D printed SMP parts. The algorithm generate a dimensional error distribution of the fabricated part from a digital overlapping of a CAD model and a 3D scan file. As well, it was presented an

algorithm that is useful for recovered SMP parts, which evaluate the dimensional accuracy of recovered SMP parts by comparing 3D scans before deformation and after recovery. Algorithm steps were presented in detail by using a case study and showing the capabilities of the 3D scanner technology. The case study results showed similar dimensional accuracy error values into tolerance for circle shape FDM parts made of SMP and ABS. However, the L- shape SMP part showed a significant lower dimensional accuracy error value into tolerance compared with the L-shape ABS part. Furthermore, dimensional error into tolerance was a useful parameter to analyze the level of recovery in SMP parts. Results demonstrated a slightly higher recovery in the circle shape part than in the L-shape part, with a 7% more dimensional error into tolerance. Because of these evaluations, the percentage of error inside the tolerance can be utilized as a single optimization value for future works. Also, it was demonstrated that dimensional accuracy evaluations in 4D printing can be enhanced by integrating 3D scanning tools that increase feature inspection of complex 4D printed parts.

8.2 Recommendations for Future Work

For future work, it could be beneficial to consider an optimization technique that complements the DOE for finding optimal settings and optimal properties. In addition, SMP could be enhanced by adding self-healing polymers to improve and reach higher recovery efficiencies. Moreover, testing of SMP/GO composites by using a laser beam could be performed to evaluate their photo-responsive shape memory systems. Regarding evaluation of dimensional accuracy of SMPs, the developed ANN could be implemented on SL systems to predict the dimensional error based on fabrication settings. Moreover, evaluation of SMP parts with different shapes and a calculation of a recovery index of SMP parts after submitting them to several thermo-mechanical cycles is recommended. Finally, a reliability assessment on possible applications at a test level is a future step.

References

[1] L. Santo, F. Quadrini, A. Accettura, and W. Villadei, "Shape memory composites for self-deployable structures in aerospace applications," *Procedia Engineering,* vol. 88, pp. 42-47, 2014.

[2] C.-C. Kuo, L.-C. Liu, W.-F. Teng, H.-Y. Chang, F.-M. Chien, S.-J. Liao, W.-F. Kuo, and C.-M. Chen, "Preparation of starch/acrylonitrile-butadiene-styrene copolymers (ABS) biomass alloys and their feasible evaluation for 3D printing applications," *Composites Part B: Engineering,* vol. 86, pp. 36-39, 2016.

[3] G. Monkman, "Advances in shape memory polymer actuation," *Mechatronics,* vol. 10, pp. 489-498, 2000.

[4] H. Kim, F. Torres, D. Villagran, C. Stewart, Y. Lin, and T.-L. B. Tseng, "3D Printing of BaTiO3/PVDF Composites with Electric In Situ Poling for Pressure Sensor Applications," *Macromolecular Materials and Engineering,* pp. 1700229-n/a.

[5] C. A. G. Rosales, M. A. Garcia, H. Kim, L. A. Chavez, D. Hodges, P. Mandal, Y. Lin, and T.-L. B. Tseng, "3D printing of Shape Memory Polymer (SMP)/Carbon Black (CB) nanocomposites with electro-responsive toughness enhancement," *Materials Research Express,* 2018.

[6] L. A. Chavez, F. O. Z. Jimenez, B. R. Wilburn, L. C. Delfin, H. Kim, N. Love, and Y. Lin, "Characterization of Thermal Energy Harvesting Using Pyroelectric Ceramics at Elevated Temperatures," *Energy Harvesting and Systems*.

[7] H. Kim, J. Johnson, L. A. Chavez, C. A. G. Rosales, T.-L. B. Tseng, and Y. Lin, "Enhanced dielectric properties of three phase dielectric MWCNTs/BaTiO3/PVDF nanocomposites for energy storage using fused deposition modeling 3D printing," *Ceramics International,* 2018.

[8] H. Kim, T. Fernando, M. Li, Y. Lin, and T.-L. B. Tseng, "Fabrication and characterization of 3D printed BaTiO3/PVDF nanocomposites," *Journal of Composite Materials,* p. 0021998317704709, 2017.

[9] H. Kim, F. Torres, M. T. Islam, M. D. Islam, L. A. Chavez, C. A. Garcia Rosales, B. R. Wilburn, C. M. Stewart, J. C. Noveron, T.-L. B. Tseng, and Y. Lin, "Increased piezoelectric response in functional nanocomposites through multiwall carbon nanotube interface and fused-deposition modeling three-dimensional printing," *MRS Communications,* pp. 1-7, 2017.

[10] H. Kim, F. Torres, Y. Wu, D. Villagran, Y. Lin, and T.-L. B. Tseng, "Integrated 3D printing and corona poling process of PVDF piezoelectric films for pressure sensor application," *Smart Materials and Structures,* 2017.

[11] H. Kim, M. A. I. Shuvo, H. Karim, M. I. Nandasiri, A. M. Schwarz, M. Vijayakumar, J. C. Noveron, T.-l. Tseng, and Y. Lin, "Porous Carbon/CeO2 Nanoparticles Hybrid Material for High-Capacity Super-Capacitors," *MRS Advances,* vol. 2, pp. 2471-2480, 2017.

[12] H. Kim, M. A. I. Shuvo, H. Karim, J. C. Noveron, T.-l. Tseng, and Y. Lin, "Synthesis and characterization of CeO2 nanoparticles on porous carbon for Li-ion battery," *MRS Advances,* vol. 2, pp. 3299-3307, 2017.

[13] Y. Y. C. Choong, M. Saeed, H. Eng, and P.-C. Su, "Curing behaviour and characteristics of shape memory polymers by uv based 3D printing," 2016.

[14] Y. Y. C. Choong, S. Maleksaeedi, H. Eng, J. Wei, and P.-C. Su, "4D printing of high performance shape memory polymer using stereolithography," *Materials & Design,* vol. 126, pp. 219-225, 2017.

[15] Y. Y. C. Choong, S. Maleksaeedi, H. Eng, P.-C. Su, and J. Wei, "Curing characteristics of shape memory polymers in 3D projection and laser stereolithography," *Virtual and Physical Prototyping,* vol. 12, pp. 77-84, 2017.

[16] S. Tibbits, "4D printing: multi-material shape change," *Architectural Design,* vol. 84, pp. 116-121, 2014.

[17] A. Lendlein and S. Kelch, "Shape-memory polymers," *Angewandte Chemie International Edition,* vol. 41, pp. 2034-2057, 2002.

[18] Z. X. Khoo, J. E. M. Teoh, Y. Liu, C. K. Chua, S. Yang, J. An, K. F. Leong, and W. Y. Yeong, "3D printing of smart materials: A review on recent progresses in 4D printing," *Virtual and Physical Prototyping,* vol. 10, pp. 103-122, 2015.

[19] W. Xu, H. Yang, W. Zeng, T. Houghton, X. Wang, R. Murthy, H. Kim, Y. Lin, M. Mignolet, H. Duan, H. Yu, M. Slepian, and H. Jiang, "Food-Based Edible and Nutritive Electronics," *Advanced Materials Technologies,* pp. 1700181-n/a.

[20] C. Schmidt, A. S. Chowdhury, K. Neuking, and G. Eggeler, "Studies on the cycling, processing and programming of an industrially applicable shape memory polymer Tecoflex®(or TFX EG 72D)," *High Performance Polymers,* vol. 23, pp. 300-307, 2011.

[21] C. Liu, H. Qin, and P. Mather, "Review of progress in shape-memory polymers," *Journal of Materials Chemistry,* vol. 17, pp. 1543-1558, 2007.

[22] X. Wu, W. Huang, and H. Tan, "Characterization of shape recovery via creeping and shape memory effect in ether-vinyl acetate copolymer (EVA)," *Journal of Polymer Research,* vol. 20, p. 150, 2013.

[23] H. Tobushi, S. Hayashi, K. Hoshio, and Y. Ejiri, "Shape recovery and irrecoverable strain control in polyurethane shape-memory polymer," *Science and Technology of Advanced Materials,* vol. 9, p. 015009, 2008.

[24] S. Reddy, E. Arzt, and A. del Campo, "Bioinspired surfaces with switchable adhesion," *Advanced Materials,* vol. 19, pp. 3833-3837, 2007.

[25] R. Kazakevičiūtė-Makovska, A. Özlem Özarmut, and H. Steeb, "Characterization of shape memory polymer estane by means of dynamic mechanical thermal analysis technique," *Smart Materials Research,* vol. 2014, 2014.

[26] Y. Heo and H. A. Sodano, "Self-Healing Polyurethanes with Shape Recovery," *Advanced Functional Materials,* vol. 24, pp. 5261-5268, 2014.

[27] X. Wang, J. Zhao, M. Chen, L. Ma, X. Zhao, Z.-M. Dang, and Z. Wang, "Improved self-healing of polyethylene/carbon black nanocomposites by their shape memory effect," *The Journal of Physical Chemistry B,* vol. 117, pp. 1467-1474, 2013.

[28] A. Lalisse, G. Tessier, J. Plain, and G. Baffou, "Quantifying the efficiency of plasmonic materials for near-field enhancement and photothermal conversion," *The Journal of Physical Chemistry C,* vol. 119, pp. 25518-25528, 2015.

[29] A. F. Zedan, S. Moussa, J. Terner, G. Atkinson, and M. S. El-Shall, "Ultrasmall gold nanoparticles anchored to graphene and enhanced photothermal effects by laser irradiation of gold nanostructures in graphene oxide solutions," *ACS nano,* vol. 7, pp. 627-636, 2012.

[30] I. H. El-Sayed, X. Huang, and M. A. El-Sayed, "Selective laser photo-thermal therapy of epithelial carcinoma using anti-EGFR antibody conjugated gold nanoparticles," *Cancer letters,* vol. 239, pp. 129-135, 2006.

[31] M. E. Garcia, Y. Lin, and H. A. Sodano, "Autonomous materials with controlled toughening and healing," *Journal of Applied Physics,* vol. 108, p. 093512, 2010.

[32] Y. Yang, Y. Chen, Y. Wei, and Y. Li, "3D printing of shape memory polymer for functional part fabrication," *The International Journal of Advanced Manufacturing Technology,* vol. 84, pp. 2079-2095, 2016.

[33] M. Zarek, M. Layani, I. Cooperstein, E. Sachyani, D. Cohn, and S. Magdassi, "3D printing of shape memory polymers for flexible electronic devices," *Advanced Materials,* vol. 28, pp. 4449-4454, 2016.

[34] K. Yu, A. Ritchie, Y. Mao, M. L. Dunn, and H. J. Qi, "Controlled sequential shape changing components by 3D printing of shape memory polymer multimaterials," *Procedia Iutam,* vol. 12, pp. 193-203, 2015.

[35] H. Li, X. Gao, and Y. Luo, "Multi-shape memory polymers achieved by the spatio-assembly of 3D printable thermoplastic building blocks," *Soft matter,* vol. 12, pp. 3226-3233, 2016.

[36] F. Senatov, K. Niaza, M. Y. Zadorozhnyy, A. Maksimkin, S. Kaloshkin, and Y. Estrin, "Mechanical properties and shape memory effect of 3D-printed PLA-based porous scaffolds," *Journal of the mechanical behavior of biomedical materials,* vol. 57, pp. 139-148, 2016.

[37] O. A. Mohamed, S. H. Masood, and J. L. Bhowmik, "Optimization of fused deposition modeling process parameters: a review of current research and future prospects," *Advances in Manufacturing,* vol. 3, pp. 42-53, 2015.

[38] T.-L. B. Tseng, A. Chilukuri, S. C. Park, and Y. J. Kwon, "Automated quality characterization of 3D printed bone scaffolds," *Journal of Computational Design and Engineering,* vol. 1, pp. 194-201, 2014.

[39] T.-L. B. Tseng, C. A. Garcia Rosales, and Y. J. Kwon, "OPTIMIZATION OF WIND TURBINE PLACEMENT LAYOUT ON NON-FLAT TERRAINS," *International Journal of Industrial Engineering,* vol. 21, 2014.

[40] F. Rayegani and G. Onwubolu, "Fused deposition modelling (FDM) process parameter prediction and optimization using group method for data handling (GMDH) and differential evolution (DE)," *International Journal of Advanced Manufacturing Technology,* vol. 73, 2014.

[41] T. Nancharaiah, V. R. d Ranga Raju, and R. Raju, "An experimental investigation on surface quality and dimensional accuracy of FDM components," 2010.

[42] A. K. Sood, R. Ohdar, and S. S. Mahapatra, "Improving dimensional accuracy of fused deposition modelling processed part using grey Taguchi method," *Materials & Design,* vol. 30, pp. 4243-4252, 2009.

[43] R. Pennington, N. Hoekstra, and J. Newcomer, "Significant factors in the dimensional accuracy of fused deposition modelling," *Proceedings of the Institution of Mechanical Engineers, Part E: Journal of Process Mechanical Engineering,* vol. 219, pp. 89-92, 2005.

[44] A. Garg, A. Bhattacharya, and A. Batish, "On surface finish and dimensional accuracy of FDM parts after cold vapor treatment," *Materials and Manufacturing Processes,* vol. 31, pp. 522-529, 2016.

[45] H. Zhang and Y. Zhao, "Polymers with dual light-triggered functions of shape memory and healing using gold nanoparticles," *ACS applied materials & interfaces,* vol. 5, pp. 13069-13075, 2013.

[46] X. Wu, W. Huang, Z. Seow, W. Chin, W. Yang, and K. Sun, "Two-step shape recovery in heating-responsive shape memory polytetrafluoroethylene and its thermally assisted self-healing," *Smart Materials and Structures,* vol. 22, p. 125023, 2013.

[47] K. Wang, G. Zhu, F. Ren, X. Yan, and X. Cui, "The effects of carbon fiber on electroactive shape memory behaviors of cyanate/polybutadiene epoxy/carbon black composites," *Journal of Reinforced Plastics and Composites,* vol. 35, pp. 556-565, 2016.

[48] D. Habault, H. Zhang, and Y. Zhao, "Light-triggered self-healing and shape-memory polymers," *Chemical Society Reviews,* vol. 42, pp. 7244-7256, 2013.

[49] X. Luo and P. T. Mather, "Shape memory assisted self-healing coating," *ACS Macro Letters,* vol. 2, pp. 152-156, 2013.

[50] J. Jordan, K. I. Jacob, R. Tannenbaum, M. A. Sharaf, and I. Jasiuk, "Experimental trends in polymer nanocomposites—a review," *Materials science and engineering: A,* vol. 393, pp. 1-11, 2005.

[51] A. Benchirouf, S. Palaniyappan, R. Ramalingame, P. Raghunandan, T. Jagemann, C. Müller, M. Hietschold, and O. Kanoun, "Electrical properties of multi-walled carbon nanotubes/PEDOT: PSS nanocomposites thin films under temperature and humidity effects," *Sensors and Actuators B: Chemical,* vol. 224, pp. 344-350, 2016.

[52] T. Xie, H. Zhang, Y. Lin, Y. Xu, Y. Ruan, W. Weng, and H. Xia, "A simple and versatile approach to self-healing polymers and electrically conductive composites," *RSC Advances,* vol. 5, pp. 13261-13269, 2015.

[53] B. Marinho, M. Ghislandi, E. Tkalya, C. E. Koning, and G. de With, "Electrical conductivity of compacts of graphene, multi-wall carbon nanotubes, carbon black, and graphite powder," *Powder technology,* vol. 221, pp. 351-358, 2012.

[54] X. Luo and P. T. Mather, "Conductive shape memory nanocomposites for high speed electrical actuation," *Soft Matter,* vol. 6, pp. 2146-2149, 2010.

[55] R. Abishera, R. Velmurugan, and K. N. Gopal, "Reversible plasticity shape memory effect in carbon nanotubes reinforced epoxy nanocomposites," *Composites Science and Technology,* vol. 137, pp. 148-158, 2016.

[56] X. Qi, H. Xiu, Y. Wei, Y. Zhou, Y. Guo, R. Huang, H. Bai, and Q. Fu, "Enhanced shape memory property of polylactide/thermoplastic poly (ether) urethane composites via carbon black self-networking induced co-continuous structure," *Composites Science and Technology,* vol. 139, pp. 8-16, 2017.

[57] L.-C. Tang, Y.-J. Wan, K. Peng, Y.-B. Pei, L.-B. Wu, L.-M. Chen, L.-J. Shu, J.-X. Jiang, and G.-Q. Lai, "Fracture toughness and electrical conductivity of epoxy composites filled with carbon nanotubes and spherical particles," *Composites Part A: Applied Science and Manufacturing,* vol. 45, pp. 95-101, 2013.

[58] S. W. Kwok, K. H. H. Goh, Z. D. Tan, S. T. M. Tan, W. W. Tjiu, J. Y. Soh, Z. J. G. Ng, Y. Z. Chan, H. K. Hui, and K. E. J. Goh, "Electrically conductive filament for 3D-printed circuits and sensors," *Applied Materials Today,* vol. 9, pp. 167-175, 2017.

[59] M. Al-Rubaiai, T. Pinto, D. Torres, N. Sepulveda, and X. Tan, "Characterization of a 3D-Printed Conductive PLA Material With Electrically Controlled Stiffness," in *ASME 2017 Conference on Smart Materials, Adaptive Structures and Intelligent Systems*, 2017, pp. V001T01A003-V001T01A003.

[60] N. Rogers and F. Khan, "Characterization of deformation induced changes to conductivity in an electrically triggered shape memory polymer," *Polymer Testing,* vol. 32, pp. 71-77, 2013.

[61] W. Liu, N. Wu, and K. Pochiraju, "Relationship Between Conductivities and Shape Memory Performance of FDM Composite Filaments," in *ASME 2017 International Mechanical Engineering Congress and Exposition*, 2017, pp. V014T11A002-V014T11A002.

[62] H. Lu, Y. Yao, and L. Lin, "Carbon-based reinforcement in shape-memory polymer composite for electrical actuation," *Pigment & Resin Technology,* vol. 43, pp. 26-34, 2013.

[63] Y. Wang, G. Zhu, X. Cui, T. Liu, Z. Liu, and K. Wang, "Electroactive shape memory effect of radiation cross-linked SBS/LLDPE composites filled with carbon black," *Colloid and Polymer Science,* vol. 292, pp. 2311-2317, 2014.

[64] X. Wang, J. Sparkman, and J. Gou, "Electrical actuation and shape memory behavior of polyurethane composites incorporated with printed carbon nanotube layers," *Composites Science and Technology,* vol. 141, pp. 8-15, 2017.

[65] H. Lu, F. Liang, Y. Yao, J. Gou, and D. Hui, "Self-assembled multi-layered carbon nanofiber nanopaper for significantly improving electrical actuation of shape memory polymer nanocomposite," *Composites Part B: Engineering,* vol. 59, pp. 191-195, 2014.

[66] M. Raja, S. H. Ryu, and A. Shanmugharaj, "Thermal, mechanical and electroactive shape memory properties of polyurethane (PU)/poly (lactic acid)(PLA)/CNT nanocomposites," *European Polymer Journal,* vol. 49, pp. 3492-3500, 2013.

[67] H. Yang, W. R. Leow, T. Wang, J. Wang, J. Yu, K. He, D. Qi, C. Wan, and X. Chen, "3D printed photoresponsive devices based on shape memory composites," *Advanced Materials,* vol. 29, p. 1701627, 2017.

[68] J. Liang, Y. Xu, Y. Huang, L. Zhang, Y. Wang, Y. Ma, F. Li, T. Guo, and Y. Chen, "Infrared-triggered actuators from graphene-based nanocomposites," *The Journal of Physical Chemistry C,* vol. 113, pp. 9921-9927, 2009.

[69] R. R. Kohlmeyer, M. Lor, and J. Chen, "Remote, local, and chemical programming of healable multishape memory polymer nanocomposites," *Nano letters,* vol. 12, pp. 2757-2762, 2012.

[70] J. Leng, X. Wu, and Y. Liu, "Infrared light-active shape memory polymer filled with nanocarbon particles," *Journal of Applied Polymer Science,* vol. 114, pp. 2455-2460, 2009.

[71] L. Yu and H. Yu, "Light-powered tumbler movement of graphene oxide/polymer nanocomposites," *ACS applied materials & interfaces,* vol. 7, pp. 3834-3839, 2015.

[72] F. Liang, R. Sivilli, J. Gou, Y. Xu, and B. Mabbott, "Electrical actuation and shape recovery control of shape-memory polymer nanocomposites," *International Journal of Smart and Nano Materials,* vol. 4, pp. 167-178, 2013.

[73] M. Yoonessi, Y. Shi, D. A. Scheiman, M. Lebron-Colon, D. M. Tigelaar, R. Weiss, and M. A. Meador, "Graphene polyimide nanocomposites; thermal, mechanical, and high-temperature shape memory effects," *ACS nano,* vol. 6, pp. 7644-7655, 2012.

[74] A. Noriega, D. Blanco, B. Alvarez, and A. Garcia, "Dimensional accuracy improvement of FDM square cross-section parts using artificial neural networks and an optimization algorithm," *The International Journal of Advanced Manufacturing Technology,* vol. 69, pp. 2301-2313, 2013.

[75] D. A. Schaub, K.-R. Chu, and D. C. Montgomery, "Optimizing stereolithography throughput," *Journal of Manufacturing Systems,* vol. 16, p. 290, 1997.

[76] P.-T. Lan, S.-Y. Chou, L.-L. Chen, and D. Gemmill, "Determining fabrication orientations for rapid prototyping with stereolithography apparatus," *Computer-Aided Design,* vol. 29, pp. 53-62, 1997.

[77] T. H. Pang, M. D. Guertin, and H. D. Nguyen, "Accuracy of Stereolithography Parts: Mechanism and Modes of Distortion for a" Letter H" Diagnostic Part," in *Proceedings of the Solid Free Form Fabrication Symposium*, 1995, pp. 170-180.

[78] S. Onuh and K. Hon, "Optimising build parameters for improved surface finish in stereolithography," *International Journal of Machine Tools and Manufacture,* vol. 38, pp. 329-342, 1998.

[79] C. Lynn-Charney and D. W. Rosen, "Usage of accuracy models in stereolithography process planning," *Rapid Prototyping Journal,* vol. 6, pp. 77-87, 2000.

[80] D. Karalekas and A. Aggelopoulos, "Study of shrinkage strains in a stereolithography cured acrylic photopolymer resin," *Journal of Materials Processing Technology,* vol. 136, pp. 146-150, 2003.

[81] J. G. Zhou, D. Herscovici, and C. C. Chen, "Parametric process optimization to improve the accuracy of rapid prototyped stereolithography parts," *International Journal of Machine Tools and Manufacture,* vol. 40, pp. 363-379, 2000.

[82] H. Cho, W. Park, B. Choi, and M.-C. Leu, "Determining optimal parameters for sterolithography processes via genetic algorithm," *Journal of Manufacturing Systems,* vol. 19, p. 18, 2000.

[83] P. E. Reeves and R. C. Cobb, "Reducing the surface deviation of stereolithography using in-process techniques," *Rapid Prototyping Journal,* vol. 3, pp. 20-31, 1997.

[84] A. Standard, "Standard test method for tensile properties of plastics," *ASTM International. Designation: D,* vol. 638, pp. 1-13, 2003.

[85] D. H. N. S. Ravi Patel, Prof. Susheela V. Kumari, "Experimental Investigation of Fracture of ABS Material by ASTM D-5045 for Different Crack Length & Layer of Orientation Using FDM Process," *International Journal of Mechanical and Industrial Technology,* vol. 3, pp. 79-83, 2015.

[86] C. A. G. Rosales, C.-C. Huang, and Y. Lin, "Characterization and Quality Assessment of Shape Memory Polymer Parts Fabricated Using Fused Deposition Modelling," in *IIE Annual Conference. Proceedings*, 2017, pp. 1270-1275.

[87] R. Hecht-Nielsen, "Theory of the backpropagation neural network," in *Neural networks for perception*, ed: Elsevier, 1992, pp. 65-93.

[88] A. International, "ASTM D790-17 Standard Test Methods for Flexural Properties of Unreinforced and Reinforced Plastics and Electrical Insulating Materials," ed, 2017.

[89] S. Lee, W. Park, H. Cho, W. Zhang, and M.-C. Leu, "A neural network approach to the modelling and analysis of stereolithography processes," *Proceedings of the Institution of Mechanical Engineers, Part B: Journal of Engineering Manufacture,* vol. 215, pp. 1719-1733, 2001.

Appendix A

Neural Network Code (Phyton)

File Edit View Insert Cell Kernel Widgets Help

Run Code

In [ ]:

In [ ]:
```
# training loop
w1= np.random.randn()
w2= np.random.randn()
b= np.random.randn()
learning_rate=0.01
costs=[]


for i in range(50000):
    ri = np.random.randint(len(datos))
    point=datos[ri]
    z= point[0]*w1+point[1]*w2+b
    pred = sigmoid(z)


    # back progpagation
    target = point[3]
    cost= np.square(pred-target)

    #print(target, pred, cost)
    dcost_pred=2*(pred-target)
    dpred_z = sigmoid_p(z)

    dz_w1= point[0]
    dz_w2 =point[1]
    dz_b = 1

    dcost_w1=dcost_pred*dpred_z*dz_w1
    dcost_w2=dcost_pred*dpred_z*dz_w2
    dcost_b=dcost_pred*dpred_z*dz_b
    w1=w1-learning_rate*dcost_w1
    w2=w2-learning_rate*dcost_w2
    b=b-learning_rate*dcost_b

    cost_sum = 0
    for j in range(len(datos)):
        p = datos[j]
        z= p[0]*w1+p[1]*w2+b
        pred = sigmoid(z)
        target = p[3]
        cost_sum += np.square(pred-target)
    costs.append(cost_sum)




plt.plot(costs)
```

jupyter Neural Network for SMP parts Last Checkpoint: 03/19/2018 (autosaved)

File Edit View Insert Cell Kernel Widgets Help

Run Code

In [7]:

```
# propagation algorithm
def cost_evaluation(I,H,HN, O, datos, w,b):
    cost=0
    for j in range(len(datos)):
        y=0
        z=0
        weigth_index = 0
        Pred_index = 0
        Neuron_pred = np.zeros(shape=(H*HN+O,1))
        zeta = np.zeros(shape=(H*HN+O,1))

        #for i1 in range (H):

        point=datos[j]
        for i in range (HN):
                for x in range (I):
                    z+= point[x]*w[weigth_index]
                    weigth_index =  weigth_index+1
                z+=b[0]
                zeta[y] = z
                Neuron_pred[y] = sigmoid(z)
                y=y+1
                z=0

        if H>1:
            for i1 in range (H-1):
                    for i in range (HN):
                        for x in range (HN):
                            z+= Neuron_pred[x+HN*i1]*w[weigth_index]
                            weigth_index =  weigth_index+1
                        z+=b[i1+1]
                        zeta[y] = z
                        Neuron_pred[y] = sigmoid(z)
                        y=y+1
                        z=0


            for i in range (O):
                        for x in range (HN):
                            z+= Neuron_pred[x+HN*(i1+1)]*w[weigth_index]
                            weigth_index =  weigth_index+1
                        z+=b[i1+2]
                        zeta[y] = z
                        Neuron_pred[y] = sigmoid(z)
                        y=y+1
                        z=0
        else:
            for i in range (O):
                        for x in range (HN):
                            z+= Neuron_pred[x]*w[weigth_index]
                            weigth_index =  weigth_index+1
                        z+=b[1]
```

Vita

Mr. Carlos Garcia is a Ph.D. candidate under the Electrical & Computer Engineering Ph.D. program (Systems Engineering track) at the University of Texas at El Paso (UTEP). He received his B.S. degree in Electromechanical Engineering from The Juarez Technology Institute in 2008. He received his M.S. degree in Manufacturing Engineering from UTEP in 2012. He is research assistant at the Department of Industrial, Manufacturing and Systems Engineering. His current research activities focus on the development of advanced polymer composite systems fabricated using additive manufacturing. Moreover, his research activities further expand to process control and optimization of additive manufacturing processes, and quality control of advanced polymer systems by applying statistical and data analytic methods. His research work has resulted into 11 Journal manuscripts that report findings related to advanced polymer composite systems. Additionally, he has combined his education with work experience on various mass production-industry engineering positions to include being the co-instructor of Modern Manufacturing Systems, and Design for Manufacturability (Master Degree level).

Contact Information: cagarciarosales@miners.utep.edu